DISSERTATION

submitted to the
Combined Faculties of the Natural Sciences and Mathematics
of the Ruperto-Carola-University of Heidelberg, Germany
for the degree of

Doctor of Natural Sciences

Put forward by

Dipl.-Phys. Alexander Bien

born in: Heidelberg, Germany

Oral examination: 5th February 2014

Measurement of the polarisation amplitudes in $B^0 \to J/\psi K^*(892)^0$ decays with the LHCb experiment

Referees: Prof. Dr. Ulrich Uwer

Prof. Dr. Hans-Christian Schultz-Coulon

Abstract: In this thesis a measurement of the polarisation amplitudes and the corresponding strong phases of the decay $B^0 \to J/\psi(\mu^+\mu^-)K^*(892)^0(K^+\pi^-)$ is presented. Studying $B^0 \to J/\psi(\mu^+\mu^-)K^*(892)^0(K^+\pi^-)$ and $\overline{B}^0 \to J/\psi(\mu^+\mu^-)\overline{K}^*(892)^0(K^-\pi^+)$ decays separately allows for the measurement of direct CP violation. The Standard Model of particle physics does not predict any CP-violating processes for this decay channel. Thus, this analysis also serves as a search for new phenomena beyond the Standard Model.
The measurement is performed using the full data sample collected with the LHCb detector in 2011 taken in proton-proton collisions at a centre-of-mass energy of 7 TeV corresponding to an integrated luminosity of approximately $1.0\,\text{fb}^{-1}$. The determination of the polarisation amplitudes requires an angular analysis of the final state particles to disentangle the three possible angular momentum states. The observables are obtained using a four-dimensional maximum likelihood fit depending on the three decay angles and the decay time of the B^0 meson. The values of the polarisation amplitudes and corresponding phases are determined to be $R_\parallel = 0.227 \pm 0.004 \pm 0.011$, $R_\perp = 0.201 \pm 0.004 \pm 0.008$, $\delta_\parallel = -2.94 \pm 0.02 \pm 0.03$ and $\delta_\perp = 2.94 \pm 0.02 \pm 0.02$, where the errors are statistical and systematic, respectively. The fit is performed in four bins of the $K^+\pi^-$ invariant mass to measure the fraction of the non-resonant $K^+\pi^-$, so-called S-wave, contribution. Averaged over all mass bins, it is measured to be $F_\text{S} = (6.4 \pm 0.3 \pm 1.0)\%$. By determining the phase difference between the resonant P-wave and the S-wave contributions in the four mass bins a two-fold ambiguity in the strong phases is resolved. Furthermore, no evidence for CP violation is observed.

Kurzfassung: In dieser Arbeit wird eine Messung der Polarisationsamplituden und der zugehörigen starken Phasen des Zerfalls $B^0 \to J/\psi(\mu^+\mu^-)K^*(892)^0(K^+\pi^-)$ vorgestellt. Die getrennte Untersuchung der Zerfälle $B^0 \to J/\psi(\mu^+\mu^-)K^*(892)^0(K^+\pi^-)$ und $\overline{B}^0 \to J/\psi(\mu^+\mu^-)\overline{K}^*(892)^0(K^-\pi^+)$ erlaubt die Messung direkter CP-Verletzung. Das Standardmodell der Teilchenphysik sagt keine CP-verletzenden Prozesse für diesen Zerfallskanal voraus. Daher dient diese Analyse auch der Suche nach neuen Phänomenen jenseits des Standardmodells.
Die Messung benutzt den vollen Datensatz, der im Jahr 2011 am LHCb-Detektor aufgenommen wurde, wobei Proton-Proton-Kollisionen der Schwerpunktsenergie 7 TeV verwendet wurden. Dies entspricht einer integrierten Luminosität von etwa $1.0\,\text{fb}^{-1}$. Die Bestimmung der Polarisationsamplituden erfordert eine Winkelanalyse der Teilchen im Endzustand, um die drei möglichen Drehimpulszustände zu trennen. Die Observablen werden durch einen vierdimensionalen Maximum-Likelihood-Fit bestimmt, der von den drei Zerfallswinkeln und der Zerfallszeit des B^0-Mesons abhängt. Die Werte der Polarisationsamplituden und zughörigen Phasen werden zu $R_\parallel = 0{,}227 \pm 0{,}004 \pm 0{,}011$, $R_\perp = 0{,}201 \pm 0{,}004 \pm 0{,}008$, $\delta_\parallel = -2{,}94 \pm 0{,}02 \pm 0{,}03$ und $\delta_\perp = 2{,}94 \pm 0{,}02 \pm 0{,}02$ ermittelt, wobei die Fehler jeweils statistisch und systematisch sind. Der Fit wird in vier Bereichen der invarianten $K^+\pi^-$-Masse durchgeführt, um den Anteil des nicht-resonanten oder sogenannten S-Wellen-Anteils zu messen. Gemittelt über alle vier Massenbereiche wird dieser zu $F_\text{S} = (6{,}4 \pm 0{,}3 \pm 1{,}0)\%$ bestimmt. Durch die Messung der Phasendifferenz zwischen dem resonanten P-Wellen- und dem S-Wellen-Anteil in den vier Massenbereichen wird eine zweifache Ambiguität der starken Phasen aufgelöst. Zudem wird kein Hinweis auf CP-Verletzung beobachtet.

The Tiger

Tiger, tiger, burning bright
In the forests of the night,
What immortal hand or eye
Could frame thy fearful symmetry?

In what distant deeps or skies
Burnt the fire of thine eyes?
On what wings dare he aspire?
What the hand dare seize the fire?

And what shoulder and what art
Could twist the sinews of thy heart?
And when thy heart began to beat,
What dread hand? and what dread feet?

What the hammer? what the chain?
In what furnace was thy brain?
What the anvil? what dread grasp
Dare its deadly terrors clasp?

When the stars threw down their spears,
And water'd heaven with their tears,
Did He smile His work to see?
Did He who made the lamb make thee?

Tiger, tiger, burning bright
In the forests of the night,
What immortal hand or eye
Dare frame thy fearful symmetry?

William Blake (1757–1827)

Contents

Introduction

Since the start of the Large Hadron Collider particle physics has experienced a large increase in media attention. In general, the project received a very positive feedback and people were looking forward to the first results. Only some concerns were raised about black holes being created when operating the collider but they never dominated public discussion. The media reception culminated in the likely discovery of the Higgs boson, the last missing piece of the Standard Model of particle physics, and the award of the Nobel Prize to the theoretical physicists Peter Higgs and François Englert. Enthusiastically, the discovery of the "God Particle" [1] was celebrated. Also other less popular results, like the analysis of rare decays sensitive to the observation of new physical phenomena and the discovery of new hadrons, have been mentioned in the media.

At the Large Hadron Collider there are four major experiments with different purposes. The LHCb experiment, for example, has the goal to shed light on the mystery of matter-antimatter asymmetry. We owe our existence the fact that in the early universe slightly more matter than antimatter had been produced. If there had been an equilibrium between both components, no structures like galaxies would have been formed. One essential prerequisite for this asymmetry is CP violation [2]. When a CP or Charge Parity operation is performed, a particle is converted into its antiparticle and the spatial coordinates of the particle are inverted. Naïvely, one would expect that all physical processes are invariant under such a transformation. However, in 1964 Cronin, Fitch and co-workers found evidence for CP violation in decays of kaons [3]. The combined CPT operation (T denotes time reversal) is a fundamental property of Quantum Field Theory [4] and no evidence for its violation has been observed (see, for example, [5]). The CP-violating phenomena measured so far at various experiments, however, cannot account for the amount of CP violation needed to explain the matter-antimatter asymmetry in the universe. This triggers the search for new processes.

The LHCb experiment uses numerous meson decays to measure CP asymmetries. One of the most important processes is the decay $B_s^0 \to J/\psi(\mu^+\mu^-)\phi(K^+K^+)$ where a CP-violating phase, ϕ_s, can be measured. Originally, the decay channel $B^0 \to J/\psi(\mu^+\mu^-)K^*(892)^0(K^+\pi^-)$ has been intended as a cross-check analysis be-

cause it shares many common problems like the description of detector acceptance effects and the role of non-resonant contributions to the decay amplitude. However, it has become evident that this analysis has its own decay specific problems: the acceptance effects are much more pronounced, the non-resonant fraction (i.e. direct decays into a pion and a kaon without the creation of a $K^*(892)^0$ resonance) is higher and the discrepancies between data and simulation are larger compared to $B_s^0 \to J/\psi\phi$ decays. Simulated event samples are necessary to describe the detector acceptance. Therefore, the study of $B^0 \to J/\psi K^*(892)^0$ decays has developed into a full separate analysis that will be detailed in this thesis. The main goal is the study of the three different polarisation states of the J/ψ and the $K^*(892)^0$ mesons. Each of these states can be described by a complex amplitude. The charge of the kaon directly indicates the flavour of the B^0 meson at the time of the decay. In other words, one can determine whether it was a B^0 or a $\overline{B}^0$ meson that decayed. Separating the data set in two sub-samples allows then to search for CP violation by measuring the polarisation amplitudes for both B^0 and $\overline{B}^0$ decays. As the Standard Model does predict neither direct nor indirect CP violation for this decay, any significant deviation between the two sub-samples would indicate new physical phenomena [6, 7, 8]. Two main complications have to be considered when performing the analysis: Firstly, as the acceptance effects are determined from simulated samples, any differences between data and simulation in kinematic quantities have to be considered. The discrepancy is especially large in the pion momentum. And secondly, this analysis only considers non-resonant contributions and the $K^*(892)^0$ resonance which has a total spin of $J = 1$. However, all possible $K^+\pi^-$ resonances have to be accounted for to correctly determine the polarisation amplitudes. For both problems solutions will be developed.
The analysis presented here uses the data set that has been recorded in proton-proton collisions at a centre-of-mass energy of $\sqrt{s} = 7$ TeV with the LHCb detector in the year 2011. This corresponds to an integrated luminosity of $\mathcal{L}_{\text{int}} \approx 1$ fb^{-1}.
The structure of the thesis is as follows: After a theoretical introduction in Chapter 1 and a description of the LHCb detector and its trigger system in Chapter 2, the selection criteria for $B^0 \to J/\psi K^*(892)^0$ decays are detailed in Chapter 3 together with the determination of the detector acceptances. In Chapter 4 the technique to extract the physical observables from the data set is explained. A four-dimensional maximum likelihood fit is used and the validation of the fit is also summarised in the same chapter. An important part of the analysis is the study of background sources to the signal decay $B^0 \to J/\psi K^*(892)^0$. These are investigated in Chapter 5. An extensive comparison between data and simulation is carried out in Chapter 6 and a strategy is presented how the differences can be reduced. Chapter 7 is dedicated to the investigation of one of the main systematic uncertainties, the treatment of further resonances in the $K^+\pi^-$ mass spectrum. In Chapter 8 the six other systematic uncertainties in the determination of the physical observables are discussed and the dominant sources identified. The main results of the analysis, the polarisation amplitudes and the search for CP violation are presented in Chapter 9. The thesis

ends with a short conclusion and prospects for the future.
This thesis is based on the work of the LHCb collaboration. Many tools that are used have been developed by colleagues within and outside the LHCb group at Heidelberg University. In this case references are given. The analysis presented here was performed especially together with the LHCb group at Edinburgh University. To document the work for the LHCb collaboration a so-called analysis note was prepared and a paper for the PRD journal was written for which the author of this thesis was also the contact author:

- A. Bien *et al.*, "Angular analysis of $B^0 \to J/\psi K^*(892)^0$ with ~ 1 fb^{-1}", LHCb analysis note (LHCb-ANA-2012-036), 2012
- R. Aaij *et al.* (LHCb collaboration), "Measurement of the polarisation amplitudes in $B^0 \to J/\psi K^*(892)^0$ decays", Physical Review D, volume 88, 052002, 2013

These documents are referenced to when studies are presented that have not been performed by the author. The following chapters are predominantly based on the own work of the author: Chapter 3, Sections 3.4, 3.5; Chapter 4, Sections 4.3 (part of the implementation), 4.4, 4.5; Chapters 5, 6 (idea for Sec. 6.2 from Edinburgh), 7 (pseudo-experiments provided by T. Skwarnicki), 8, 9.

The following figures show distributions using LHCb data: 3.1, 3.2, 3.3 (simulation only), 3.4; 4.1, 4.2; 5.1, 5.2 (simulation only), 5.3 (simulation only), 5.4 (simulation only), 5.5 (simulation only), 5.6 (simulation only); 6.1, 6.2, 6.3 (simulation only), 6.4, 6.5, 6.6, 6.7; 7.1, 7.2, 7.3, 7.4; 8.1; 9.1, 9.2, 9.3, 9.4, 9.5

Chapter 1

Theoretical Overview

> The truth is incontrovertible. Malice may attack it, ignorance may deride it, but in the end, there it is.
> *Sir Winston Churchill (1874-1965)*

This chapter details the theoretical background of the analysis presented here. First, the Standard Model of particle physics is shortly introduced, followed by a summary of the different sources for CP violation. In addition, a phenomenological description of the decay $B^0 \to J/\psi K^*(892)^0$ in the Standard Model is given and and the measurement of possible new phenomena is discussed.

1.1 The Standard Model of particle physics

The Standard Model of particle physics (SM) describes the current knowledge of the most elementary constituents of matter and their interactions [9]. The SM has been tested very successfully at various particle accelerators, most recently with the discovery of a Higgs boson [1] at the Large Hadron Collider (LHC) at the Conseil Européen pour la Recherche Nucléaire (CERN). The fundamental matter particles, quarks and leptons, are all fermions of spin $1/2$ and appear in three different generations [10, 11, 12]. The main properties of these particles are summarised in Table 1.1 (in the following, natural units are used, i.e. $c = 1$). Open questions in the SM are, among others, why these particles appear in three generations and masses are so different, not only across but also within the generations.
Quarks and charged leptons are massive, contrary to the neutrinos which are assumed to be massless in the SM. Experiments on neutrino oscillations have prompted the conclusion that neutrinos have very small but non-zero masses, see e.g. [13]. To each quark and lepton there exists an antiparticle with the same mass but opposite quantum numbers (e.g. electric charge). Quarks can form composite particles, mesons (quark and anti-quark) and baryons (three quarks).
The interactions between the fundamental matter constituents, the electromagnetic, the weak and the strong force, are mediated by vector bosons of integer spin, a

	Quarks			Leptons		
Gen.	Type	El. charge [e]	Mass	Type	El. charge [e]	Mass
I	u	$+\frac{2}{3}$	$2.3^{+0.7}_{-0.5}$ MeV	ν_e	0	≤ 2 eV
	d	$-\frac{1}{3}$	$4.8^{+0.7}_{-0.3}$ MeV	e	-1	511.0 keV
II	c	$+\frac{2}{3}$	1.28 ± 0.03 GeV	ν_μ	0	≤ 2 eV
	s	$-\frac{1}{3}$	95 ± 5 MeV	μ	-1	105.7 MeV
III	t	$+\frac{2}{3}$	173.5 ± 1.0 GeV	ν_τ	0	≤ 2 eV
	b	$-\frac{1}{3}$	4.18 ± 0.03 GeV	τ	-1	1.78 GeV

Table 1.1: *Properties of the fundamental quarks and leptons in the SM [5].*

summary of which can be found in Table 1.2. The mediators of the electromagnetic and the strong force, photons and gluons, are massless whereas the bosons carrying the weak force, the $W^\pm$ and Z^0 bosons, are massive. The electromagnetic and the weak force can be unified to the electroweak interaction.
The SM Lagrangian is invariant under the gauge transformation of the combined $SU(3)_C \otimes SU(2)_L \otimes U(1)_Y$ group. The interactions are the result of the invariance requirement. To each interaction a conserved quantum number can be associated which is denoted by the subscripts in the above formula (for the following, see [15]). Quantum Chromodynamics (QCD), describing the strong interaction, i.e. interactions between quarks, is associated to the $SU(3)_C$ group. The corresponding quantum number is called colour, C, which can appear in three different realisations (red, green, blue and the corresponding anti-colours). As the mediators of the strong interaction, the gluons, carry colour themselves, they are self-interacting (contrary to, for example, photons). Therefore, in addition to quark-gluon interactions there can be three and four gluon interactions. The most important characteristics of QCD are asymptotic freedom and confinement: Interactions between quarks become weaker with decreasing distance, whereas free quarks do not exist. Instead, they are always in a bound state.
The unified electroweak interaction can be described by a $SU(2)_L \otimes U(1)_Y$ symmetry group. Associated to the weak $SU(2)_L$ group there are three gauge bosons B_i, with the weak isospin T (third component T_3) being the conserved quantum number.

Interaction	Couples to	Boson	Mass [GeV]
strong	colour	8 gluons (g)	0
electromagn.	electric charge	photon (γ)	0
weak	weak charge	$W^\pm$, Z	80.39 ± 0.02, 91.188 ± 0.002

Table 1.2: *Bosons mediating the three interactions in the SM of particle physics [5, 14].*

The theory is a so-called chiral theory, i.e. only left-handed fermions (hence, the index L) and right-handed anti-fermions couple to the gauge bosons. The conserved quantum number of the $U(1)_Y$ group is the hypercharge, Y. The mediator is the gauge boson A. The hypercharge of a fermion can be determined by $Y = Q - T_3$, where Q is the electric charge. The mediators of the weak force, the $W^{\pm}$ and Z bosons, and the photon are linear combinations of the B_i and A bosons (the $W^{\pm}$ bosons are combinations of B_1 and B_2 only). The photon couples to the electric charge of the fermions which is carried by all fermions except for the neutrinos but is not self-coupling. The bosons of the weak interaction couple to the weak charge which they carry themselves. Charged currents can only be mediated by the $W^{\pm}$ bosons. They are the only possibility in the SM for interactions between the three generations. Flavour Changing Neutral Currents (FCNC) are forbidden in the SM on tree-level and can only occur in so-called loop (penguin or box) processes.
A priory, particles in the SM are massless. However, the bosons of the weak interaction, the $W^{\pm}$ and the Z bosons, are massive. The so-called Higgs mechanism describes how the particles acquire mass. The basic idea of this mechanism is to introduce a potential, consisting of a doublet of two complex scalar fields. This potential gives rise to a non-symmetric ground state and thus a spontaneous symmetry-breaking. The mechanism predicts a massive spin 0 particle, the so-called Higgs particle H, which has recently been discovered at the LHC. The fermion couplings to the Higgs field give rise to the fermion masses. For a more detailed review on the Higgs mechanism, see for example [16].

1.2 The CKM mechanism

The electroweak quark eigenstates (d', s', b') are not equivalent to the mass eigenstates (d, s, b) [5, 17]. This gives rise to transformations between quarks which can be described by a unitary matrix, the so-called Cabibbo-Kobayashi-Maskawa (CKM) matrix V_{CKM} [17] (by convention only the down-type quarks are rotated):

$$\begin{pmatrix} d' \\ s' \\ b' \end{pmatrix} = \begin{pmatrix} V_{ud} & V_{us} & V_{ub} \\ V_{cd} & V_{cs} & V_{cb} \\ V_{td} & V_{ts} & V_{tb} \end{pmatrix} \begin{pmatrix} d \\ s \\ b \end{pmatrix}. \tag{1.1}$$

As the matrix elements can be complex, there are 18 free parameters which can be reduced to nine due to the unitarity relation $V_{\mathrm{CKM}}(V_{\mathrm{CKM}})^{\dagger} = \mathbb{1}$. Five of the remaining paramters can be absorbed into non-observable quark phases, so the matrix can be parametrised by three Euler angles $\theta_{12}, \theta_{23}, \theta_{31}$ and one phase δ

$$V_{\mathrm{CKM}} = \begin{pmatrix} c_{12}c_{13} & s_{12}c_{13} & s_{13}e^{-i\delta} \\ -s_{12}c_{23} - c_{12}s_{23}s_{13}e^{i\delta} & c_{12}c_{23} - s_{12}s_{23}s_{13}e^{i\delta} & s_{23}c_{13} \\ s_{12}c_{23} - c_{12}s_{23}s_{13}e^{i\delta} & -c_{12}s_{23} - s_{12}c_{23}s_{13}e^{i\delta} & c_{23}c_{13} \end{pmatrix}, \tag{1.2}$$

where $s_{ij} = \sin\theta_{ij}$ and $c_{ij} = \cos\theta_{ij}$. The phase δ is responsible for all CP violating effects in flavour-changing processes within the SM (for a detailed explanation of CP violation, see the next section). Experiments show that $s_{13} \ll s_{23} \ll s_{12}$. This hierarchy is visualised in the so-called Wolfenstein parametrisation of the CKM matrix [5]. Using $s_{12} = \lambda, s_{23} = A\lambda^2$ and $s_{13}e^{-i\delta} = A\lambda^3(\rho + i\eta)$ with $\lambda \approx 0.23$, one can write to the $\mathcal{O}(\lambda^4)$

$$V_{\mathrm{CKM}} = \begin{pmatrix} 1 - \frac{\lambda^2}{2} & \lambda & A\lambda^3(\rho - i\eta) \\ -\lambda & 1 - \frac{\lambda^2}{2} & A\lambda^2 \\ A\lambda^3(1 - \rho - i\eta) & -A\lambda^2 & 1 \end{pmatrix}. \tag{1.3}$$

The elements of the CKM matrix are fundamental parameters of the SM and their exact determination is crucial. For a more detailed summary see [5].

1.3 CP violation

In the following an overview of CP violation (CPV) of a pseudoscalar meson P is given (see [5]). The meson can be a charged or neutral K, D, B, or B_s meson. The decay amplitudes of P and its CP conjugate $\overline{P}$ to a final state f (CP conjugate $\overline{f}$) are defined as

$$A_f = \langle f|\mathcal{H}|P\rangle, \overline{A}_f = \langle f|\mathcal{H}|\overline{P}\rangle, A_{\overline{f}} = \langle \overline{f}|\mathcal{H}|P\rangle, \overline{A}_{\overline{f}} = \langle \overline{f}|\mathcal{H}|\overline{P}\rangle, \tag{1.4}$$

where $\mathcal{H}$ denotes the Hamilton operator of the weak interaction.
Neutral mesons that are initially a superposition of P^0 and $\overline{P}^0$ will evolve in time (mixing). This time-dependent two-state system can be described by an effective 2×2 Hamiltonian $\mathbf{H}$ which can be expressed in terms of two Hermitian matrices $\mathbf{M}$ and $\mathbf{\Gamma}$

$$\mathbf{H} = \mathbf{M} - \frac{i}{2}\mathbf{\Gamma}, \tag{1.5}$$

where $\mathbf{M}$ and $\mathbf{\Gamma}$ are the mass and decay width matrix, respectively. Using the Hermiticity of $\mathbf{M}$ and $\mathbf{\Gamma}$ ($\mathrm{M}_{21} = \mathrm{M}_{12}^*$, $\Gamma_{21} = \Gamma_{12}^*$) and the CPT invariance ($\mathrm{M}_{11} = \mathrm{M}_{22} = \mathrm{M}$, $\Gamma_{11} = \Gamma_{22} = \Gamma$), one can re-write the matrix as

$$\mathbf{H} = \begin{pmatrix} \mathrm{M} - \frac{i}{2}\Gamma & \mathrm{M}_{12} - \frac{i}{2}\Gamma_{12} \\ \mathrm{M}_{12}^* - \frac{i}{2}\Gamma_{12}^* & \mathrm{M} - \frac{i}{2}\Gamma \end{pmatrix}. \tag{1.6}$$

The corresponding eigenvectors are composed of well-defined masses and decay widths. One can express the strong interaction eigenstates P^0 and $\overline{P}^0$ in the light and heavy mass eigenstates $\langle P_L\rangle$ and $\langle P_H\rangle$ by introducing two complex parameters p and q (with $|p|^2 + |q|^2 = 1$)

$$\begin{aligned} |P_L\rangle &\propto p|P^0\rangle + q|\overline{P}^0\rangle \\ |P_H\rangle &\propto p|P^0\rangle + q|\overline{P}^0\rangle. \end{aligned} \tag{1.7}$$

The mass and decay width of the flavour eigenstates can be obtained from the mass eigenvalues $(M_L - i\Gamma_L/2)$ and $(M_H - i\Gamma_H/2)$ by

$$\begin{aligned} \Gamma &= 1/2(\Gamma_L + \Gamma_H) \\ M &= 1/2(M_L + M_H). \end{aligned} \tag{1.8}$$

The corresponding mass and decay widths are defined as

$$\begin{aligned} \Delta\Gamma &= \Gamma_L - \Gamma_H \\ \Delta M &= M_H - M_L. \end{aligned} \tag{1.9}$$

For B^0 mesons, $\Delta\Gamma_{(d)} \approx 0$ holds. Thus, the decay width is neglected in this analysis. There are three categories of CPV which are explained in the following:

1. CPV in decay or direct CPV is defined as

$$|\overline{A}_{\overline{f}}/A_f| \neq 1. \tag{1.10}$$

   For charged meson decays where mixing is not possible (e.g. $B^{\pm} \to D^0 K^{\pm}$) CPV in decay is the only source for CP asymmetry, which can be written as

$$A_{f^{\pm}} = \frac{\Gamma(P^- \to f^-) - \Gamma(P^+ \to f^+)}{\Gamma(P^- \to f^-) + \Gamma(P^+ \to f^+)} = \frac{|\overline{A}_{f^-}/A_{f^+}|^2 - 1}{|\overline{A}_{f^-}/A_{f^+}|^2 + 1}. \tag{1.11}$$

2. CPV in mixing is defined as

$$|q/p| \neq 1. \tag{1.12}$$

   This source can be, for example, measured in semileptonic decays of neutral mesons by evaluating

$$A_{\mathrm{SL}} = \frac{\Gamma(\overline{P}^0 \to l^+ X) - \Gamma[P^0 \to l^- X)}{\Gamma(\overline{P}^0 \to l^+ X) + \Gamma(P^0 \to l^- X)} = \frac{1 - |q/p|^4}{1 + |q/p|^4}. \tag{1.13}$$

3. For neutral mesons where both P^0 and $\overline{P}^0$ decay to the same final state f (e.g. $B_s^0 \to J/\psi\phi$), the neutral meson can either decay to the final state directly or first mix and then decay which gives rise to CPV in the interference between mixing and decay. The CP-violating parameter λ_f is then defined as

$$\Im(\lambda_f) = \Im\left(\frac{q}{p}\frac{\overline{A}_f}{A_f}\right) \neq 0. \tag{1.14}$$

   This category of CPV is time-dependent and can be measured using decays of neutral mesons into CP eigenstates f_{CP}:

$$A_{f_{\mathrm{CP}}}(t) = \frac{\mathrm{d}\Gamma/\mathrm{d}t[\overline{P}^0(t) \to f_{\mathrm{CP}}] - \mathrm{d}\Gamma/\mathrm{d}t[P^0(t) \to f_{\mathrm{CP}}]}{\mathrm{d}\Gamma/\mathrm{d}t[\overline{P}^0(t) \to f_{\mathrm{CP}}] + \mathrm{d}\Gamma/\mathrm{d}t[P^0(t) \to f_{\mathrm{CP}}]}. \tag{1.15}$$

If the decay width difference $\Delta\Gamma$ is close to zero and CPV in mixing is negligible, as predicted for B mesons, then the above equation simplifies as follows

$$A_{f_{\rm CP}}(t) = S_f \sin(\Delta M t) - C_F \cos(\Delta M t), \tag{1.16}$$

where

$$S_f = \frac{2\Im(\lambda_f)}{1+|\lambda_f|^2}, \quad C_f = \frac{1-|\lambda_f|^2}{1+|\lambda_f|^2}. \tag{1.17}$$

If, furthermore, $|\overline{A}_{f_{\rm CP}}| = |A_{f_{\rm CP}}|$ holds, then the interference between mixing and decay is the only source of CPV and one gets for the time-dependent mixing asymmetry.

$$A_{f_{\rm CP}}(t) = \Im(\lambda_{f_{\rm CP}}) \sin(\Delta M t). \tag{1.18}$$

Possible CPV effects in $B^0 \to J/\psi K^*(892)^0$ decays and how they can be measured are discussed in Sec. 1.5.

1.4 Phenomenology of $B^0 \to J/\psi K^*(892)^0$ decays in the Standard Model

1.4.1 Motivation

The study of the decay $B^0 \to J/\psi(\mu^+\mu^-)K^*(892)^0(K^+\pi^-)$ (in the following K^{*0} is used for $K^*(892)^0$ unless stated otherwise) and its charge conjugate $\overline{B}^0 \to J/\psi(\mu^+\mu^-)\overline{K}^*(892)^0(K^-\pi^+)$ is intended to measure the polarisation amplitudes defined in the next subsection. Also, the angular anlysis of $B^0 \to J/\psi K^{*0}$ and their flavour conjugate decays can probe possible physics beyond the Standard Model (BSM). The SM predicts that the observables are equal for both, B^0 and $\overline{B}^0$ decays, that can be distinguished by the kaon charge. Any deviation from this prediction would indicate direct CPV. Any limits on CPV would constrain extensions to the SM [6, 7, 8].
The initial motivation to study this decay was to provide a cross-check analysis for the decay $B_s^0 \to J/\psi\phi$ as both analyses share the same kinematic description and use similar techniques like the determination of detector acceptances. Over the time the analysis of $B^0 \to J/\psi K^{*0}$ decays has become independent from the study of other channels also because it has to deal with decay-specific problems.

1.4.2 Description of the decay channel $B^0 \to J/\psi K^{*0}$

In the SM the decay is dominated by the tree diagram (see Figure 1.1(a)), whereas contributions from gluonic and CP-violating weak penguin diagrams (as shown in Figure 1.1(b)) are considerably smaller and therefore neglected [18].

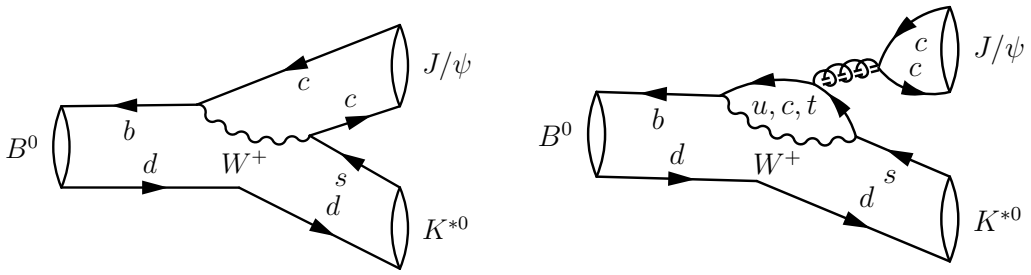

(a) Tree diagram (b) Penguin diagram

Figure 1.1: *Feynman diagrams contributing to $B^0 \to J/\psi K^{*0}$ decays. Figures from [19].*

The B^0, a pseudoscalar meson, decays to two vector particles, the J/ψ and the K^{*0} meson. All decay modes decaying to two particles with non-zero spin require an angular analysis to extract most of the observables (for the following, see [20]). There are three polarisation states, depending on the relative angular momentum between the J/ψ and the K^{*0} meson, $L = 0, 1, 2$. Considering the formula to determine the parity, $P = (-1)^L$, and that the B^0 meson has parity -1, two of the polarisation states are parity violating (the P-even states $L = 0, 2$) and one is parity conserving (the P-odd state $L = 1$). Consequently, the final state is an admixture of P-even and P-odd states. Using an appropriate basis to describe the decay, the time dependence factorises which simplifies the description.
At time $t = 0$ there are three different approaches to describe the polarisation in the final state which are fully equivalent. Firstly, in the helicity basis there are three amplitudes that correspond to the helicity of the two vector mesons. Secondly, the partial wave analysis decomposes the relative angular momentum states $L = 0, 1, 2$. And finally, in the transversity basis the three amplitudes correspond to the spin projections of one vector meson parallel or perpendicular to the other. The latter approach is used in this thesis as it allows for the decomposition of the P-even and P-odd components. The amplitudes are complex, so there are absolute values and phases. The former consist of

$$\begin{aligned} A_0 &\quad \text{longitudinal orientation, corresponding to } L = 0, 2 \\ A_\parallel &\quad \text{transverse-parallel orientation, corresponding to } L = 0, 2 \\ A_\perp &\quad \text{transverse-perpendicular orientation, corresponding to } L = 1, \end{aligned} \tag{1.19}$$

where the orientation is meant to be with respect to the spins of the J/ψ and the K^{*0} meson. The spin orientations are shown in Fig. 1.2. The corresponding CP-

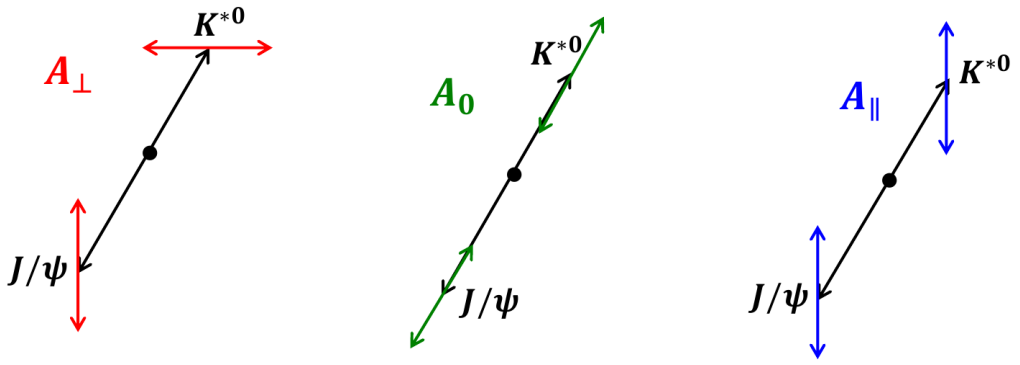

Figure 1.2: *Visualisation of the three transversity amplitudes corresponding to transverse-perpendicular, longitudinal and transverse-parallel orientation.*

conserving strong phases are (where δ_0 is set to zero by convention)

$$\begin{aligned} \delta_\parallel &= \arg(A_\parallel A_0^*), \\ \delta_\perp &= \arg(A_\perp A_0^*). \end{aligned} \tag{1.20}$$

Usually, the absolute values squared of the polarisation amplitudes are measured. As the $K^+\pi^-$ system is in a P-wave state (spin of 1), these amplitudes are denoted as P-wave amplitudes.

To derive the time-dependent decay amplitude for the decay of a pseudoscalar meson to two vector mesons, V_1 and V_2, one considers the three-dimensional polarisation vectors of the two vector mesons, ϵ_{V_1} and ϵ_{V_2}, in the rest-frame of V_1. The three individual amplitudes are linear in both polarisation vectors and include possible powers of $\widehat{p}_{V_2}$, the unit vector along the direction of motion of the second vector meson in the rest-frame of the first. The total decay amplitude is a scalar quantity. Therefore, the P-even decay amplitudes are expressed in terms of the scalar products $\epsilon^*_{V_1} \cdot \epsilon^*_{V_2}$ (this term contributes to A_0 and $A_\parallel$) and $(\epsilon^*_{V_1} \cdot \widehat{p}_{V_2})\,(\epsilon^*_{V_2} \cdot \widehat{p}_{V_2})$ (this term contributs to A_0 only), where * denotes the complex conjugation. To the contrary, the P-odd component has to be represented by a (P-odd) pseudoscalar quantity, $(\epsilon^*_{V_1} \times \epsilon^*_{V_2}) \cdot \widehat{p}_{V_2}$ (axial vector times vector). This term contributes to $A_\perp$ only. One can then replace $(\epsilon^*_{V_1} \cdot \widehat{p}_{V_2})\,(\epsilon^*_{V_2} \cdot \widehat{p}_{V_2})$ by $\epsilon^{*0}_{V_1} \cdot \epsilon^{*0}_{V_2}$ (where 0 denotes the longitudinal component) and subtract off the longitudinal component of the polarisation vectors to replace $\epsilon^*_{V_1} \cdot \epsilon^*_{V_2}$ by $\epsilon^{*\parallel}_{V_1} \cdot \epsilon^{*\parallel}_{V_2}$, where $\parallel$ refers to the transverse-parallel projection. For $B^0 \to J/\psi K^{*0}$ decays one then obtains

$$\Gamma(B^0 \to J/\psi K^{*0}) = \widetilde{A}_0(t)\frac{\epsilon^{*0}_{J/\psi} \cdot \epsilon^{*0}_{K^{*0}}}{x} - \widetilde{A}_\parallel(t)\frac{\epsilon^{*\parallel}_{J/\psi} \cdot \epsilon^{*\parallel}_{K^{*0}}}{\sqrt{2}} - i\widetilde{A}_\perp(t)\frac{(\epsilon^*_{J/\psi} \times \epsilon^*_{K^{*0}}) \cdot \widehat{p}_{K^{*0}}}{\sqrt{2}}, \tag{1.21}$$

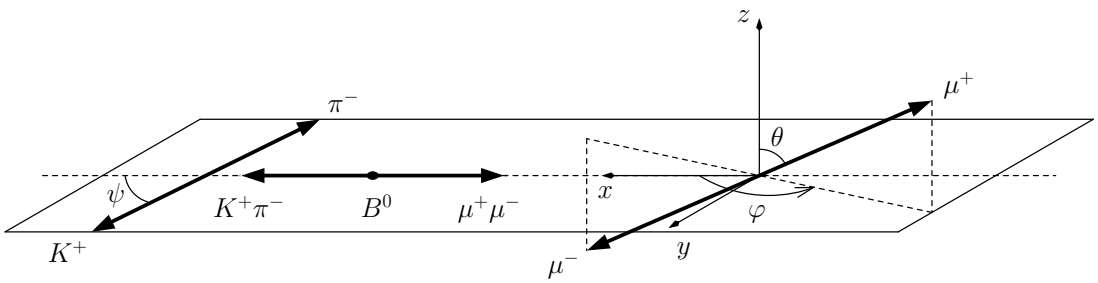

Figure 1.3: *Definitions of the transversity angles θ, ψ, φ, as described in the text. Figure from [19].*

where $\tilde{}$ denotes the full complex amplitude and x is a kinematic factor depending on the momenta and masses of the two vector mesons. A more detailed explanation can be found in [21], [22] and [23].
At time $t = 0$, the decay amplitude depends on the observables A_i and δ_i defined above. In the absence of final-state interactions, theoretical models predict that all three strong phases assume the same value 0 (mod π). However, for colour-suppressed modes like $B^0 \to J/\psi K^{*0}$ this assumption is not necessarily valid. Predictions for the magnitudes of the amplitudes differ between the various theoretical models [21].
As the amplitudes correspond to P-even and P-odd final-state configurations, their time evolution and angular distributions differ [20]. The time evolution can be treated separately and the different polarisation states can be disentangled by an angular analysis. In the transversity formalism the angular variables are denoted as $\Omega = \{\cos\theta, \cos\psi, \varphi\}$ and are defined in Fig. 1.3. For the decay of a B^0, the angle between the flight direction of the μ^+ and the z axis in the J/ψ rest frame is denoted by θ, the corresponding azimuthal angle by φ. The angle between the flight direction of the K^+ meson and the negative flight direction of the J/ψ in the rest frame of the K^{*0} is denoted by ψ. For the decay of a $\overline{B}^0$, the angles are defined with respect to the μ^- and the K^-.
As the K^{*0} is identified by its decay to $K^+\pi^-$, there is always also a component where the B^0 meson decays directly to a non-resonant $K^+\pi^-$ system. This forms an S-wave state (spin of 0), contrary to the resonant P-wave contribution. This irreducible contribution can be described by an additional amplitude A_{S}. The parity of this state is P-odd and the corresponding strong phase is denoted by δ_{S}. In addition, interference between P- and S-wave amplitudes has to be taken into account.
Summing over the $B^0 \to J/\psi K^{*0}$ and $\overline{B}^0 \to J/\psi \overline{K}^{*0}$ contributions, using Eq. 1.21 and assuming $\Delta\Gamma_d = 0$, the differential decay rate can be written as [19, 21, 24]

$$\frac{d^4\Gamma(B^0 \to J/\psi K^{*0})}{dt\, d\Omega} \propto e^{-\Gamma_d t} \sum_{k=1}^{10} h_k f_k(\Omega) \,, \tag{1.22}$$

k	h_k	$f_k(\Omega)$
1	$\lvert A_0\rvert^2$	$\frac{9}{32\pi} 2\cos^2\psi(1-\sin^2\theta\cos^2\varphi)$
2	$\lvert A_\parallel\rvert^2$	$\frac{9}{32\pi}\sin^2\psi(1-\sin^2\theta\sin^2\varphi)$
3	$\lvert A_\perp\rvert^2$	$\frac{9}{32\pi}\sin^2\psi\sin^2\theta$
4	$\lvert A_\parallel\rvert\lvert A_\perp\rvert\sin(\delta_\perp-\delta_\parallel)$	$-\frac{9}{32\pi}\sin^2\psi\sin2\theta\sin\varphi$
5	$\lvert A_0\rvert\lvert A_\parallel\rvert\cos(\delta_\parallel)$	$\frac{9}{32\pi\sqrt{2}}\sin2\psi\sin^2\theta\sin2\varphi$
6	$\lvert A_0\rvert\lvert A_\perp\rvert\sin(\delta_\perp)$	$\frac{9}{32\pi\sqrt{2}}\sin2\psi\sin2\theta\cos\varphi$
7	$\lvert A_{\rm S}\rvert^2$	$\frac{3}{32\pi}2(1-\sin^2\theta\cos^2\varphi)$
8	$\lvert A_\parallel\rvert\lvert A_{\rm S}\rvert\cos(\delta_\parallel-\delta_{\rm S})$	$\frac{3}{32\pi}\sqrt{6}\sin\psi\sin^2\theta\sin2\varphi$
9	$\lvert A_\perp\rvert\lvert A_{\rm S}\rvert\sin(\delta_\perp-\delta_{\rm S})$	$\frac{3}{32\pi}\sqrt{6}\sin\psi\sin2\theta\cos\varphi$
10	$\lvert A_0\rvert\lvert A_{\rm S}\rvert\cos(\delta_{\rm S})$	$\frac{3}{32\pi}4\sqrt{3}\cos\psi(1-\sin^2\theta\cos^2\varphi)$

Table 1.3: *Definition of the factors h_k and the functions f_k appearing in Eq. 1.22 [19, 21, 24].*

where t is the B^0 decay time and Γ_d the corresponding total decay width. The h_k factors are combinations of the polarisation amplitudes. The f_k are functions of the decay angles, normalised such that their integrals over Ω are unity. The definitions of these factors and functions can be found in Table 1.3. The first six terms describe the P-wave contribution, the seventh term is the pure S-wave part and the last three terms describe the interference between P- and S-wave amplitudes.
The differential decay rate for $\overline{B}^0 \to J/\psi\overline{K}^{*0}$ decays can be determined from Eq. 1.22 by using the charge conjugate final state particles to calculate the angles and then multiplying the angular functions f_4, f_6 and f_9 in Table 1.3 by -1. This allows to separately analyse B^0 and $\overline{B}^0$ decays.

1.4.3 Resolving the ambiguity in the strong phases

It can be seen from Table 1.3 that the combinations of the polarisation amplitudes h_k are invariant under the phase transformation

$$(\delta_\parallel, \delta_\perp, \delta_{\rm S}) \longleftrightarrow (-\delta_\parallel, \pi-\delta_\perp, -\delta_{\rm S}). \tag{1.23}$$

The corresponding 2-fold ambiguity has already been resolved in the analysis of $B_s^0 \to J/\psi\phi$ decays at the LHCb experiment [25] which has been done in the following way: Already in 1955 Eugene Wigner pointed out in his causality principle [26] that the phase of a resonant amplitude (as in $B_s^0 \to J/\psi\phi$ and $B^0 \to J/\psi K^{*0}$) rises with increasing invariant mass. The phase changes in total by a value of $\pi/2$. Indeed, the P-wave phases increase rapidly around the K^{*0} mass whereas the non-resonant S-wave phase increases, if at all, very slowly [25]. Therefore, one expects that the phase difference between P- and S-wave, e.g. $\delta_{\rm S}-\delta_0$, decreases rapidly.

This behaviour allows to resolve the ambiguity by determining the phase difference in bins of the $K^+\pi^-$ mass around the K^{*0} resonance. One expects two solutions, one rapidly decreasing, the other steeply rising, with the first being the physical solution.

1.4.4 Coupling between P- and S-wave

In principle, the decay rate quoted in Eq. 1.22 depends on the $K^+\pi^-$ mass. All P-wave amplitudes can be assumed to have the same $m(K^+\pi^-) \equiv m$ dependence following the shape of a Breit-Wigner function of the K^{*0} resonance [27]. If the P-wave amplitudes are normalised to the total P-wave rate, then they are independent of m. The S-wave, however, has a different mass behaviour and therefore varies with m. For the exact parametrisation of the amplitudes, see Sec. 4.2.
The most accurate way would be to explicitly model the mass dependence of the P- and S-wave components. However, the exact line-shapes are not well-known. Instead, a simplified approach is chosen in this thesis [28]. The $K^+\pi^-$ mass range is divided in bins, assuming that there is only a small variation within the respective bin. One can then replace the mass-dependent values for the amplitudes and phases by their effective value in that bin.
In this simplified strategy a correction factor has to be calculated and introduced in front of the amplitude terms h_k listed in Table 1.3. These correction factors depend on the size of the chosen mass range. For infinitely small bins they are equal to 1. Assuming P- and S-wave line-shapes, $p(m)$ and $s(m)$, and then integrating the amplitude terms over m in a certain mass bin, it turns out that those containing only pure P- and S-wave expressions remain unchanged. The three interference terms, however, have to be modified by the factor $C_{\rm SP}e^{-i\theta_{\rm SP}}$. It can be calculated by

$$\int_{m^L}^{m^H} p(m)s(m)^*\, dm(K^+\pi^-) = C_{\rm SP}e^{-i\theta_{\rm SP}}\ , \tag{1.24}$$

where * denotes the complex conjugation and m^L and m^H are the lower and higher bin boundary, respectively. Note that the line-shapes are normalised to unity in the integration range. The above formula effectively describes the coupling between the

$m(K^+\pi^-)$ [MeV]	$C_{\rm SP}$
$826 - 861$	0.984
$861 - 896$	0.946
$896 - 931$	0.948
$931 - 966$	0.985

Table 1.4: *S-P-wave correction factors using four bins of the $K^+\pi^-$ mass.*

P- and S-wave. The absolute value of the correction factor, $C_{\rm SP}$, has to be introduced in front of the three S-P-wave interference terms f_8, f_9 and f_{10}, corresponding to the mass bin. The phase $\theta_{\rm SP}$ can be absorbed by the strong phases.
As the natural decay width of the K^{*0} meson is large compared to the detector resolution, the P-wave can be described by a Breit-Wigner function

$$p(m) = \sqrt{\frac{\Gamma_{K^{*0}}/2}{\Delta\omega}} \cdot \frac{1}{m - m_{K^{*0}} + i\Gamma_{K^{*0}}/2}, \tag{1.25}$$

where $m_{K^{*0}}$ and $\Gamma_{K^{*0}}$ are the mass and the decay width of the K^{*0} meson and $\Delta\omega = \arg(m^L - m_{K^{*0}} + i\Gamma_{K^{*0}}/2) - \arg(m^H - m_{K^{*0}} + i\Gamma_{K^{*0}}/2)$. For the S-wave a flat mass dependence is assumed

$$s(m) = \frac{1}{\sqrt{m^H - m^L}}, \tag{1.26}$$

where $\sqrt{m^H - m^L}$ accounts for the normalisation. The correction factors for four equidistant bins (which are used for the analysis presented here) can be found in Table 1.4. They are close to unity.

1.4.5 Previous measurements

The polarisation amplitudes and the corresponding strong phases have been measured previously by several experiments. Here, the three most recent results by BaBar [29], Belle [30] and CDF [31] are discussed. These measurements have been performed using only a single $K^+\pi^-$ mass bin and the S-wave component has not been taken into account. The results are summarised in Table 1.5. Note that $|A_0|^2 = 1 - |A_\parallel|^2 - |A_\perp|^2$. It can be seen that the magnitudes for $|A_\parallel|^2$ and $|A_\perp|^2$ are approximately the same. Also the strong phases have similar values (mod π) but are away from 0 or π, thus showing evidence for final state interactions.
The BaBar experiment has resolved the 2-fold ambiguity mentioned above without quoting S-wave fractions in the individual bins [32, 33].

Param.	BaBar 2007 [29]	Belle 2005 [30]	CDF 2005 [31]
$\lvert A_\parallel\rvert^2$	$0.211 \pm 0.010 \pm 0.006$	$0.231 \pm 0.012 \pm 0.008$	$0.211 \pm 0.012 \pm 0.009$
$\lvert A_\perp\rvert^2$	$0.233 \pm 0.010 \pm 0.005$	$0.195 \pm 0.012 \pm 0.008$	$0.220 \pm 0.015 \pm 0.011$
$\delta_\parallel$	$-2.93 \pm 0.08 \pm 0.04$	$-2.887 \pm 0.090 \pm 0.008$	$-2.96 \pm 0.08 \pm 0.03$
$\delta_\perp$	$2.91 \pm 0.05 \pm 0.03$	$2.938 \pm 0.064 \pm 0.010$	$2.97 \pm 0.06 \pm 0.01$

Table 1.5: *Results from previous experiments where the S-wave has not been taken into account. The uncertainties are statistical and systematic, respectively.*

1.5 Probing BSM physics in $B^0 \to J/\psi K^{*0}$ decays

The analysis of $B^0 \to J/\psi K^{*0}$ decays can probe BSM physics. It is shown in [18] that this decay is very clean since the penguin contributions are very small compared to the contribution from the tree diagram. Furthermore, the weak phase of the penguin decay roughly corresponds to the phase of V_{ts} and is very small so that the two diagrams do not have a weak phase to a good approximation. Therefore, CP-violating effects are not expected in the SM. Physics BSM can affect the decay amplitudes if there are additional contributions to the penguin amplitudes such as various supersymmetric and other BSM models and thus allowing for two different weak amplitudes.
In the following it will be shown that the CP asymmetry is only different from zero if there are two non-zero phase differences. Generally, one can write for the decay amplitude

$$\Gamma(B \to f) = ae^{i\sigma_a}e^{i\delta_a} + be^{i\sigma_b}e^{i\delta_b}, \tag{1.27}$$

where $\sigma_{a,b}$ and $\delta_{a,b}$ are the weak (CP-violating) and the strong phases (CP-conserving) of the two amplitudes, respectively. The direct CPV observable can be written as

$$A_f = \frac{\Gamma(B \to f) - \Gamma(\overline{B} \to \overline{f})}{\Gamma(B \to f) + \Gamma(\overline{B} \to \overline{f})} = \frac{2ab\sin(\sigma_a - \sigma_b)\sin(\delta_a - \delta_b)}{a^2 + b^2 + 2ab\cos(\sigma_a - \sigma_b)\cos(\delta_a - \delta_b)}. \tag{1.28}$$

A non-zero CP asymmetry requires not only a non-zero weak phase difference but also a non-vanishing strong phase difference. If the strong phases are nearly the same, direct CPV cannot be observed even if BSM physics is present. Therefore, the quantity defined in Eq. 1.28 is not a good observable to find BSM phenomena.
However, in [6] it is shown that certain angular variables can also be used to test CPV beyond the SM as these observables vanish in the SM but can have significant contributions in BSM models. This is another reason for performing an angular analysis. Splitting the sample into separate K^{*0} and $\overline{K}^{*0}$ and hence, B^0 and $\overline{B}^0$ sub-samples allows to study direct CPV even if the asymmetry in Eq. 1.28 is zero. In the following $\overline{A}$ denotes the amplitudes corresponding to $\overline{B}^0$ decays. Possible CPV in mixing is neglected.
Assuming that each amplitude A_i has a CP-conserving phase δ_i and a CP-violating phase σ_i one can write

$$\widetilde{A}_i = |\widetilde{A}_i|e^{i(\delta_i + \sigma_i)}. \tag{1.29}$$

For the CP conjugated amplitudes one gets

$$\widetilde{\overline{A}}_0 = |\widetilde{A}_0|e^{i(\delta_0 - \sigma_0)}, \quad \widetilde{\overline{A}}_\parallel = |\widetilde{A}_\parallel|e^{i(\delta_\parallel - \sigma_\parallel)}, \quad \widetilde{\overline{A}}_\perp = -|\widetilde{A}_\perp|e^{i(\delta_\perp - \sigma_\perp)} \tag{1.30}$$

The most familiar manifestation of direct CPV is in partial rate asymmetries which can be realised in the first three terms of Eq. 1.22 for B^0 and $\overline{B}^0$ decays separately.

Parameter	B^0	$\overline{B}^0$
$\lvert A_\parallel\rvert^2$	0.216 ± 0.017	0.244 ± 0.018
$\lvert A_\perp\rvert^2$	0.213 ± 0.017	0.178 ± 0.017
$\delta_\parallel$	-2.934 ± 0.134	-2.851 ± 0.114
$\delta_\perp$	2.878 ± 0.088	2.993 ± 0.089

Table 1.6: *Measurements by Belle of the amplitudes and strong phases for $B^0 \to J/\psi K^{*0}$ and $\overline{B}^0 \to J/\psi \overline{K}^{*0}$ decays separately [30]. Only the statistical error is quoted.*

Partial rate asymmetries can appear in either of the terms. In practise, these effects would manifest themselves in different transversity amplitudes when splitting in B^0 and $\overline{B}^0$ decays. This can be easily measured and the results of such a measurement are presented in this thesis.
The aforementioned differences are expected to be rather small. In principle, information can also be extracted from the terms 4 to 6 in Eq. 1.22. Using these coefficients, assuming the presence of CP-violating phases, one gets modified coefficient terms h'_4, h'_5 and h'_6 which can be used to determine the following quantities

$$\begin{aligned} a = h'_4 + \overline{h}'_4 &= \quad 2|A_\perp||A_\parallel| \cos(\delta_\parallel - \delta_\perp) \sin(\sigma_\parallel - \sigma_\perp), \\ b = h'_5 - \overline{h}'_5 &= -2|A_\parallel||A_0| \sin(\delta_\parallel - \delta_0) \sin(\sigma_\parallel - \sigma_0), \\ c = h'_6 + \overline{h}'_6 &= -2|A_\perp||A_0| \cos(\delta_\perp - \delta_0) \sin(\sigma_\perp - \sigma_0). \end{aligned} \tag{1.31}$$

These observables are particularly sensitive to CP-violating phases even if the strong phase differences vanish. However, it is technically not easy to extract these interference terms.
There are several BSM approaches which explain an enhancement of the penguin amplitude. One example is the so-called supersymmetric right-handed flavour mixing scenario which is detailed in [8]. Deviations of quantities as defined in Eq. 1.31 from zero can be of the order of a few percent at maximum as the ratio of the (BSM) penguin amplitude to the (SM) tree amplitude is suppressed. Deviations of the order of one, however, can be expected in pure penguin decays, like $B^0 \to \phi K^{*0}$.
The Belle experiment has measured the decay amplitudes and the strong phases separately for B^0 and $\overline{B}^0$ decays, testing possible direct CPV effects [30]. The results can be seen in Table 1.6; the values for both decays are consistent within the errors. Belle has also measured quantities as defined in Eq. 1.31, seeing no evidence for BSM physics.

Chapter 2

The LHCb detector

> It doesn't matter how beautiful your theory is, it doesn't matter how smart you are. If it doesn't agree with experiment, it's wrong.
>
> *Richard Feynman (1918-1988)*

In this chapter the Large Hadron Collider and its four main experiments are briefly discussed, followed by a detailed presentation of the LHCb experiment. The main focus is put on the tracking detectors, the particle identification and the trigger system.

2.1 The Large Hadron Collider

The currently largest facility of particle physics is the LHC [34], located at CERN in Geneva, Switzerland. It is a proton-proton (pp) collider where two proton beams are accelarated in a tunnel with a circumference of 27 km. The beams are brought to collision at four interaction points, where particle detectors are installed to analyse the remnants of the collisions: the ATLAS (A Toroidal LHC Apparatus [35]), CMS (Compact-Muon-Solenoid [36]), ALICE (A Large Ion Collider Experiment [37]) and LHCb (Large Hadron Collider beauty [38]) detector. The former two experiments are general purpose detectors, ALICE is investigating the properties of quark-gluon plasma in heavy ion collisions and LHCb is dedicated to measure decays of b- and c-hadrons. A visualisation of the location of the tunnel and the four experiments can be found in Fig. 2.1.
The LHC is intended to operate at a centre-of-mass energy of $\sqrt{s} = 14$ TeV and a luminosity of $10^{34}\,\mathrm{cm}^{-2}\mathrm{s}^{-1}$. Then, the protons are packed in 2808 bunches per proton beam with a spacing of 25 ns. To force the protons on the circular orbits, superconducting magnets with a peak dipole field of 8.33 T are required. The LHCb experiments has a design luminosity of $10^{32}\,\mathrm{cm}^{-2}\mathrm{s}^{-1}$. This decreases the number of primary interactions per bunch crossing which allows a full and efficient event reconstruction [34].

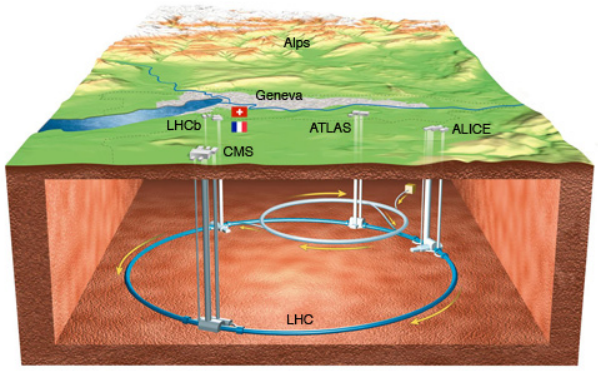

Figure 2.1: *Location of the LHC tunnel and the four main experiments ATLAS, CMS, ALICE and LHCb. Figure from [39].*

The LHC has a history of three years of data taking. In 2010 and 2011 the data were collected at a centre-of-mass energy of $\sqrt{s} = 7$ TeV which was increased to 8 TeV in 2012. The delivered instantaneous luminosity to the LHCb experiment was $2 \cdot 10^{32}\,\mathrm{cm}^{-2}\mathrm{s}^{-1}$ in 2010 and was then increased to $4 \cdot 10^{32}\,\mathrm{cm}^{-2}\mathrm{s}^{-1}$, i.e. LHCb has been operating above design luminosity. The experiment recorded an integrated luminosity, $\mathcal{L}_{\mathrm{int}}$, of 0.04 fb^{-1} in 2010, 1.1 fb^{-1} in 2011 and 2.08 fb^{-1} in 2012. This is summarised in Fig. 2.2. It can be seen that the efficiency of the data taking, i.e. the ratio between the recorded luminosity and the integrated luminosity delivered to the LHCb experiment is very high, in 2011 it was approximately 90%. The analysis presented here is restricted to the data collected in 2011 [40].
In the energy range of the LHC b-quarks are mainly produced in pairs by means of inelastic pp collisions [41]. The leading order Feynman diagrams are shown in Fig. 2.3 where the pairs are created by quark-antiquark annihilation or gluon fusion. For the calculation of the $b\bar{b}$ cross-section also higher order corrections (flavour

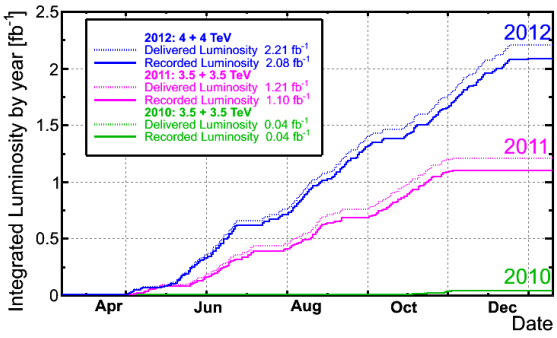

Figure 2.2: *Summary of the recorded integrated luminosity at LHCb in the three years of operation. Figure from [40].*

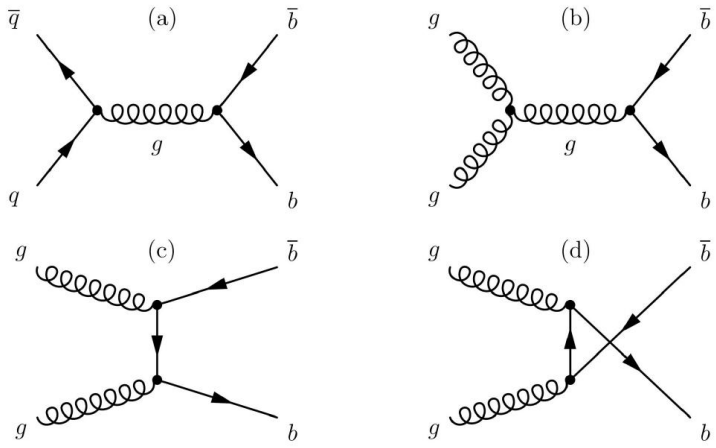

Figure 2.3: *Leading order Feynman diagrams of b-hadron production: (a) quark-antiquark annihilation, (b)-(d) gluon fusion. Fig. from [41].*

excitation and gluon splitting) have to be taken into account. This cross-section for inelastic pp collisions at a centre-of-mass energy of 7 TeV has been measured by LHCb to be [42]

$$\sigma_{b\bar{b}} = \sigma(pp \to b\bar{b}X) = (288 \pm 4 \pm 48)\mu\text{b}, \tag{2.1}$$

using J/ψ mesons from b-hadron decays. The large systematic error is mainly due

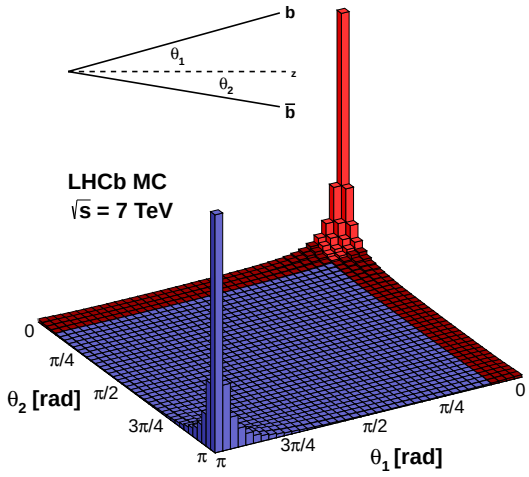

Figure 2.4: *The plot shows the distribution of the angle between the b ($\bar{b}$) quark and the beam axis z using simulated events. Figure from [40].*

to the tracking efficiency and the luminosity determination. In 2011, an integrated luminosity of $1.1\,\mathrm{fb}^{-1}$ has been recorded. By multiplying this number by the cross-section one obtains a number of $b\bar{b}$ pairs of approximately $3 \cdot 10^{11}$ of which roughly 25% are produced in the geometric acceptance of the LHCb detector. As it is unlikely that both gluons or quarks producing the $b\bar{b}$ pair carry the same fraction of the proton momentum, the $b\bar{b}$ pairs are boosted in the direction of the beam axis and therefore produced predominantly in the forward or backward direction. This can be seen from Fig. 2.4 where the distribution of the angle between the b ($\bar{b}$) quark and the beam axis z is shown. Simulated events at $\sqrt{s} = 7$ TeV have been used to produce the plot.

2.2 The LHCb experiment

As $b\bar{b}$ pairs are predominantly produced in the forward or backward direction, the LHCb detector is built as a forward spectrometer. Its design is visualised in Fig. 2.5. The z-axis is defined in the direction of the beam axis, the y-axis points to the vertical direction. The geometrical acceptance of the detector ranges from 10 to 300 mrad in the bending plane of the dipole magnet (x-z-plane) and from 10 to 250 mrad in the non-bending plane (y-z-plane).
The detector consists of the following components which are discussed in the course of this section in more detail: Surrounding the region of the pp interaction the

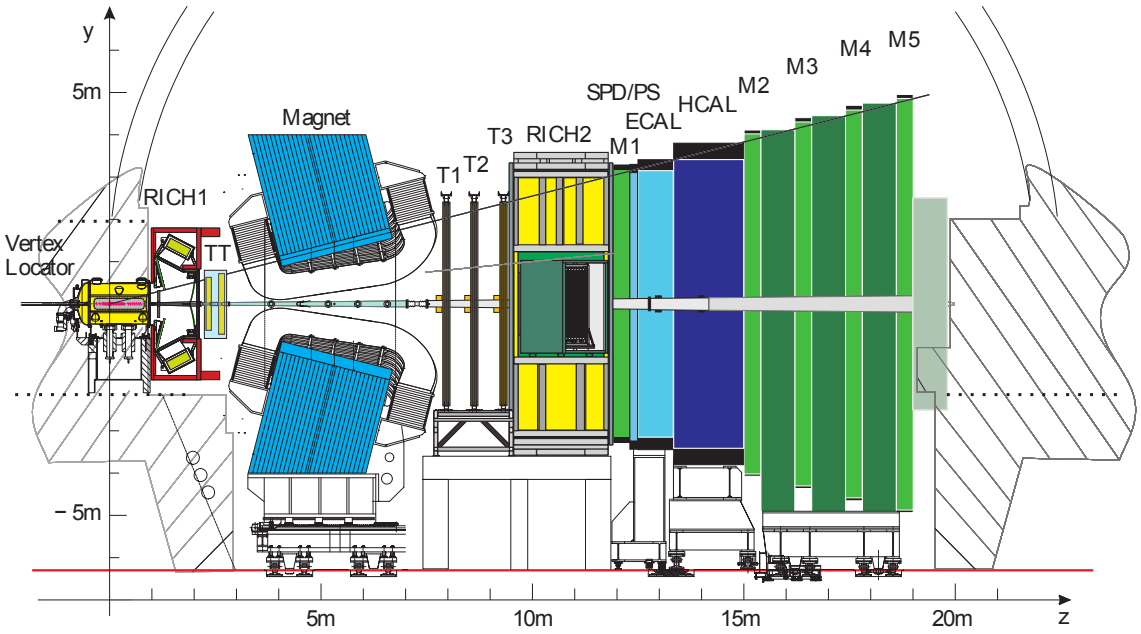

Figure 2.5: *Schematic view of the LHCb detector. Figure from [38], modifications courtesy of M. Meißner.*

VErtex LOcator (VELO) provides a very good spatial resolution of reconstructed vertices. Further tracking detectors consist of the Tracker Turicensis (TT) before and three tracking stations T1, T2, T3 after the dipole magnet. These sub-detector components are designed to measure the signatures that the final state charged particles leave on their way through the detector (so-called tracks). The three tracking stations are composed of two parts, the Inner Tracker (IT) covering the area around the beam axis and the Outer Tracker (OT) covering the outer regions of the detector acceptance.
For particle identification two ring-imaging Cherenkov detectors (RICH1 and RICH2) are installed, one before and one after the dipole magnet. They are mainly used to distinguish between kaons, pions and protons. After the RICH2 there is a Scintillating Pad Detector (SPD) and a Pre-Shower detector (PS or PRS), followed by an Electromagnetic (ECAL) and a Hadronic CALorimeter (HCAL). To detect muons five dedicated chambers (M1-M5) are used, one of them placed before the other four behind the calorimeter [38].

2.2.1 Tracking detectors

The tracking detectors are installed to measure the momentum of charged particles. Their trajectories leave signatures in the VELO and TT before the magnet and the tracking chambers after the magnet and are bent by the homogeneous magnetic field according to their momentum. The dipole magnet is not superconducting and its bending plane is in x-z direction. For tracks of a length of 10 m the integrated magnetic field is 4 Tm. To achieve the desired momentum resolution, the magnetic field integral $\int B \, \mathrm{d}l$ has to be known with a relative precision of roughly 10^{-4} and the position of the B-field with an accuracy of a few mm. The polarity of the magnetic field can be switched in order to precisely measure detector asymmetries of charged particles. The information presented in this subsection is based on [38].

The Vertex Locator
The VELO is intended to measure the coordinates of tracks close to the collision point. This is especially important for the measurment of the primary vertex (the location of the pp collision) and displaced secondary vertices. b-hadrons have a relatively large average lifetime and travel about 1 cm before they decay. The detector is composed of 21 pairs of silicon modules to measure the radial coordinate r and the azimuthal angle ϕ. These modules are installed along the direction of the beam axis with a distance of 2 mm between them. In addition, two stations are arranged perpendicular to the beam axis in the backward (upstream) direction. This is the so-called pile-up veto system. It is only used in the trigger system. A sketch of the VELO setup can be seen in Fig. 2.6. Each module consists of two sensors, the r- and the ϕ-sensors, with a thickness of 300 μm. The unusual cylindrical geometry was chosen instead of a rectangular scheme to allow a fast reconstruction of tracks and vertices in the trigger. The r-ϕ-geometry of the VELO is visualised in Fig. 2.7.

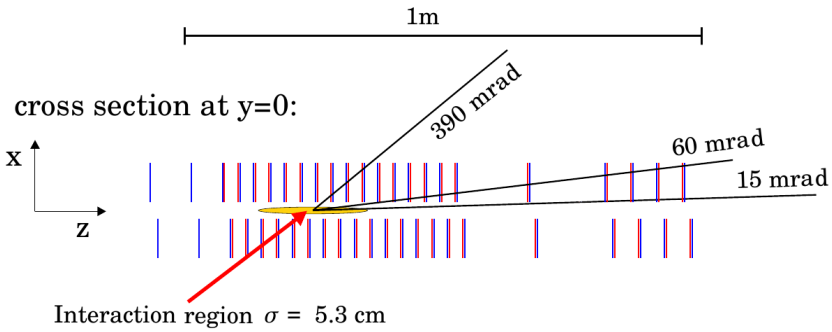

Figure 2.6: *Schematic view of the* 21 *VELO stations in the x-z-plane. Figure from [43] (originally in [38]).*

The sensor segments are divided in four 45° regions to minimise the occupancy. The pitches between the sensors get larger with linearly increasing distance from the beam axis, from 38 μm to 97 μm for the r-sensors and to 102 μm for the ϕ-sensors. Within a module the sensor alignment is better than 20 μm. The VELO detector is a moveable device. In order to precisely measure tracks and vertices it can be positioned very close to the interaction point. The sensitive region starts at a distance of approximately 8 mm from the beam axis. The exact position of the detector depends on the beam conditions and can vary from proton fill to poton fill. Before stable proton beams are achieved, the VELO is moved away from the interaction region to avoid any damage.

The Tracker Turicensis

The TT is located before the dipole magnet and consists of silicon strips. There are four detection layers which are installed in pairs, the so-called (x, u) and (v, x)

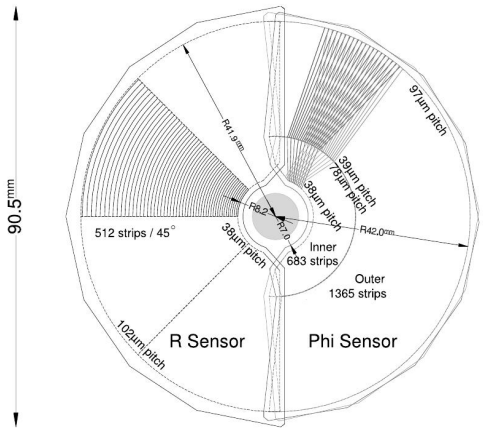

Figure 2.7: *The r-ϕ-geometry of the VELO sensors. Figure from [38].*

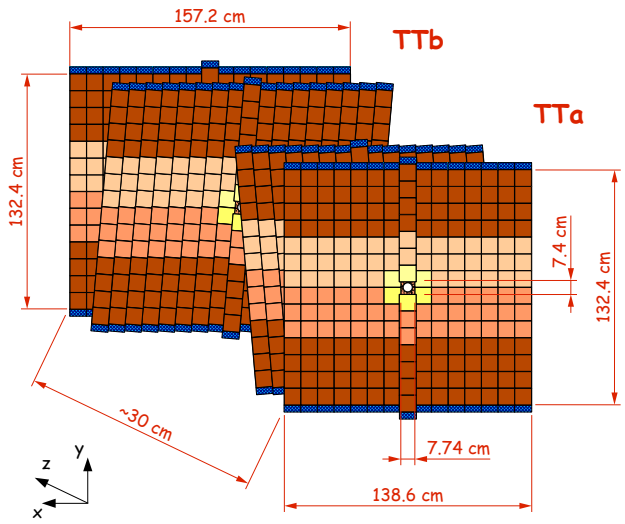

Figure 2.8: *Basic geometry of the TT detector. Figure from [44].*

stations. These stations are approximately 130 mm high and 145 mm wide and separated by 27 cm. The u- and v-layers are rotated by a stereo angle of $\pm 5°$ with respect to the vertically orientated x-layers. This geometry has been chosen to have also resolution in y-direction. The basic geometrical layout can be seen in Fig. 2.8. One half module consists of a row of seven silicon sensors. These sensors are 500 μm thick and have a pitch of 183 μm. The detector is read out from the top and the bottom and the resolution of a single track is approximately 50 μm.

The Inner Tracker

Downstream of the dipole magnet there are three tracking stations. The region around the beam pipe is covered by the IT, a silicon strip detector. It has the form of a cross with a total width of 125 mm and a height of 40 cm. The active area covers approximately 4 m^2. Similar to the TT, for each of the three stations there are four layers in a (x, u, v, x) scheme where the u and v layers are rotated by $\pm 5°$. The geometry of an x-layer is shown in Fig. 2.13. Either one or two silicon strips are combined to one module. The sensor thickness is 320 μm for the regions above and below the beam axis and 410 μm for the areas on either side of the beam pipe. The strip pitch amounts to roughly 200 μm and, like for the TT, the resolution of a single track is approximately 50 μm. The thickness has been chosen in that way to ensure a high signal-to-noise level while at the same time reducing the material budget of the detector.

The Outer Tracker

The OT is a gas detector with the purpose of reconstructing tracks over a large

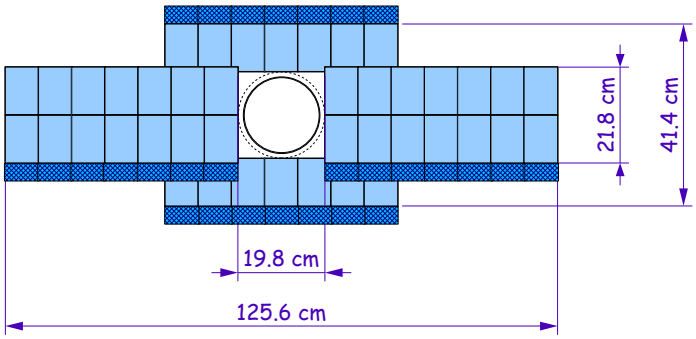

Figure 2.9: *Basic geometry of an IT x-layer. The shaded blue areas indicate the readout electronics. Figure from [44].*

region and measuring their momentum. The detector is based on the straw-tube technology. The straw-tubes themselves are composed of double layers, so-called monolayers. The tubes have an inner diameter of 4.9 mm and a pitch of 5.25 mm. As counting gas a mixture of argon (70%), CO_2 (28.5%) and O_2 (1.5%) is chosen. This ensures a fast drift time that is below 50 ns for the mean drift path of 2.45 mm and a spatial resolution of about 200 μm. In the centre of each straw there is a wire serving as anode, being 25 μm thick. The geometry corresponds to that of the IT, i.e. it has four layers per station, two of them tilted by $\pm 5°$. The outer boundary of the stations corresponds to an acceptance of 300 mrad in the bending plane and 250 mrad in the non-bending plane. The full detector is made up out of 168 long and 96 short modules and roughly $53\,760$ straw-tube channels. Due to the light materials chosen, the detector only corresponds to 10% of a radiation length. The cross-section of an OT station and the layout of a straw-tube module can be seen in Fig. 2.10.

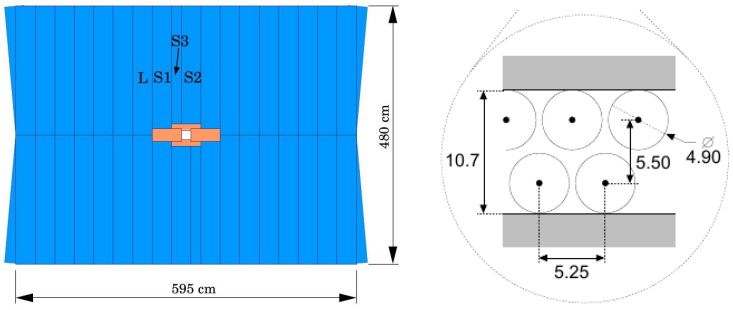

Figure 2.10: *Basic geometry of (a) an OT station (from [43], originally in [45]) and (b) a straw-tube module (numbers in mm, from [38]).*

Reconstruction of tracks
All three tracking detectors, the VELO, the TT and the three tracking stations (IT and OT) are used to reconstruct tracks and determine the momentum of charged particles. There are five different track categories (see [46]):

1. **VELO tracks** leave only signatures (hits) in the modules of the Vertex Locator.
2. **T-tracks** are only composed of hits left in the three tracking stations.
3. **Downstream tracks** are T-tracks with additional hits from the TT detector.
4. **Upstream tracks** have signatures in both the VELO and TT, i.e. they leave the detector right after the magnet due to their low momentum.
5. **Long tracks** are reconstructed from hits in the VELO and the tracking stations. Only these tracks are used in this analysis as they give the most accurate momentum estimate of all track categories.

Two different algorithms are used to reconstruct long tracks [46]. They both use track segments in the VELO and the three tracking stations which are then combined to the full track. A momentum estimate is calculated by a fit to the measurements in the sub-detectors. In the **Forward Tracking** algorithm a VELO segment and one hit in the tracking stations are combined. Additional hits in the tracking stations are taken into account. These hits and the resulting track have to satisfy various requirements to be chosen as long track. Hits in the TT that are close enough to the selected track are considered as well. The approach of the **Track Matching** algorithm is to combine VELO and T-tracks by extrapolation. TT-hits are again taken into account if they are close to the selected long track.
The momentum measurement has a high resolution, varying from 0.4% for a momentum of 5 GeV to 0.6% for a momentum of 100 GeV. The spatial resolution is approximately 20 μm for tracks with a high transverse momentum [19].

2.2.2 Particle identification

After the momentum estimate the particle type has to be determined. In the decay investigated in this thesis it is especially important to distinguish between kaons and pions. This is mainly achieved with the two RICH detectors. This subsection is based on [38].

The RICH detectors
Cherenkov detectors are based on the fact that charged particles passing through a medium of refraction index n with a velocity v larger than the speed of light in that medium, $c' = \frac{c}{n}$, emit photons along a cone with the opening angle

$$\cos\theta_{\mathrm{C}} = \frac{1}{\beta n}, \tag{2.2}$$

where $\beta = \frac{v}{c}$. By measuring the opening angle and estimating the momentum as explained above the mass of the particle can be inferred. There are two RICH detectors that cover different momentum ranges. The first one is installed before the dipole magnet and is intended to measure the opening angles of charged particles with momenta between 1 and 60 GeV. As radiator material aerogel and C_4F_{10} is used. The second one is placed behind the tracking stations, covers particle momenta between 15 and 100 GeV and uses CF_4 as radiator material. RICH1 covers a very wide acceptance range from ± 25 to ± 300 mrad in the horizontal plane and from ± 15 up to ± 250 mrad in the vertical plane. In both detectors, the Cherenkov light is focussed by means of spherical and flat mirrors to reflect the image out of the detector acceptance. The Cherenkov photons are in the visible spectrum ($200 - 600$ nm) and are detected by Hybrid Photon Detectors. These detectors are shielded by iron to protect them from the magnetic field. The layout of both detectors can be seen in Fig. 2.11. The misidentification rate for pions is approximately 10%. This number and more information on the RICH performance can be found in [47].

The calorimeter

The task of the calorimeter is to identify electrons, photons and hadrons, to measure their energy and position and to give an input to the first stage of the trigger system. Particles produce showers of secondary particles in the calorimeter. The corresponding scintillation light is then detected. The calorimeter system consists of

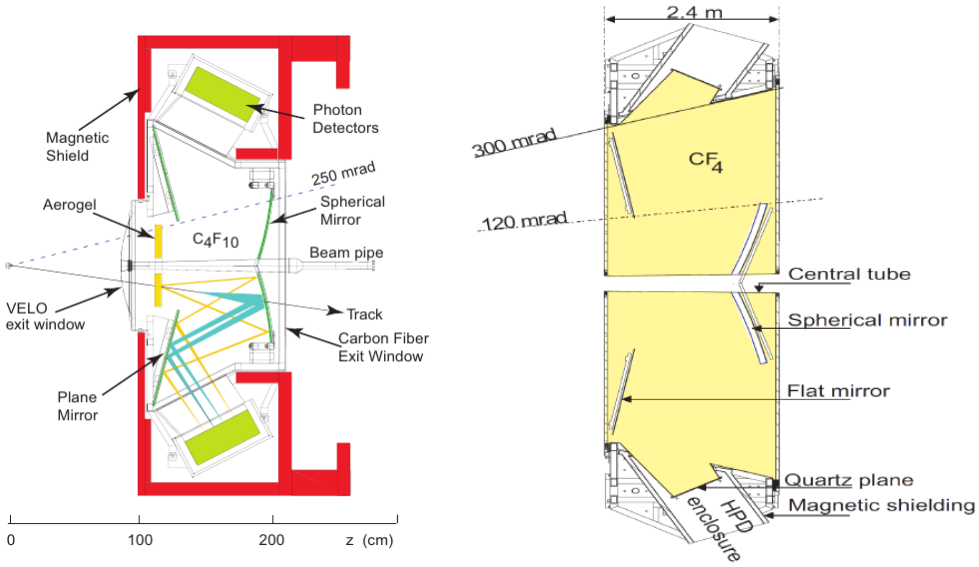

(a) (b)

Figure 2.11: *Schematic layout of (a) the RICH1 (side view) and (b) the RICH2 (top view) detector. Figures from [38].*

four main components:

1. The **Scintillator Pad Detector (SPD)** is the most upstream detector positioned directly behind the first muon station. It is composed of 15 mm thick scintillating layers and serves mainly to distinguish between electrons and photons as only charged particles can be detected. Behind the SPD there is a lead converter corresponding to 2.5 radiation lengths to initiate electromagnetic showers.

2. The **Preshower Detector (PS or PRS)** is composed in the same way as the SPD (a 15 mm thick layer of scintillators). As hadrons initiate only small showers in this detector, its main purpose is to distinguish hadronic from electromagnetic showers.

3. The **Electromagnetic CALorimeter (ECAL)** is a so-called shashlik detector as it is composed of alternating layers of lead (2 mm thick) and scintillator pads (4 mm thick). In total there are 66 layers, corresponding to 25 interaction lengths. Its main purpose is to detect showers initiated by electrons and photons. For the energy resolution one obtains

$$\frac{\sigma(E)}{E} = \frac{10\%}{\sqrt{E}} \oplus 1.5\%, \tag{2.3}$$

   where $\oplus$ denotes quadratic summation. The energy is measured in GeV.

4. The structure of the **Hadronic CALorimeter (HCAL)** is similar to that of the ECAL, consisting of alternating iron and scintillator plates serving as absorber and active material, respectively. The purpose of the HCAL is to detect showers initiated by hadrons. However, contrary to the ECAL the layers are oriented parallel to the beam axis. The 1 cm thick iron plates are installed in the transverse direction. The length of one layer corresponds to the hadronic interaction length. In total, approximately $86,000$ tiles have been used. The energy resolution is given by

$$\frac{\sigma(E)}{E} = \frac{80\%}{\sqrt{E}} \oplus 10\%. \tag{2.4}$$

Figure 2.12 shows an overview of the purpose of each calorimeter component and a schematic view of the HCAL.

The muon stations

Muons are an integral part in many important measurements at LHCb, especially for the determination of CP asymmetries. Also, the decay analysed in this thesis has two muons in the final state. The muon system provides an important input to the hardware and software stages of the trigger. The detector consists of five stations,

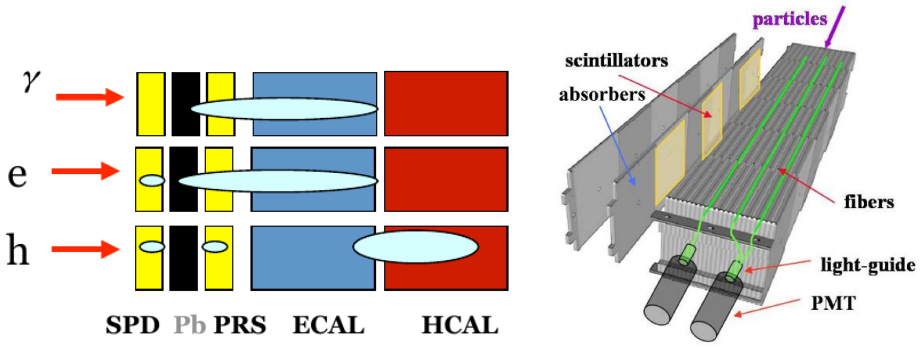

(a) (b)

Figure 2.12: *Schematic overview of (a) the functions of the four calorimeter components (from [48]) and (b) the cell structure of the HCAL (from [38]).*

one installed before the calorimeter and four being placed at the end of the detector. All five stations are composed of 1380 chambers in total. The acceptance range includes roughly 20% of the muons from inclusive semileptonic b-decays. The stations M2-M5 are interleaved with 80 cm thick iron absorbers to avoid the penetration of hadrons. The main purpose of M1 is to improve the measurement of the transverse momentum in the trigger. Only muons with a momentum larger than 6 GeV cross the entire muon detector since the total thickness of all absorbers (calorimeter and

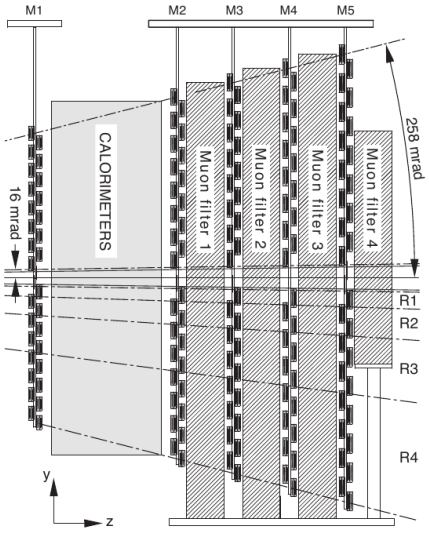

Figure 2.13: *Schematic view of the muon stations. Figure from [38].*

muon system) amounts to 20 hadronic interaction lengths. The first three muon stations have a very high spatial resolution in the bending plane in order to measure the direction of the track and the transverse momentum of the muon candidate (resolution of 20%). The last two stations have a limited resolution, they are mainly built to identify the muons passing through the detector. The stations consist of Multi-Wire Proportional Chambers, except for the region of M1 that is close to the beam axis. There, Gas Electron Multipliers are used.

Particle hypothesis
The information obtained from the RICH detectors, the calorimeter and the muon system is used to determine the probability of a particle hypothesis x by associating a likelihood value $\mathcal{L}_x$ to the corresponding track. This likelihood value is mostly calculated relative to the pion π, i.e. differences of (logarithmic) likelihood values are determined:

$$\Delta \ln \mathcal{L}_{x\pi} = \ln \mathcal{L}_x - \ln \mathcal{L}_\pi. \tag{2.5}$$

If $\Delta \ln \mathcal{L}_{x\pi} > 0$, then the reconstructed track can be more likely associated to a particle x than to a pion. Analogously, the difference $\Delta \ln \mathcal{L}_{xp}$ is defined, where p denotes a proton.
In the analysis presented here particle identification plays an important role. Variables like that defined in Eq. 2.5 are used to distinguish pions from kaons and kaons from protons, see Table 3.1.

2.2.3 The trigger system

The LHCb experiment operates at a lower luminosity as ATLAS and CMS. The main reason for this is to limit the number of interactions per bunch crossing to one or two at most which ensures a fast and efficient track reconstruction. Nevertheless, the event rate is very large. The nominal rate, including empty bunches, is 40 MHz. This is also the number quoted in Fig. 2.14 which shows the working principle of the trigger. For most of the running periods in 2011 and 2012 the event rate was at approximately 15 MHz (only 50% of the possible RF bunches were filled with protons). The purpose of the trigger is to reduce this rate to about 5 kHz at which the data can be written to the storage. The trigger has to work very fast while still retaining events interesting for LHCb analyses. This is achieved by a trigger system that consists of two stages (subsection is based on [38]):

1. The **Level-0 trigger (L0)** is a hardware trigger intended to reduce the event rate below 1 MHz. For charged hadrons this number is around 450 kHz, for muons 400 kHz and for electron and photons 150 kHz. Generally, the L0 intends to select those electron, photon and hadron clusters in the calorimeter with the highest transverse energy and those two muons with the highest transverse momentum.

The L0 can itself be sub-divided in three parts: The *L0 pile-up trigger* attempts to distinguish between events with only one or more interactions per bunch crossing by taking advantage of the pile-up sensors of the VELO. In most of the physics analyses this information is not used. The *L0 calorimeter trigger* selects calorimeter clusters with high transverse energy. This is done by adding 2x2 calorimeter cells. Furthermore, a first particle hypothesis is assigned based on the information from the calorimeter components. The *L0 muon trigger* selects the two muons with the highest transverse momentum in each quadrant of the muon stations. The corresponding event is accepted by the trigger if one of the two transverse momenta or the product of both is above a certain threshold.
The time between the pp interaction and the L0 decision (based on the three parts explained above) is around $4\ \mu$s.

2. All events that pass the L0 are processed by the software based **High Level Trigger (HLT)**. It consists of two components, the *HLT1* and the *HLT2*, that are intended to reduce the event rates to around 50 kHz and 5 kHz, respectively.
LHCb performs a wide range of physics analyses. Therefore, every analysis uses a specified trigger configuration (or trigger line) with process specific trig-

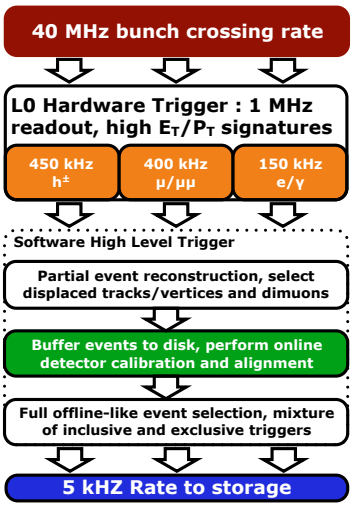

Figure 2.14: *Working principle of the LHCb trigger system. Note that the bunch crossing rate given here is only the nominal rate also including empty bunches. For most of the data taking the number had been around* 15 *MHz. Figure from [40].*

ger algorithms, reconstruction methods and selection criteria. These trigger lines do not depend upon the events triggered by the L0. The HLT1 performs a partial event reconstruction and selects displaced tracks or vertices and dimuon candidates. For the events passing this stage a detector calibration and alignment is performed. The HLT2 does a first full event reconstruction intended to be as close to the final, offline, reconstruction as possible. Various inclusive and exclusive trigger selections are performed to achieve the intended event rate.

More information on the trigger strategy for the decay analysed here is given in Sec.3.3. More details on the trigger system can be found in [38].

Chapter 3

Selection of signal candidates

A good decision is based on knowledge and not on numbers.

Plato (428/427 BC - 348/347 BC)

The first step in the analysis presented in this thesis is the reconstruction and selection of $B^0 \to J/\psi K^{*0}$ candidates. This chapter details the applied selection criteria and the trigger strategy. Furthermore, it is explained how the angular and decay time acceptances are determined.

3.1 Selection of $B^0 \to J/\psi K^{*0}$ candidates

The data sample used is polluted by background. This can be physical background, where similar decays are (partially) reconstructed and taken as the signal decay, or a background component, where one or more of the final state particles are randomly combined to form a signal-like signature. The case where all four final state particles are chosen randomly is called combinatorial background. As the background decreases the sensitivity to the observables, it is very important to reduce the background level as much as possible while maintaining a high signal yield.
The data analysed in this thesis were collected in proton-proton collisions at a centre-of-mass energy of $\sqrt{s} = 7$ TeV with the LHCb detector, amounting to an integrated luminosity of approximately 1 fb^{-1}. This corresponds to the full data set taken in 2011. During data taking, both the hardware and the software stage of the trigger are applied to filter the events. The remaining candidates are further processed by the LHCb reconstruction software (Brunel, [49]) and the LHCb analysis software (DaVinci, [50]) where a pre-selection is performed. Finally, an offline selection is applied to further reduce the background [19].
Several studies like the determination of the detector acceptances rely on simulated events. For this purpose a sample of 10 million $B^0 \to J/\psi K^{*0}$ events was generated. Proton-proton collisions are simulated using the Monte Carlo event generator Phythia 6.4 [51], in a specific LHCb configuration (Gauss, [52]). The B-hadron decays

are described by the EvtGen package [53], in which final state radiation is simulated using Photos [54]. Each event contains at least one $B^0 \to J/\psi K^{*0}$ candidate. Only events in the range from 0 to 400 mrad around the beam pipe (roughly corresponding to the detector acceptance) are further processed, for which the detector response is simulated using the Geant4 software [55] as described in [56].
To allow for comparisons between data and simulation, the trigger criteria are also applied to the simulation and the selection requirements are the same for both samples.
The B^0 meson is produced directly in the proton-proton interaction (at the so-called primary vertex, PV). After an average flight distance of approximately 1 cm, it decays weakly to two vector mesons, the J/ψ and the K^{*0}, with a branching fraction of $\mathcal{B}(B^0 \to J/\psi K^{*0}) = (1.34 \pm 0.06) \cdot 10^{-3}$ [5]. The S-wave subtracted branching fraction is $(1.29 \pm 0.14) \cdot 10^{-3}$ [57]. Both mesons decay into a pair of muons and a kaon and pion, respectively, with branching fractions of $\mathcal{B}(J/\psi \to \mu^+\mu^-) = (5.93 \pm 0.06)\%$ [5] and $\mathcal{B}(K^{*0} \to K^+\pi^-) \simeq 2/3$ [5]. The muons, kaons and pions do not decay within the detector and are therefore considered as stable. The total visible branching fraction for the decay $B^0 \to J/\psi(\mu^+\mu^-)K^{*0}(K^+\pi^-)$ is then $\mathcal{B}_{\text{vis}} \simeq 5.30 \cdot 10^{-5}$.

3.2 Trigger strategy

Before the offline selection, described in the next section, a decay specific trigger algorithm [58] is applied to perform a preliminary reconstruction and mainly to reduce the data to an amount which is recordable, keeping only potentially interesting events. The trigger configurations (so-called trigger lines) are based on reconstructed single muons or muon pairs and partially on the decay time of the B^0 which helps in reducing background. As the trigger lines can introduce biases, the strategy is to use as few lines as possible while retaining a high signal yield. The trigger system has been introduced in Subsec. 2.2.3.
On the hardware (L0) stage two trigger configurations are selected for this analysis: The single-muon and the dimuon line. The first requires a single muon candidate with a transverse momentum larger than 1.4 GeV, whereas the latter requires two muon candidates with a transverse momentum larger than 0.56 GeV and 0.48 GeV, respectively. All candidates passing the hardware trigger are passed on to the software stage. In the first stage (HLT1), a partial reconstruction is performed, confirming or discarding the L0 decision. For this analysis the trigger line HLT1DiMuonHighMass is chosen. It requires two oppositely-charged muons with an invariant mass larger than 2.7 GeV. In addition, a transverse muon momentum larger than 0.5 GeV and a muon momentum larger than 6 GeV is required. The track fit to the muon hits in the vertex detector and the tracking stations has to have a χ^2 divided by the number of degrees of freedom, $\chi^2_{\text{track}}/\text{nDoF}$, of smaller than 4. The second stage of the software trigger (HLT2) requires a full reconstruc-

tion of the J/ψ meson. Here, the HLT2DiMuonDetachedJpsi trigger configuration is used. Only dimuon pairs with an invariant mass within 120 MeV of the known J/ψ mass [5] are selected. Quality requirements on the muon tracks and the fit of the J/ψ vertex are applied, such that $\chi^2_{\text{track}}/\text{nDoF} < 5$ and $\chi^2_{\text{vtx}}(J/\psi)/\text{nDoF} < 25$. In addition, a cut on the decay length (DL) significance $\text{DL}/\sigma_{\text{DL}}$ of the J/ψ with respect to the PV to which the J/ψ has the smallest impact parameter is required, $\text{DL}/\sigma_{\text{DL}} > 3$. The impact parameter (IP) is defined as the distance of closest approach of a track to the PV. This cut exploits the long lifetime of the B^0 meson to identify J/ψ mesons from B^0 decays and suppresses so-called prompt background, where either the J/ψ or the K^{*0} meson originates from the PV and not from the B^0 candidate, but introduces a bias on the decay time distribution as B^0 candidates with a higher decay time are more likely to pass the criterion. Since the time and angular parts of the decay amplitude separate, this has no influence on the angular observables.

3.3 Offline selection

The full list of offline selection criteria can be seen in Table 3.1. The selection is mainly based on the requirements for $B^0_s \to J/\psi\phi$ and related decays which have been optimised to maximise the sensitivity on the main observables and reduce the background level, see [58, 59, 60]. The criteria especially adapted for $B^0 \to J/\psi K^{*0}$ decays are highlighted in red. They further reduce the background by a significant margin (see next section).
The offline selection requirements can be divided in four parts:

The **four stable particles** in the final state leave signatures in the detector which can be reconstructed as a track and extrapolated back to the decay point (secondary vertex) of the B^0 meson. The J/ψ and K^{*0} mesons have a lifetime that is only approximately 10^{-20} s [5]. Hence, they are assumed to decay "instantaneously". Certain requirements have to be fulfilled by these tracks in order to be selected: The quality of the track fit is required to have a $\chi^2_{\text{track}}/\text{nDoF}$ smaller than 4. The cut value does not have necessarily to be chosen exactly at 4 to meet the goals of the selection but has been applied as a common requirement for various $B \to J/\psi X$ decays. This statement is also valid for other selection criteria where no specific statement is made. Furthermore, it can happen that the detector signature of a particle is used twice to fit a track. These additional tracks are called clones which can be reduced by using a minimum distance between the track in consideration with respect to all other tracks, the so-called Kullback-Liebler clone distance [61]. More precisely, this distance is a measure for the difference in information content between two tracks. Thus, the larger the clone distance the smaller the probability that the track is a clone. On average, rejecting tracks with clone distances smaller than 5000 reduces the clone fraction to approximately three per mille with an effi-

Decay mode	Cut parameter	Selection criterion
μ^+, μ^-, K^+, π^-	$\chi^2_{\text{track}}/\text{nDoF}$	< 4
	clone distance	> 5000
$J/\psi \to \mu^+\mu^-$	$\Delta \ln \mathcal{L}_{\mu\pi}(\mu)$	> 0
	$\min(p_{\text{T}}(\mu^+), p_{\text{T}}(\mu^-))$	> 0.5 GeV
	$\chi^2_{\text{vtx}}(J/\psi)/\text{nDoF}$	< 16
	$m(J/\psi)$	$\in [3030, 3150]$ MeV
$K^{*0} \to K^+\pi^-$	$\Delta \ln \mathcal{L}_{K\pi}(K)$	> 0
	$\Delta \ln \mathcal{L}_{Kp}(K)$	> -2
	$\Delta \ln \mathcal{L}_{K\pi}(\pi)$	< 0
	$p_{\text{T}}(K^{*0})$	> 2 GeV
	$m(K^{*0})$	$\in [826, 966]$ MeV
	$\chi^2_{\text{vtx}}(K^{*0})/\text{nDoF}$	< 16
$B^0 \to J/\psi K^{*0}$	$m(B^0)$	$\in [5150, 5400]$ MeV
	$\chi^2_{\text{vtx}}(B^0)/\text{nDoF}$	< 10
	$\chi^2_{\text{DTF}}(B^0)/\text{nDoF}$	< 5
	$\chi^2_{\text{IP}}(B^0)$	< 25
	$\chi^2_{\text{IP,next}}(B^0)$	> 50
	$t(B^0)$	$\in [0.3, 14]$ ps

Table 3.1: *Offline Selection criteria applied to analyse $B^0 \to J/\psi K^{*0}$ decays.*

ciency loss of only roughly two per mille.

Four criteria are posed on the ***J/ψ* selection**. The J/ψ candidate is formed from two oppositely-charged muons whose invariant mass has to be in the range from 3030 to 3150 MeV. This criterion includes all signal events as can be seen from the mass distribution presented in the next section. The fit of the common vertex is required to be of a certain quality which is ensured by selecting only candidates with $\chi^2_{\text{vtx}}(J/\psi)/\text{nDoF} < 16$. Again, a similar value around 16 could be applied, the particular choice has been selected to meet the requirements of several $B \to J/\psi X$ decays. Only muons with a transverse momentum p_{T} larger than 500 MeV are chosen. This largely reduces the number of muons originating directly from the PV. And finally, the muons have to have a positive muon probability, $\Delta \ln \mathcal{L}_{\mu\pi} > 0$, to minimise misidentification.

Similar selection requirements apply to the $\boldsymbol{K^{*0}}$ **selection**. Candidates are built from an oppositely charged kaon-pion pair with invariant mass in the range from 826 to 966 MeV. The same criterion as for the J/ψ is posed on the quality of the vertex fit. An important cut is applied to the transverse momentum of the K^{*0} which has to be larger than 2 GeV. Several cut scenarios in the range from 1 to 3 GeV have been tested and the one with the most efficient background rejection has been chosen. The applied cut is a strong requirement but reduces the background fraction by a large amount as will be shown in the next section. Furthermore, particle identification criteria are applied. Both the pion and the kaon are required to have a negative and positive kaon probability, respectively. In addition, the kaon has to have a kaon probability with respect to the proton of larger than -2. The particle identification requirements on the kaon are rather weak, contrary to the criterion $\Delta \ln \mathcal{L}_{K\pi}(\pi) < 0$. It has been specifically chosen to reduce peaking background from candidates where at least one track has been misidentified while still retaining most of the signal decays.

For the $\boldsymbol{B^0}$ **selection** as well criteria on the invariant mass (in the range from 5150 to 5400 MeV) and the quality of the vertex fit ($\chi^2_{\text{vtx}}(B^0)/\text{nDoF} < 10$) are applied. The selected mass range is very wide to allow a detailed investigation of the background distributions. In addition, the invariant mass of the two muons is constrained to the known J/ψ mass [5]. Consequently, the resolution of the B^0 mass is improved. Contrary to the other sub-selections, not only a vertex fit is performed but also a kinematic fit of the entire decay tree (Decay Tree Fit, DTF [62]). The full decay tree is parametrised by means of the momentum of the particles, the position of the vertices and the decay lengths. Also, at each vertex the momentum conservation is taken into account and it is required that the B^0 candidate originates from the PV. The fit uses the momentum and the position of the tracks and their covariance matrix as input. This kinematic fit is also required to be of a certain quality, selecting only canidates with $\chi^2_{\text{DTF}}(B^0)/\text{nDoF} < 5$. The particular cut value has been optimised for several $B \to J/\psi X$ decays. Also, one can calculate the χ^2 of the IP by taking the IP significance, $\text{IP}/\sigma_{\text{IP}}$, to the second power. This quantity, χ^2_{IP}, is required to be smaller than 25 to ensure that the B^0 candidates originate from the PV. Usually, there is more than one PV in the event. To avoid misidentification of the PV, a minimum impact parameter to the second nearest PV is required, $\chi^2_{\text{IP,next}} > 50$. This is a loose criterion but is helpful to prevent assignments to the wrong PV. A hard constraint is put on the decay time of the B^0 candidates, which has to be larger than 0.3 ps. This criterion largely reduces the prompt background without removing a large fraction of signal candidates. The decay time is restricted to 14 ps at maximum, which neglects only a few candidates. Finally, in cases with more than one B^0 candidate per event the one with the best DTF quality is chosen. It is verified that the average number of B^0 candidates per events in the signal region is small (1.03) and that the best candidate selection does not introduce any bias on the observables.

3.4 Selection efficiencies and mass plots

An approximate overview of the selection efficiencies is given in Table 3.2. All numbers have been obtained from data. The first row indicates which cuts have been applied in addition to the previous line, the cut efficiency shows which fraction of candidates passes the selection compared to the previous set of cuts. The number of signal candidates (for the signal over background ratio) are determined by a fit to the B^0 mass distribution. A statistical error is only assumed for the signal fraction which can then be propagated to the number of signal candidates. The fit is described in more detail in Ch. 4. The pre-selection consists only of a few basic particle identification (PID) and kinematic requirements and the decay time cut is set to 0.2 ps. Also, the trigger lines as discussed in Sec. 3.3 are applied. The stricter decay time cut of the offline selection increases the signal fraction by more than 50%. The standard $B \to J/\psi X$ selection (see [58, 59, 60]) requires a weaker constraint on $p_{\mathrm{T}}(K^{*0})$ (larger than 1 GeV) and does not apply the pion PID cut but else is identical to the selection listed in Table 3.1. Applying the first of these additional cuts approximately doubles the signal fraction and the tight PID criterion increases the signal over background ration by almost 70%. This PID requirement on the pion has been specifically chosen to reduce most of the peaking background components (see Ch. 5).
In total, $77\,282$ $B^0 \to J/\psi K^{*0}$ candidates are selected in data after applying all selection criteria. Using the same requirements for the simulated sample, $404\,624$ candidates remain.
To visualise the effect of the cuts listed in Table 3.2 and the low background fraction after the full selection, the B^0 mass distributions at various stages of the selection are shown in Fig. 3.1. The blue and the red curves show the signal and background distributions, respectively, the sum of both is shown in black. In Fig. 3.1(a) only the

Criterion	Candidates	ϵ_{cut}	S/B	f_{sig}
Pre-selection and trigger	900 920	–	0.161	0.139
Decay time cut	533 935	0.593	0.300	0.231
Standard $B \to J/\psi X$ selection	299 011	0.647	0.577	0.366
$p_{\mathrm{T}}(K^{*0})$ cut	109 254	0.365	2.268	0.694
$\Delta \ln \mathcal{L}_{\pi K}(\pi)$ cut	77 282	0.707	3.808	0.792

Table 3.2: *Selection efficiency table showing the number of B^0 candidates, the cut efficiency on all candidates passing the additional criterion, the signal over background ratio and the signal fraction. All numbers are obtained from data. The statistical error of the signal fraction is approximately 0.002.*

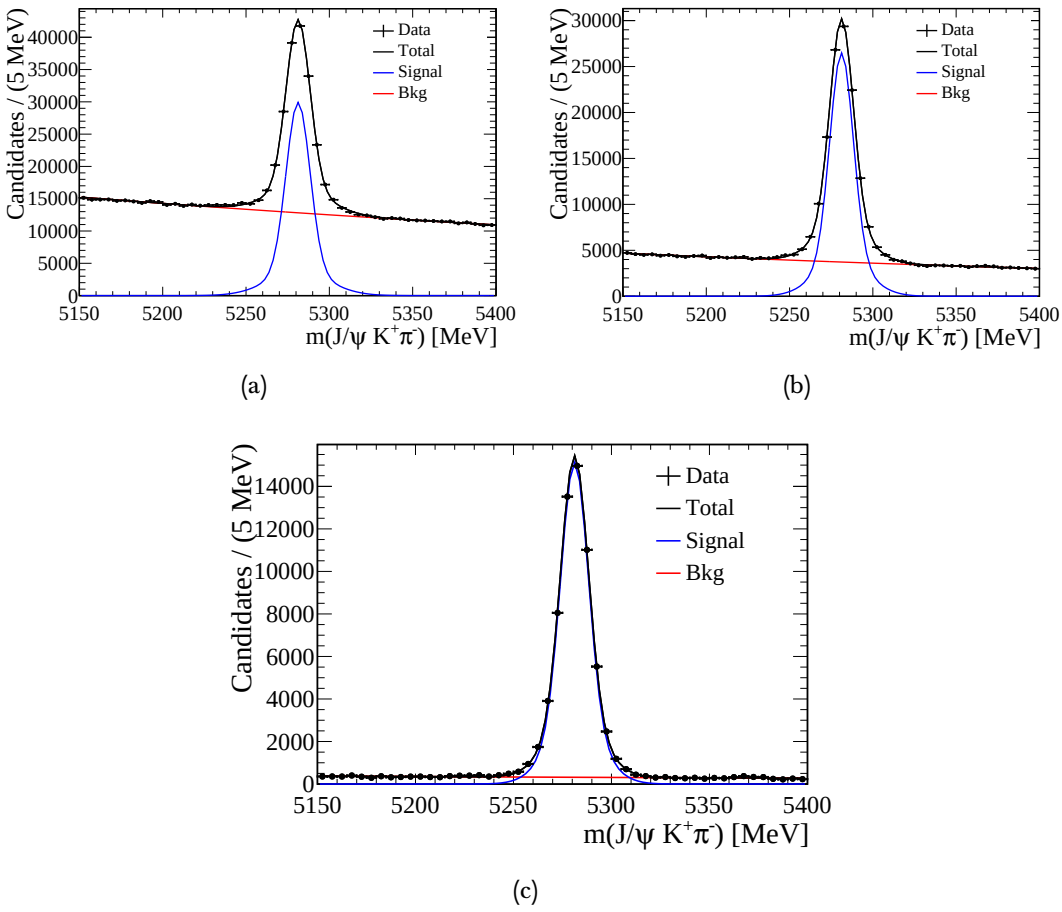

Figure 3.1: *Invariant mass distributions of selected $B^0 \to J/\psi K^{*0}$ candidates where (a) only the pre-selection and the trigger strategy, (b) the standard $B \to J/\psi X$ selection and (c) the full selection has been applied. All three plots show the signal (blue), background (red) and total (black) distribution.*

pre-selection and the trigger has been applied, Fig. 3.1(b) shows the mass distribution after the standard $B \to J/\psi X$ selection and in Fig. 3.1(c) all cuts are in effect. For the latter scenario the signal fraction in a narrow mass window of ± 30 MeV around the known B^0 mass [5] is approximately 93%, indicating a very clean signal. The signal distributions in all three figures is described by the sum of two Gaussian functions $\mathcal{G}_1$ and $\mathcal{G}_2$ with common mean mass m_{B^0}

$$\mathcal{G}_D = f^{\sigma}_{\mathrm{m},1} \cdot \mathcal{G}_1(m_{B^0}, \sigma^{sig}_{\mathrm{m},1}) + (1 - f^{\sigma}_{\mathrm{m},1}) \cdot \mathcal{G}_2(m_{B^0}, \sigma^{sig}_{\mathrm{m},2}), \tag{3.1}$$

where $f^{\sigma}_{\mathrm{m},1}$ is the fraction of the first Gaussian function and $\sigma^{sig}_{\mathrm{m},1}$ and $\sigma^{sig}_{\mathrm{m},2}$ are the widths of the first and second Gaussian function, respectively. As the effect of the detector resolution is larger than the natural decay width, the distribution cannot be

Parameter	Fit result
m_{B^0}	5281.19 ± 0.04 MeV
$f^{\sigma}_{\mathrm{m},1}$	0.714 ± 0.025
$\sigma^{sig}_{\mathrm{m},1}$	6.99 ± 0.11 MeV
$\sigma^{sig}_{\mathrm{m},2}$	13.38 ± 0.43 MeV
α_{m}	-0.0012 ± 0.0001

Table 3.3: *Fit values of the parameters of the fit to the B^0 invariant mass distribution after applying all selection criteria. The errors are statistical only.*

described by a Breit-Wigner function. Usually, a Gaussian function is used, in this case, however, the data is better described by the sum of two Gaussian functions. This improves the description of the tails of the distribution. The background is modelled by an exponential function with constant α_m, $e^{\alpha_m \cdot m}$. A more detailed investigation of the background is given in Ch. 5. All parameters determined by the fit to the mass distribution after the full selection can be found in Table 3.3. From the fit, the number of signal events is found to be $61\,244 \pm 132$. The effective mass resolution is determined to be

$$\sigma_{\mathrm{eff}} = \sqrt{f^{\sigma}_{\mathrm{m},1} \cdot {\sigma^{sig}_{\mathrm{m},1}}^2 + (1 - f^{\sigma}_{\mathrm{m},1}) \cdot {\sigma^{sig}_{\mathrm{m},2}}^2} = (9.3 \pm 0.8)\ \mathrm{MeV}. \tag{3.2}$$

In Fig. 3.2 the distributions of the $\mu^+\mu^-$ and $K^+\pi^-$ invariant mass are shown. In both cases the background is subtracted using the so-called sPlot technique which is explained in detail in [63], making use of the fit to the $J/\psi K^+\pi^-$ mass distribution

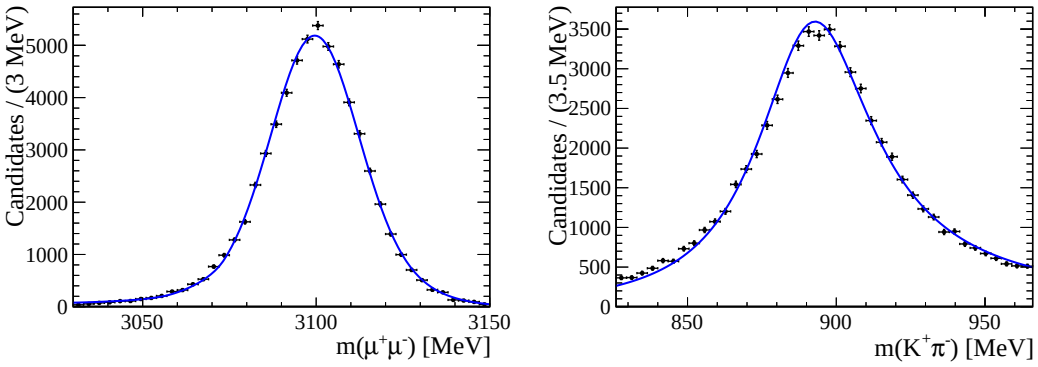

Figure 3.2: *Background subtracted invariant $\mu^+\mu^-$ (left) and $K^+\pi^-$ (right) mass distributions.*

as discriminating variable. Each event is given a signal weight, W_i, which is then used to separate signal and background (see also Ch. 4). In practise, the weights are calculated by using the relative fractions of the fitted signal and background distributions as a function of $m(J/\psi K^+\pi^-)$. Candidates that are more likely to be a signal event are assigned a larger weight, whereas probable background events have a corresponding weight that is small or negative. This strategy statistically separates background from signal.
The $\mu^+\mu^-$ invariant mass cannot be modelled by a simple sum of two Gaussian functions as the radiative tail is quite pronounced. Instead, a so-called Crystal Ball function is used [64]. The basic Crystal Ball function consists of a Gaussian core and a radiative tail towards low masses described by a polynomial. The functional form can be written as

$$\mathcal{CB}(m;\alpha,n,\mu,\sigma) = N\cdot\begin{cases} e^{-\frac{(m-\mu)^2}{2\sigma^2}} & \text{for } \frac{m-\mu}{\sigma} > -\alpha \\ \left(\frac{n}{|\alpha|}\right)^n e^{-\frac{|\alpha|^2}{2}} \left(\frac{n}{|\alpha|} - |\alpha| - \frac{m-\mu}{\sigma}\right)^{-n} & \text{for } \frac{m-\mu}{\sigma} \leq -\alpha \end{cases} \tag{3.3}$$

where m is the invariant mass, μ and σ are the mean and the width of the mass distribution, α and n are the starting point and the order of the polynomial function and N is a normalisation factor. In this analysis the Gaussian core is replaced by the sum of two Gaussian functions to better describe the data.
As already discussed in Ch. 1, the $m(K^+\pi^-)$ invariant mass distribution can be described by a Breit-Wigner function following the formula given in Eq. 1.25. This is the case as the natural decay width is larger than the detector resolution. However, the data are still not well-described using this parametrisation, as seen in Fig. 3.2(b). Several other fit models have been used (e.g. the sum of two Gaussian functions) but a better agreement has not been found. One reason could be that the sPlot method does not fully separate signal and background for the $K^+\pi^-$ invariant mass distribution. This does not affect the measurement of the polarisation amplitudes as $m(K^+\pi^-)$ is not explicitly taken into account in the decay rate.

3.5 Angular acceptance

Due to the finite detector acceptances and the trigger and selection criteria the angular distributions are distorted. These effects can be described by the angular acceptance which is defined as

$$\epsilon(\Omega) = \frac{\text{number of selected } B^0 \text{ candidates } (\Omega)}{\text{number of expected } B^0 \text{ candidates } (\Omega)}, \tag{3.4}$$

where Ω denotes the three transversity angles. From the description of the angles in Subsec. 1.4.2 one can conclude that they are highly correlated. Therefore, a three-dimensional description of the acceptance has to be used. Since the main goal of this analysis is to measure the polarisation amplitudes which determine the shape of

the angular distributions, the acceptance has to be obtained from simulated events. As geometric cuts have already been applied in the generation of the $B^0 \to J/\psi K^{*0}$ simulated sample, the theoretical prediction is used in the denominator instead of the expected number of events, so that

$$\epsilon(\Omega) = \frac{\text{number of selected } B^0 \text{ candidates } (\Omega)}{N \int \mathrm{d}t \int \mathrm{d}\Omega \, \mathcal{S}(\Omega|t, \vec{\lambda})}, \tag{3.5}$$

where $\mathcal{S}(\Omega|t, \vec{\lambda}) = \frac{1}{2}\frac{\mathrm{d}^4\Gamma(B^0 \to J/\psi K^{*0})}{\mathrm{d}t\,\mathrm{d}\Omega} + \frac{1}{2}\frac{\mathrm{d}^4\Gamma(\overline{B}^0 \to J/\psi \overline{K}^{*0})}{\mathrm{d}t\,\mathrm{d}\Omega}$ is the differential decay rate conditional on the decay time t and the physical and detector parameters λ, and N is the selected number of events.

The one-dimensional projections of the acceptance integrated over the two other angles are shown in Fig. 3.3. The projections are normalised such that the average value over the range of the histogram is unity. The shape of the acceptance distributions can be mainly attributed to the detector geometry cuts (between 0 and 400 mrad around the beam pipe) and to the hard requirements on the transverse

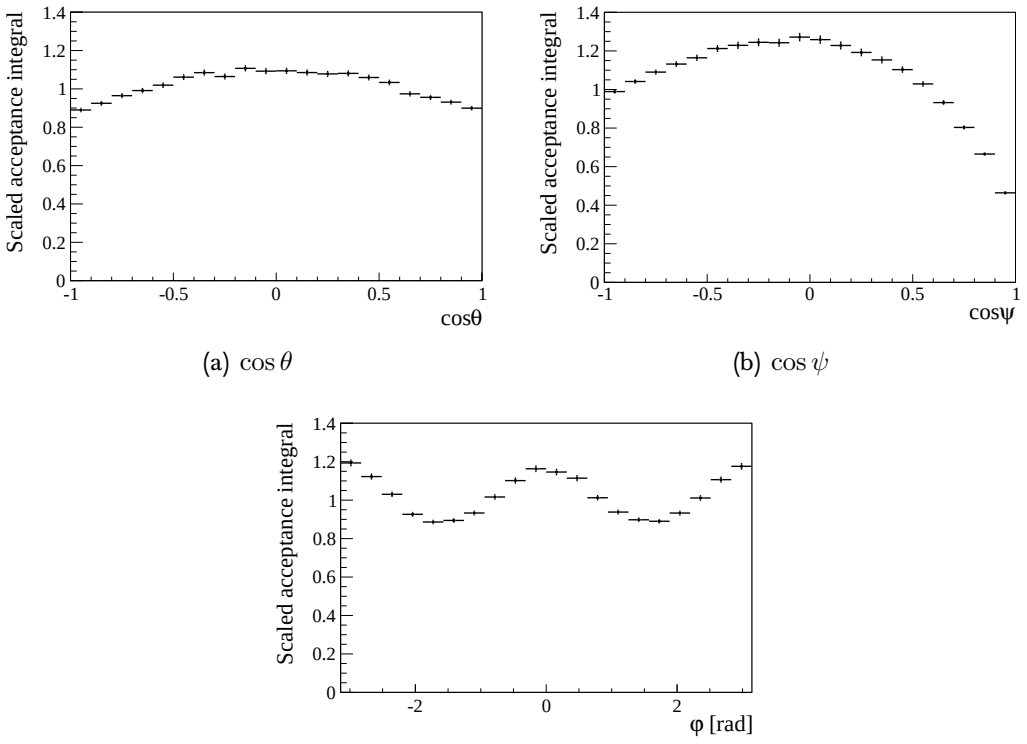

(a) $\cos\theta$ (b) $\cos\psi$

(c) φ

Figure 3.3: *Angular acceptance $\epsilon(\Omega)$ as a function of each decay angle. The projections are normalised such that the average value over the range of the histogram is unity.*

momentum of the K^{*0} and the PID requirement on the pion which are responsible for the asymmetric shape of the $\cos\psi$ distribution. The issue of angular acceptance in general is addressed in [65]. It should be, however, emphasised again that the determination of the angular acceptance entirely relies on simulated events. As the true angular distributions are not known, there is no possibility to determine the acceptances on data. Using simulated events for the acceptances is one of the most important issues of this analysis since it is not clear a priori how well the data is described by the simulation. It is therefore essential that the kinematic distributions between data and simulation agree to ensure the validity of the acceptance description. Any deviation has to be treated as a systematic uncertainty to the observables. This is discussed in more detail in Ch. 6.
In the next chapter it will be explained that the polarisation amplitudes and phases are extracted using a maximum likelihood fit. The angular part of the probability density function contains the angular acceptance in both the numerator and the denominator (normalisation). If the reader would like to have a look in advance, this can be seen in Eq. 4.13. As the logarithmic likelihood function is used in the fit, the angular acceptance, $\epsilon(\Omega)$, is only important in the normalisation but not in the numerator. There, it is a mere constant in the sum of logarithmic likelihoods (this is fully correct only if the background is subtracted before the likelihood fit). Thus, instead of using a three-dimensional acceptance histogram in numerator and denominator, one can re-write the normalisation and introduce ten normalisation factors [66]

$$\xi_k = \int \mathrm{d}\Omega \; f_k(\Omega) \cdot \epsilon(\Omega), \tag{3.6}$$

where $f_k(\Omega)$ are the angular functions defined in Table 1.3. This simplifies the comparison of different sets of acceptances. The exact implementation of the angular acceptance in the fitting algorithm is explained in detail in Subsec. 4.3.1.

3.6 Decay time acceptance

As shown in Ch. 1, the decay time and the angular part of the decay rate separate. Therefore, it is expected that the angular observables do not depend on the correct description of the decay time acceptance. Also, this analysis is not intended to perform a lifetime measurement but uses it merely as an additional discriminating parameter between signal and background in the classical fit technique as described in Sec. 4.2. Nonetheless, the decay time acceptance effects are discussed here in more detail.
Similarly as for the angular acceptance, the decay time acceptance can be determined by (t is the decay time)

$$\epsilon(t) = \frac{\text{number of selected } B^0 \text{ candidates } (t)}{\text{number of expected } B^0 \text{ candidates } (t)}, \tag{3.7}$$

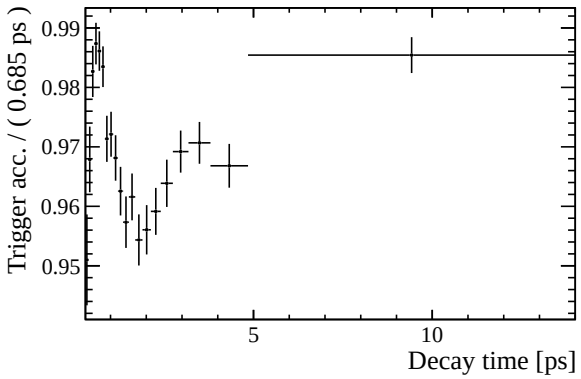

Figure 3.4: *Acceptance distribution for low decay times. Note the zero suppression of the y-axis. Figure from [67].*

using simulated events. However, for lifetime measurements using simulated events only is not sufficient. Instead the acceptance has to be partially determined from data. An extensive review of the issue can be found in [68]. Here, the two main effects are briefly summarised. At large decay times the reconstruction efficiency in the VELO detector decreases. This effect can be parametrised by the efficiency function

$$\epsilon_{\text{high}}(t) = 1 + \beta t, \tag{3.8}$$

with $\beta = (-0.0092 \pm 0.0008)$ ps^{-1}. The factor used specifically for this analysis is taken from a preliminary study of the β-factor using simulated events and data [67]. At small decay times the acceptance is dominated by the HLT2DiMuonDetachedJpsi trigger line which introduces a bias on the decay time. To account for this a one-dimensional histogram is used. The acceptance distribution for this trigger line, which can be seen in Fig. 3.4, is determined in the following way: As a reference the trigger line HLT2DiMuonJpsi is used which requires the same selection cuts as the HLT2DiMuonDetachedJpsi line except for the requirement on the DL significance of the J/ψ meson, i.e. it does not introduce a decay time bias. The efficiency is then calculated from the events passing the combination of trigger lines

$$\epsilon_{\text{low}}(t) = \frac{\text{HLT2DiMuonDetachedJpsi AND HLT2DiMuonJpsi}}{\text{HLT2DiMuonJpsi}}. \tag{3.9}$$

This procedure is performed entirely on data thus avoiding to rely on simulated events. It can be seen that there is an efficiency drop at around 2 ps. This can be explained by technical issues in the determination of the primary vertex. It has no physics reason but is merely an artefact. In principle, it would be expected that the acceptance rises monotonously for small decay times. The acceptance remains flat for decay times larger than 6 ps.

It should be noted again that the decay time and related acceptance effects have only a negligible impact on the extracted polarisation amplitudes and phases as the angular and time dependent parts of the decay rate factorise [28]. The decay time is only used to better discriminate between signal and background. In Ch. 9 it will be explicitly shown that the correlation between the decay time and the polarisation amplitudes is negligible.

Chapter 4

Extracting the physics parameters

That's how we know we're alive: we're wrong.
*Philip Roth (*1932), in "American Pastoral"*

The physical observables are obtained using a maximum likelihood fit. This chapter explains the general concept of this method and details the signal and background distributions describing the data. The chapter ends with an extensive validation of the fitting procedure and a summary of the nominal fit results.

4.1 Maximum Likelihood Method

The physical observables are extracted using a four-dimensional maximum likelihood fit to the decay time and the three transversity angles (for the following see [69]).
With the maximum likelihood method, one or more unknown parameters $\vec{\lambda}$ (physical observables, background and detector parameters) can be estimated from a measured data set, $\vec{x}$. Usually, the data set is composed of a large number of events, N. In this analysis the event data, $\vec{x}_i$ ($i = 1, ..., N$), consist of the four measured quantities decay time and transversity angles. The theoretical prediction for the distribution of the measured data set is the so-called Probability Density Function (PDF), $f(\vec{x}|\vec{\lambda})$. The PDF depends on the unknown parameters $\vec{\lambda}$ and has to obey the normalisation condition

$$\int_D f(\vec{x}|\vec{\lambda})\mathrm{d}\vec{x} = 1 \tag{4.1}$$

as the probability to measure any possible value is 1. D is the domain of $\vec{x}$. The PDF then determines the probability of a measurement in the range $[\vec{x}, \vec{x} + \mathrm{d}\vec{x}]$, conditional on $\vec{\lambda}$. In the maximum likelihood method, the likelihood function is formed from the given PDF and is defined as the product of the PDFs for all N events, i.e.

$$\vec{\mathcal{L}}(\vec{\lambda}) = f(\vec{x}_1|\vec{\lambda}) \cdot f(\vec{x}_2|\vec{\lambda}) \cdots f(\vec{x}_N|\vec{\lambda}) = \prod_{i=1}^{N} f(\vec{x}_i|\vec{\lambda}). \tag{4.2}$$

The function $\mathcal{L}(\vec{\lambda})$ gives the likelihood to obtain the measured quantities for a given choice of parameters $\vec{\lambda}$. The best estimate $\hat{\vec{\lambda}}$ for the unknown parameters maximises the likelihood function $\mathcal{L}(\vec{\lambda})$. It is very important to maintain the normalisation of $f(\vec{x}|\vec{\lambda})$ at all times. In practice, the negative logarithm of the likelihood function is used so that the function

$$F(\vec{\lambda}) = -\ln \mathcal{L}(\vec{\lambda}) = -\sum_{i=1}^{N} \ln f(\vec{x}_i|\vec{\lambda}) \tag{4.3}$$

is minimised. This procedure is numerically more stable.
In this analysis the minimisation is performed using the Minuit framework [70]. The analysis presented here is based on a fitting algorithm developed for the analysis of $B_s^0 \to J/\psi\phi$ decays, documented in [46].
For a large number of events ($N \to \infty$) the probability distribution of the parameters determined in the fit is Gaussian. In this case and for a single parameter λ the error of this parameter is determined by [69]

$$\sigma = \left(\frac{\mathrm{d}^2 F}{\mathrm{d}\lambda^2}\bigg|_{\hat{\lambda}} \right)^{-1/2}. \tag{4.4}$$

The negative logarithmic likelihood function has the form of a parabola and its value around the minimum is

$$F(\hat{\lambda} \pm r \cdot \sigma) = F(\hat{\lambda}) + \frac{1}{2} r^2. \tag{4.5}$$

In the case of more than one parameter the errors and their correlations are described by a matrix $\boldsymbol{G}$ whose elements can be calculated by

$$G_{ik} = \frac{\partial^2 F}{\partial\lambda_i \partial\lambda_k}, \tag{4.6}$$

where ∂ denotes a partial derivative.
Often, the so-called likelihood ratio method is used to determine confidence intervals. For one single parameter it is determined at fixed values λ_i of this parameter by the difference of the logarithmic likelihood

$$-2 \cdot \Delta \ln \mathcal{L}(\lambda_i) = -2 \cdot [\ln \mathcal{L}(\hat{\lambda}_i) - \ln \mathcal{L}(\lambda_i)], \tag{4.7}$$

where $\hat{\lambda}_i$ is the best estimate of the parameter. The best estimate is determined from a full fit to data. A so-called profile likelihood distribution is then obtained by calculating the likelihood ratio for a set of values around the best estimate (grid points). The $1\sigma(, 2\sigma, 3\sigma)$ confidence levels are defined at those values where $-2 \cdot \Delta \ln \mathcal{L} = 1(, 4, 9)$. As in this analysis there are multiple parameters, the likelihood ratio depends on additional parameters $\vec{\lambda}$. The ratio $-2 \cdot \Delta \ln \mathcal{L}(\lambda_i, \vec{\lambda})$ is then determined at grid points of λ_i by minimising the likelihood function with respect to all other parameters, i.e. fixing the parameter under investigation to the grid point. Examples of profile likelihoods are shown in Sec. 9.3.

4.2 Parameters and fitting technique

The maximum likelihood method introduced in the previous section is used to extract the physical observables, $\vec{\lambda}_{\rm phys}$. In addition, several so-called nuisance parameters are needed to describe the data. They can be separated in detector parameters, $\vec{\lambda}_{\rm det}$, that mainly model the imperfect detector resolution, and background parameters, $\vec{\lambda}_{\rm bkg}$, describing the distribution of the different background components. All of these parameters $\vec{\lambda}$ are explained in more detail in the following section where the probability density functions for the signal and background part are discussed. This section is intended to detail the parametrisation of the physics parameters in the fit and to explain the standard (or classical) fitting approach that is used in this analysis. An alternative technique is presented in Subsec. 4.3.3.
In Subsec. 1.4.2 it has been shown that the P- and S-wave components can be described by four amplitudes and the corresponding phases. The amplitudes obey the normalisation condition $|A_0|^2 + |A_\parallel|^2 + |A_\perp|^2 + |A_{\rm S}|^2 = 1$, from which the amplitude $|A_0|^2$ can be inferred. Note that δ_0 is set to zero by convention. In the fit the amplitudes are parametrised such that the P-wave amplitudes are normalised to the total P-wave fraction. One can then define the P-wave ratios

$$R_\parallel = \frac{|A_\parallel|^2}{|A_{\rm P}|^2}, \quad R_\perp = \frac{|A_\perp|^2}{|A_{\rm P}|^2}, \quad R_0 = \frac{|A_0|^2}{|A_{\rm P}|^2}, \tag{4.8}$$

where $|A_{\rm P}|^2 = |A_0|^2 + |A_\parallel|^2 + |A_\perp|^2$ and $R_\parallel + R_\perp + R_0 = 1$, and the S-wave fraction

$$F_{\rm S} = \frac{|A_{\rm S}|^2}{|A_{\rm P}|^2 + |A_{\rm S}|^2}. \tag{4.9}$$

As $|A_{\rm P}|^2 + |A_{\rm S}|^2 = 1$, the relation $F_{\rm S} = |A_{\rm S}|^2$ holds. So, the physics parameters consist of three amplitude fractions and three phases, $\vec{\lambda}_{\rm phys} = \{R_\parallel, R_\perp, F_{\rm S}, \delta_\parallel, \delta_\perp, \delta_{\rm S}\}$. In addition, the decay width Γ_d is a parameter of the fit and used for additional background separation.
The full fit is performed in four bins of the $K^+\pi^-$ invariant mass. In this chapter, the parameters of the fit are first introduced for a single mass bin. It is then explained how the fit in multiple bins is performed.

In the so-called **classical fit (cFit)** both the signal part and the background part of the PDF are explicitly modelled, i.e. the full PDF as described in the next section is minimised using the maximum likelihood method. In addition to the measured quantities, decay time and transversity angles, the B^0 mass is fitted simultaneously to separate the background.
The following section is dedicated to the presentation of the PDF. Both the parametrisation of the signal and the background component is shown.

4.3 The probability density function

Generally, the PDF can be separated in a signal part $\mathcal{S}(\vec{x}|\vec{\lambda})$ and a background part $\mathcal{B}(\vec{x}|\vec{\lambda})$ such that

$$f(\vec{x}|\vec{\lambda}) = f_{\rm sig} \cdot \mathcal{S}(\vec{x}|\vec{\lambda}) + (1 - f_{\rm sig}) \cdot \mathcal{B}(\vec{x}|\vec{\lambda}), \tag{4.10}$$

where $f_{\rm sig}$ is the signal fraction. Both components depend on the measured quantities decay time, the transversity angles and the B^0 mass. The latter is especially used to separate signal from background.

4.3.1 The signal component

There is no reason to assume that the invariant mass of the B^0 meson is correlated to the transversity angles and the decay time. In particular, the decay rate is independent of $m(B^0)$. Thus, the mass dependent part of the PDF can be factorised from the time and angular components. The signal part, which contains the physics parameters, can be written in the following form (m denotes the measured B^0 mass)

$$\mathcal{S}(\vec{x}|\vec{\lambda}) = \mathcal{S}_m(m|\vec{\lambda}_{\rm det}) \cdot \mathcal{S}_{t,\Omega}(t,\Omega|\vec{\lambda}_{\rm phys}), \tag{4.11}$$

neglecting detector effects like the decay time resolution and acceptance which will be discussed later in this section.

The **mass distribution** of the B^0 meson is best described by the sum of two Gaussian functions as the detector resolution is much larger than the actual width of the resonance. Two instead of one Gaussian function are used to better describe the data, especially the tails of the distribution, see also Sec. 3.4. The mass PDF $\mathcal{S}_m(m|\vec{\lambda}_{\rm det})$ has the same form as in Eq. 3.1. A fit to the mass distribution only gives the results listed in Table 3.3. In summary, the parameters describing the mass PDF consist of $\vec{\lambda}_{\rm det} = \{m_{B^0}, f^{\sigma}_{\rm m,1}, \sigma^{sig}_{\rm m,1}, \sigma^{sig}_{\rm m,2}\}$, where $f^{\sigma}_{\rm m,1}$ is the fraction of the first Gaussian function and $\sigma^{sig}_{\rm m,1}, \sigma^{sig}_{\rm m,2}$ are the widths of the first and second Gaussian function, respectively. In the full cFit to data these mass parameters are obtained simultaneously with the angular observables.

The physics parameters, which are the observables of interest, appear in the **time and angular dependent part** of the PDF. Following Eq. 1.22, the PDF has the form

$$\mathcal{S}_{t,\Omega}(t,\Omega|\vec{\lambda}_{\rm phys}) = \frac{1}{2}\frac{{\rm d}^4\Gamma(B^0 \to J/\psi K^{*0})}{{\rm d}t\,{\rm d}\Omega} + \frac{1}{2}\frac{{\rm d}^4\Gamma(\overline{B}^0 \to J/\psi \overline{K}^{*0})}{{\rm d}t\,{\rm d}\Omega}. \tag{4.12}$$

It is conditional on the physics parameters which are varied in the fit. In addition, the decay width, Γ_d, is a free parameter in the fit but is not quoted as a physics result since this analysis is not intended to measure the lifetime of the B^0 meson. The fit

gives a value of $\Gamma_d = (0.664 \pm 0.003)$ ps (statistical error only), in good agreement with the known value [5]. To see the effect of having Γ_d as additional free parameter in the cFit another fit is performed with a fixed value of the decay width. The signal fraction is slightly higher (order 1%) in the default case resulting in a better signal-background separation. A full explanation for this observation has not been found. One reason can be that the decay time distributions are different for signal and background and that by explicitly fitting for Γ_d both components can be better separated.

In addition to the simple form of Eq. 4.12, **detector resolution and acceptance effects** have to be taken into account when describing the data.
Due to the finite decay time resolution of the detector, the time-dependent term, $e^{-\Gamma_d t}$, in Eq. 1.22 has to be modified by a resolution function. This is done by convolving the exponential term with a triple Gaussian resolution function $\mathcal{G}(t, \sigma_t)$. Here, σ_t is the effective width that is defined analogously to Eq. 3.2 as $\sigma_t = \sqrt{f_1 \cdot \sigma_1^2 + f_2 \cdot \sigma_2^2 + (1 - f_1 - f_2) \cdot \sigma_3^2}$, where f_i and σ_i ($i = 1, 2, 3$) are the fractions and the widths of the three single Gaussian functions, respectively. Varying the width between 30 and 100 fs (the expected decay time resolution is at around 50 fs) and neglecting the resolution entirely has no measurable effect on the physics parameters.
In principle, angular resolution effects have to be considered as well in the fitting procedure. In [71] they have been estimated to be approximately 30 mrad using simulated events (as for the decay time resolution a triple Gaussian has been used). Pseudo-experiments have shown that the effect on the physics observables is negligible. The study in [71] is done for $B_s^0 \to J/\psi\phi$ decays but since the kinematic model is the same for the process investigated here, angular resolutions are expected to be of the same order and thus, are neglected here.
In Sec. 3.5 it has been explained that detector acceptance effects have to be taken into account. This yields a modified time and angular part of the PDF

$$\mathcal{S}'_{t,\Omega}(t, \Omega|\vec{\lambda}_{\text{phys}}, \vec{\lambda}_{\text{det}}) = \frac{\epsilon(t) \cdot \epsilon(\Omega) \cdot \mathcal{S}_{t,\Omega}(t, \Omega|\vec{\lambda}_{\text{phys}}) \otimes \mathcal{G}(t, \sigma_t)}{\int \mathrm{d}t\mathrm{d}\Omega \ \left[\epsilon(t) \cdot \epsilon(\Omega) \cdot \mathcal{S}_{t,\Omega}(t, \Omega|\vec{\lambda}_{\text{phys}}) \otimes \mathcal{G}(t, \sigma_t)\right]}, \quad (4.13)$$

where $\epsilon(t)$ and $\epsilon(\Omega)$ are the time and angular acceptance functions, respectively. As the time and angular parts of the decay rate separate, it is expected that the time and angular dependent acceptances factorise as well. Note that the acceptance appears in both the numerator and the denominator (normalisation) of Eq. 4.13.
There are two effects accounting for the decay time acceptance. The lower decay time acceptance is determined from a histogram of 20 bins (see Fig. 3.4) which is used explicitly in the PDF. The upper decay time correction, $\epsilon_{\text{high}}(t) = 1 + \beta t$, is also taken into account.
The angular acceptance is described by a three-dimensional histogram of 20 bins for each angular variable. The one-dimensional projections are shown in Fig. 3.3. Similarly to the decay time acceptance, the histogram is used in the numerator and

Factor	Nominal acceptance	Flat acceptance
ξ_1	0.8985 ± 0.0017	1
ξ_2	1.1727 ± 0.0024	1
ξ_3	1.1788 ± 0.0025	1
ξ_4	0.0002 ± 0.0017	0
ξ_5	-0.0112 ± 0.0011	0
ξ_6	-0.0008 ± 0.0010	0
ξ_7	1.0290 ± 0.0019	1
ξ_8	-0.0113 ± 0.0016	0
ξ_9	0.0017 ± 0.0015	0
ξ_{10}	-0.2292 ± 0.0029	0

Table 4.1: *Nominal acceptance factors and numbers for a flat acceptance indicating the statistical error only.*

the denominator of the signal PDF.
The normalisation in the denominator of Eq. 4.13 can be re-written in the following way using the definition of the factors h_k

$$\int \mathrm{d}t\mathrm{d}\Omega\ \epsilon(t)\cdot\epsilon(\Omega)\cdot\mathcal{S}_{t,\Omega} = \sum_{k=1}^{10}\xi_k\cdot\int \mathrm{d}t\ e^{-\Gamma_d t}\cdot h_k\cdot\epsilon(t), \tag{4.14}$$

where ξ_k are the normalisation factors as defined in Eq. 3.6. These factors can be determined directly from the acceptance histogram. The factors corresponding to the acceptance used in the default fit and describing a flat acceptance are shown in Table 4.1. The parameters describing the resolution effects as detailed in this section are not varied in the fit.

4.3.2 The background component

Similarly to the signal component, no correlation is expected between the mass and the time and angular dependent part. Thus, one can write

$$\mathcal{B}(\vec{x}|\vec{\lambda}) = \mathcal{B}_m(m|\vec{\lambda}_{\mathrm{bkg}})\cdot\mathcal{B}_{t,\Omega}(t,\Omega|\vec{\lambda}_{\mathrm{bkg}}). \tag{4.15}$$

In the signal PDF, the time and the angular part factorise. There is no evidence that this is not also valid for the background description. This allows to re-write the background PDF in the following way

$$\mathcal{B}(\vec{x}|\vec{\lambda}) = \mathcal{B}_m(m|\vec{\lambda}_{\mathrm{bkg}})\cdot\mathcal{B}_t(t|\vec{\lambda}_{\mathrm{bkg}})\cdot\mathcal{B}_\Omega(\Omega). \tag{4.16}$$

The angular part of the background does not explicitly depend on any parameters $\vec{\lambda}$ as it is determined from events with B^0 mass outside the region of the signal peak

Parameter	Fit result
$f_{\tau,1}^{\mathrm{LL}}$	0.546 ± 0.012
τ_1^{LL}	0.167 ± 0.005 ps
τ_2^{LL}	1.013 ± 0.022 ps

Table 4.2: *Parameter values from the fit to the time dependent background PDF (statistical errors only).*

(so-called sidebands) and kept constant.

The **background mass distribution** is best described by an exponential function, $e^{-\alpha_{\mathrm{m}}}$, normalised over the entire range of the mass fit. The corresponding parameter of the exponential, α_{m}, has already been introduced in Sec. 3.4.

The **background time distribution** can be best described by the sum of two exponential functions with different lifetimes

$$\mathcal{B}_t(t|\lambda_{\mathrm{bkg}}) = \frac{1}{N}\left(f_{\tau,1}^{\mathrm{LL}} \cdot e^{-t/\tau_1^{\mathrm{LL}}} + (1 - f_{\tau,1}^{\mathrm{LL}}) \cdot e^{-t/\tau_2^{\mathrm{LL}}}\right), \tag{4.17}$$

where N is the normalisation obtained by integrating over the entire decay time range, $f_{\tau,1}^{\mathrm{LL}}$ is the fraction of the first exponential and τ_1^{LL} and τ_2^{LL} are the lifetimes of the first and second exponential, respectively. This parametrisation does not correspond to a physical model but is rather motivated by the observed shape in data. The index LL indicates that both components seem to be long-lived compared to prompt events that are mostly rejected due to the cut on the decay time of the B^0 meson of 0.3 ps. The results for these background parameters from a fit to data can be found in Table 4.2. It can be seen that roughly the same number of background events are described by each of the two components ($f_{\tau,1}^{\mathrm{LL}} \approx 0.55$). The first has a low average lifetime of 0.2 ps. This background component most likely originates from the tail of prompt events with relatively large measured lifetimes. The second contribution has a much larger average lifetime of around 1.0 ps, originating from other B-background.

In summary, the background parameters are $\vec{\lambda}_{\mathrm{bkg}} = \{\alpha_{\mathrm{m}}; f_{\tau,1}^{\mathrm{LL}}, \tau_1^{\mathrm{LL}}, \tau_2^{\mathrm{LL}}\}$. They are all left free in the full maximum likelihood fit.

The **angular background distributions** are described by a three-dimensional histogram using 10 bins in each angular variable. The three dimensions of the histogram ensure that possible correlations between the angles are taken into account. For the background description only events from the B^0 mass sidebands are used, i.e. the invariant mass is required to be in the range from 5150 to 5230 MeV or from

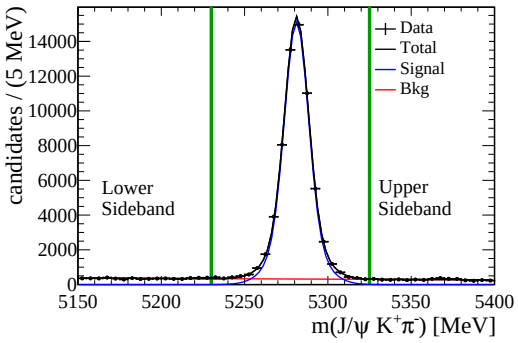

Figure 4.1: *Invariant B^0 mass distribution indicating the upper and lower sideband used to determine the time and angular background distributions.*

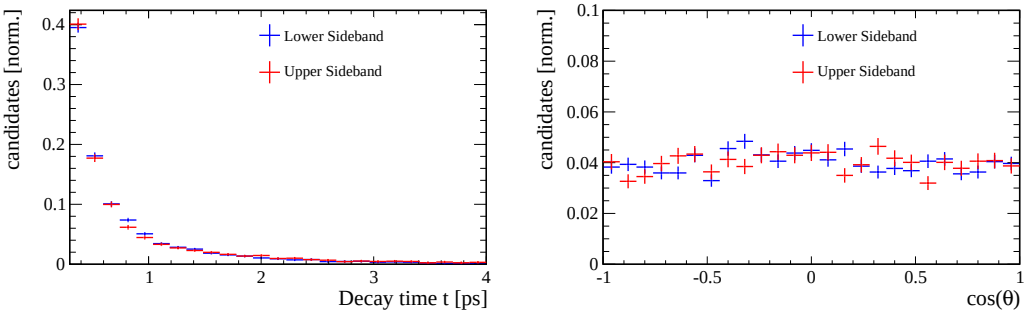

(a) Decay time t (b) $\cos\theta$

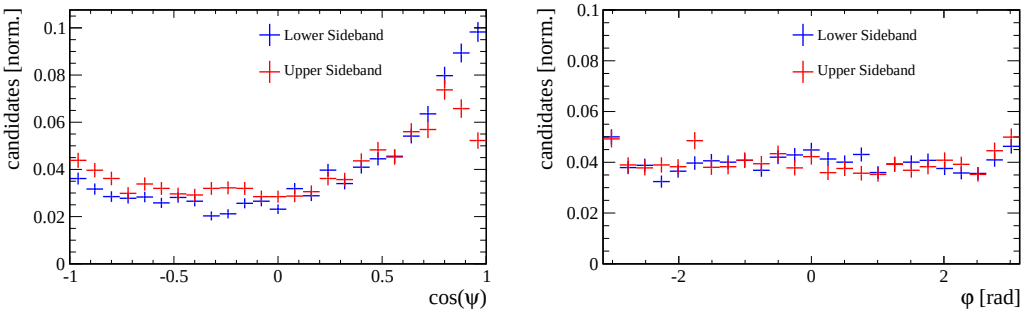

(c) $\cos\psi$ (d) φ

Figure 4.2: *Time and angular distributions of the background for the upper and lower sideband. The plots are normalised to unity.*

5325 to 5400 MeV. The histogram is used explicitly in the PDF. The two sideband regions are visualised in the mass plot shown in Fig. 4.1.
In other words: The angular distributions have to be described explicitly in the fit.

This is achieved by using events from the mass sideband regions. However, one has to verify that these distributions are compatible with those in the region of the peak. This is an important prerequisite for the fitting procedure to work.
This can be done by comparing the distributions from the lower and the upper sideband. If they agree well, then they can be extrapolated to the signal region. In Fig. 4.2 the angular distributions for the upper and lower sideband are shown together with the decay time distributions. Except for the two last bins in the $\cos\psi$ distribution the agreement is very good. The small discrepancy hints to small differences in the two sidebands. However, since both the cFit and an alternative treatment of the background, as described in Subsec. 4.3.3, gives fully compatible results, one can conclude that the observed difference averages out.
Apart from the combinatorial background, there are further contributions from physics background that may peak around the m_{B^0} mass. The method that has been described in this subsection cannot detect peaking background components. The default fit does not include such components. However, the effect of peaking background is treated as systematic uncertainty and is explained in more detail in the next chapter.

4.3.3 Alternative fitting technique

In the fit described above the background components are described explicitly using events from the sideband regions. An alternative approach is the so-called **sFit** method using the sPlot technique described in Sec. 3.4. The sFit method is detailed in [72]. In this case, the background is not explicitly modelled but subtracted in advance. This is obtained by using a fit to the $J/\psi K^+\pi^-$ invariant mass as discriminating variable to assign a weight, W_i, to each candidate, as described in Sec. 3.4. Note that events that are likely to be background are assigned small or negative weights. Then, a maximum likelihood fit is performed where each candidate is weighted by W_i. The fit minimises the negative log likelihood function

$$-\ln\mathcal{L}(\vec{\lambda}) = -\alpha\sum_{i=1}^{N} W_i \ln\mathcal{S}(\vec{x}_i|\vec{\lambda}), \tag{4.18}$$

where $\mathcal{S}(\vec{x}_i|\vec{\lambda})$ is the signal part of the PDF and $\alpha = \sum_{i=1}^{N} W_i / \sum_{i=1}^{N} W_i^2$ a correction factor to ensure the correct determination of the statistical uncertainties for the weighted data sample. The sFit technique is only valid if the discriminating variable is independent from all other observables. As already stated the angular variables are assumed not be correlated with $m(J/\psi K^+\pi^-)$. It is emphasised again that the sFit also assumes that the background can be extrapolated from the mass sidebands to the signal region. The difference to the cFit is that only signal events are used in the maximum likelihood fit and that the background does not have to be modelled explicitly.
As this fit method requires much less computing time, it is chosen as the default fit.

The cFit serves only as a crosscheck and is used to determine a systematic error due to the background modelling.
As for the sFit an explicit background component is not needed and the mass fit is performed separately, only the physics parameters $\vec{\lambda}_{\text{phys}} = \{R_\parallel, R_\perp, F_\text{S}, \delta_\parallel, \delta_\perp, \delta_\text{S}\}$ are considered in the main fit. The decay width is not used to separate signal and background as in the sFit the background is subtracted before the maximum likelihood fit by means of the B^0 mass as discriminating variable. There is no difference in the results of the physics parameters whether the decay time is fixed or floated in the fit. It is therefore not regarded as a full parameter of the fit.

4.3.4 Summary

This subsection summarises the parameters of the given data set and the unknown variables to be determined in the fit. For the sFit only the physics parameters are floating in the fit. For didactic reasons the fitting procedure has been described for only one $K^+\pi^-$ mass bin. It has been explained, however, in Ch. 1 that the analysis is performed in four mass bins to account for the mass dependence of the

Parameter type	One $K^+\pi^-$ mass bin	Four $K^+\pi^-$ mass bins
Measured quantities $\vec{x}$	$t, \cos\psi, \cos\theta, \varphi, m$	$t, \cos\psi, \cos\theta, \varphi, m$
Signal fraction	f_sig	$f_\text{sig}^{(1)}, f_\text{sig}^{(2)}, f_\text{sig}^{(3)}, f_\text{sig}^{(4)}$
Decay width	Γ_d	Γ_d
Physics parameters $\vec{\lambda}_{\text{phys}}$	$R_\parallel, R_\perp, F_\text{S}, \delta_\parallel, \delta_\perp, \delta_\text{S}$	$R_\parallel, R_\perp, F_\text{S}^{(1)}, \delta_\parallel, \delta_\perp, \delta_\text{S}^{(1)}$ $F_\text{S}^{(2)}, \delta_\text{S}^{(2)}$ $F_\text{S}^{(3)}, \delta_\text{S}^{(3)}$ $F_\text{S}^{(4)}, \delta_\text{S}^{(4)}$
Mass parameters $\vec{\lambda}_{\text{det}}$	$m_{B^0}, f_{\text{m},1}^{\sigma}, \sigma_{\text{m},1}^{sig}, \sigma_{\text{m},2}^{sig}$	$m_{B^0}, f_{\text{m},1}^{\sigma,(1)}, \sigma_{\text{m},1}^{sig,(1)}, \sigma_{\text{m},2}^{sig,(1)}$ $f_{\text{m},1}^{\sigma,(2)}, \sigma_{\text{m},1}^{sig,(2)}, \sigma_{\text{m},2}^{sig,(2)}$ $f_{\text{m},1}^{\sigma,(3)}, \sigma_{\text{m},1}^{sig,(3)}, \sigma_{\text{m},2}^{sig,(3)}$ $f_{\text{m},1}^{\sigma,(4)}, \sigma_{\text{m},1}^{sig,(4)}, \sigma_{\text{m},2}^{sig,(4)}$
Background parameters $\vec{\lambda}_{\text{bkg}}$	$\alpha_\text{m}; f_{\tau,1}^{\text{LL}}, \tau_1^{\text{LL}}, \tau_2^{\text{LL}}$	$\alpha_\text{m}^{(1)}; f_{\tau,1}^{\text{LL}}, \tau_1^{\text{LL}}, \tau_2^{\text{LL}}$ $\alpha_\text{m}^{(2)}$ $\alpha_\text{m}^{(3)}$ $\alpha_\text{m}^{(4)}$

Table 4.3: *Free fit paramters for one and four $K^+\pi^-$ mass bins. The superscript indicates the $K^+\pi^-$ mass bins. The parameters also used in the sFit are highlighted in red.*

polarisation amplitudes. The fitting procedure is similar to the case of one $K^+\pi^-$ mass bin, however, several parameters are determined separately in the four bins. First and foremost, these are the S-wave parameters. The P-wave parameters are determined globally. Additionally, four different sets of signal fractions and mass parameters are used, only the B^0 mass is assumed to be the same for all bins. The sFit is performed with four different sets of signal weights, corresponding to the four $K^+\pi^-$ mass regions.
As described in Ch. 1, the coupling factors between S- and P-wave, $C_{\rm SP}$, are taken into account. The numbers for four $K^+\pi^-$ mass bins are listed in Table 1.4.
In Table 4.3 all parameters that are kept floating in the one and four bin fit are shown. Those parameters as well used in the sFit are highlighted in red. The superscript indicates the bin number.
In addition, acceptance and resolution effects are taken into account. The angular distribution of the background is described by a three-dimensional histogram (cFit). None of these parameters are varied in the fit. Only one acceptance histogram is used for all bins. The full cFit in four bins of $m(K^+\pi^-)$ includes 37 free parameters. As the mass fit is separated from the actual fit and the background is not taken into account, the sFit has much less free parameters, only the 12 physics parameters.

4.4 Validation of the fit procedure

It is very important that the fitting procedure is thoroughly tested. The PDF described in this chapter is rather complex, so mistakes leading to biases can easily be introduced. A first validation is to perform a fit to fully simulated $B^0 \to J/\psi K^{*0}$ decays. This allows for a verification of the acceptance correction as well. As the simulation sample does not contain any S-wave contribution, only the first six terms in Eq. 1.22 are used. This allows to perform the fit in only one bin. The background does not have to be taken into account as only signal events are used. The fit results compared to the values with which the simulated sample has been generated are shown in Table 4.4. The agreement is very good, the differences to the generated

Parameter	Fitted result	Generated value	Deviation [σ]
$R_\parallel$	0.2411 ± 0.0015	0.24	0.7
$R_\perp$	0.1601 ± 0.0015	0.16	0.1
$\delta_\parallel$	2.503 ± 0.008	2.50	0.4
$\delta_\perp$	-0.168 ± 0.007	-0.17	0.3

Table 4.4: *Results from a fit to fully simulated signal events compared to the generated value and the difference in standard deviations (statistical errors only).*

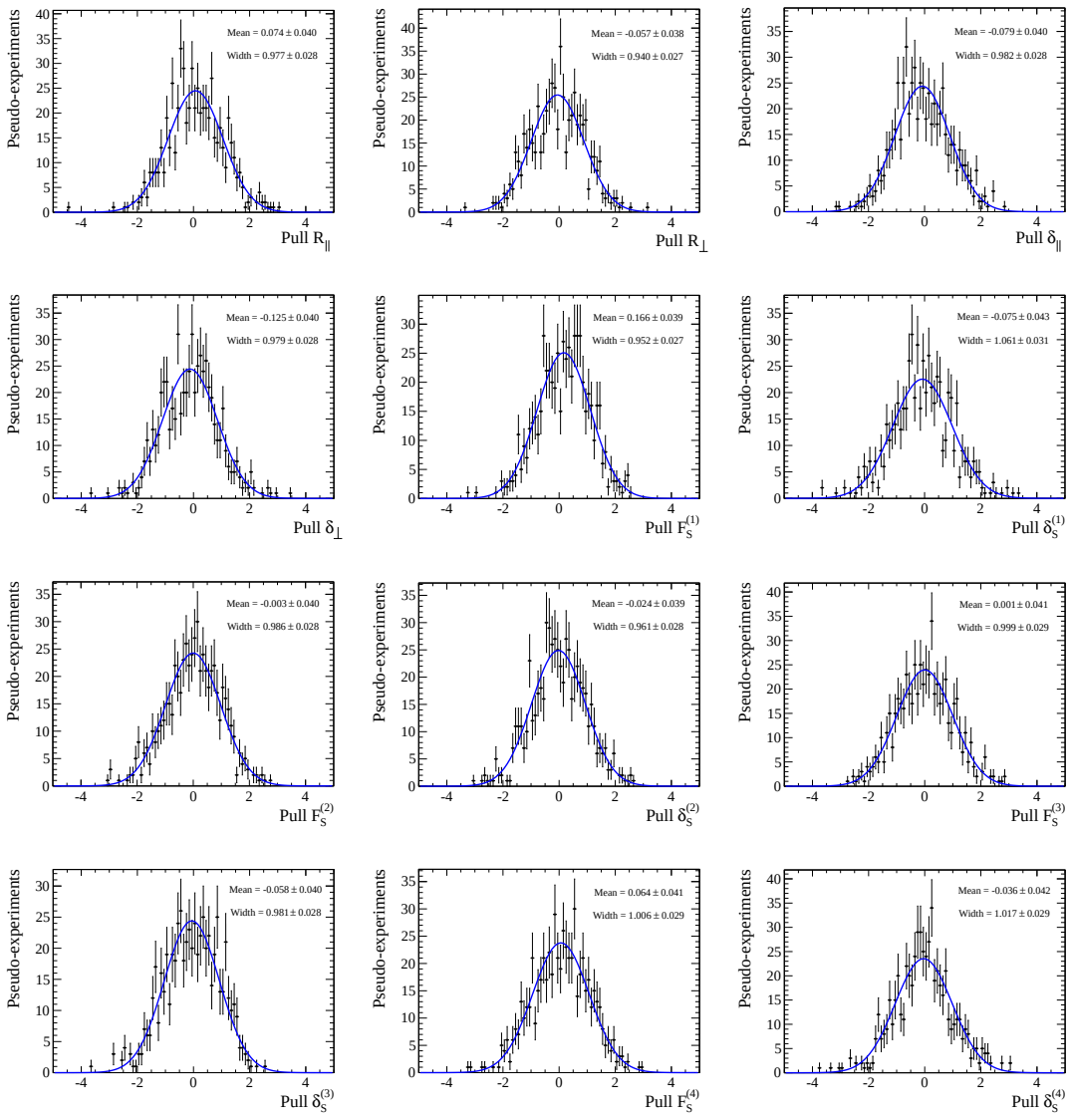

Figure 4.3: *Pull distributions for all sFit physics parameters obtained from a fit to 600 pseudo-experiments.*

values are smaller than one standard deviation.
A method to test the full PDF is the generation of pseudo-experiments. The PDF is used to generate events, corresponding to the number of candidates in each $K^+\pi^-$ mass bin, approximately $10\,000$, $29\,000$, $27\,000$ and $11\,000$ candidates, respectively. A full fit is then performed to the generated set of events. This procedure is repeated 600 times corresponding to 600 pseudo-experiments. As the sFit is the default fit, no background component is included and the free parameters are the physics parameters in the case of an sFit. The best way to see if the fit procedure works is looking

Parameter	Pull mean	Pull width
$R_{\parallel}$	0.074 ± 0.040	0.977 ± 0.028
$R_{\perp}$	-0.057 ± 0.038	0.940 ± 0.027
$\delta_{\parallel}$	-0.079 ± 0.040	0.982 ± 0.028
$\delta_{\perp}$	-0.125 ± 0.040	0.979 ± 0.028
$F_{\mathrm{S}}^{(1)}$	0.166 ± 0.039	0.952 ± 0.027
$\delta_{\mathrm{S}}^{(1)}$	-0.075 ± 0.043	1.061 ± 0.031
$F_{\mathrm{S}}^{(2)}$	-0.003 ± 0.040	0.986 ± 0.028
$\delta_{\mathrm{S}}^{(2)}$	-0.024 ± 0.039	0.961 ± 0.028
$F_{\mathrm{S}}^{(3)}$	0.001 ± 0.041	0.999 ± 0.029
$\delta_{\mathrm{S}}^{(3)}$	-0.058 ± 0.040	0.981 ± 0.028
$F_{\mathrm{S}}^{(4)}$	0.064 ± 0.041	1.006 ± 0.029
$\delta_{\mathrm{S}}^{(4)}$	-0.036 ± 0.042	1.017 ± 0.029

Table 4.5: *Mean values and widths of the pull distributions from* 600 *pseudo-experiments for all physics parameters, corresponding to the plots in Fig. 4.3. Only statistical errors are indicated.*

at pull distributions that show the difference between the fitted and the generated parameter value, divided by the error determined from the fit. An ideal pull plot is Gaussian distributed, centered around zero and has a width of one. This shows that there is no bias and that the normalisation of the fit and the error estimate is correct. The pull distributions for all physics parameters can be seen in Fig 4.3. The mean values and widths are summarised in Table 4.5. All mean values with the exception of $F_{\mathrm{S}}^{(1)}$ and widths are compatible with 0 and 1, respectively. For $F_{\mathrm{S}}^{(1)}$ the deviation of the mean from zero is around four standard deviations. This is more than the usual tolerance of three standard deviations, the absolute bias itself,

Parameter	Fitted result	Generated value	Deviation [σ]
$R_{\parallel}$	0.237 ± 0.004	0.24	0.75
$R_{\perp}$	0.165 ± 0.004	0.16	0.13
$\delta_{\parallel}$	2.54 ± 0.02	2.50	2.0
$\delta_{\perp}$	-0.14 ± 0.02	-0.17	1.7

Table 4.6: *Results from a fit to fully simulated signal events including events from the data sidebands compared to the generated value and the difference in standard deviations. Only statistical errors are indicated.*

however, is very small (deviation of roughly 0.17σ from zero). Therefore, this bias is not further considered.
One further crosscheck has been performed to also validate the background description of the PDF. Note that the tests discussed in this section so far have not included a background component. Now, background from the data mass sidebands are embedded in the simulation sample. To describe the background in the signal region, an offset of 50 MeV is added to events from the lower sideband and subtracted from the events in the upper sideband. Hence, the fit is performed in a limited mass range from 5200 to 5350 MeV instead of the full interval [5150, 5400] MeV. In total, $60\ 000$ events from simulation and $9\,400$ sideband events, corresponding to a signal fraction of approximately 85%, are used. An sFit is performed, i.e. the B^0 mass is fitted for before the full maximum likelihood procedure. The results are compatible with the generated values which can be seen in Table 4.6. Note again that the simulation does not contain any S-wave component. Thus, only the P-wave parameters can be extracted from the fit.

4.5 Nominal sFit results and comparison with cFit

The purpose of this section is mainly to introduce the nominal sFit results from data because they are referred to in the following chapters. These results are discussed in detail in Ch. 9.
As a first step a comparison between the sFit and the cFit is performed. Both fits to data are carried out in four $K^+\pi^-$ mass bins. Note that the S-wave fraction and the corresponding phase are averaged over the four bins to allow for an easier comparison between the two sets of results. It has been noted in Subsec. 1.4.3 that there are two solutions for the strong phases. The results shown here represent the physical solution of the 2-fold ambiguity. This is discussed in more detail in Ch. 9. The angular acceptance corresponds to the acceptance factors shown in Table 4.1.

Parameter	sFit result	cFit value
$R_\parallel$	0.227 ± 0.004	0.229 ± 0.004
$R_\perp$	0.201 ± 0.004	0.200 ± 0.004
$\delta_\parallel$	-2.94 ± 0.02	-2.94 ± 0.02
$\delta_\perp$	2.94 ± 0.02	2.94 ± 0.02
F_S	0.064 ± 0.004	0.063 ± 0.004
δ_S	2.30 ± 0.03	2.30 ± 0.03

Table 4.7: *Results of a four bin fit to data for both sFit and cFit. The error is statistical only. The S-wave parameters are averaged over the four bins.*

Parameter	Default results
$R_{\parallel}$	0.227 ± 0.004
$R_{\perp}$	0.201 ± 0.004
$\delta_{\parallel}$	-2.94 ± 0.02
$\delta_{\perp}$	2.94 ± 0.02
$F_{\mathrm{S}}^{(1)}$	0.115 ± 0.007
$\delta_{\mathrm{S}}^{(1)}$	3.09 ± 0.10
$F_{\mathrm{S}}^{(2)}$	0.049 ± 0.004
$\delta_{\mathrm{S}}^{(2)}$	2.66 ± 0.06
$F_{\mathrm{S}}^{(3)}$	0.052 ± 0.006
$\delta_{\mathrm{S}}^{(3)}$	1.94 ± 0.03
$F_{\mathrm{S}}^{(4)}$	0.105 ± 0.014
$\delta_{\mathrm{S}}^{(4)}$	1.53 ± 0.03

Table 4.8: *Nominal fit results to data (sFit) for further reference in subsequent chapters. Only the statistical error is indicated.*

The results can be seen in Table 4.7. The agreement between both fitting techniques is very good. This shows that both approaches to treat the background - explicitly modelling the distributions in the fit and statistically subtract the background before the main fit - are fully equivalent.

In Table 4.8 the results of the full default sFit performed in four $K^+\pi^-$ mass bins using the acceptance factors in Table 4.1 are shown. They serve as reference for the following chapters.
Both fitting techniques assume no peaking background components in the region around the known B^0 mass [5]. The next chapter is dedicated to the detailed study of these components.

Chapter 5

Background composition

Divide each difficulty into as many parts as is feasible and necessary to resolve it.

René Descartes (1596-1650)

As already stated in Sec. 4.5 this chapter is dedicated to the detailed investigation of peaking background. After a short introduction the main physical backgrounds are discussed. In addition, peaking background from misreconstructed events is studied.

5.1 Introduction

One of the main difficulties in the selection of $B^0 \to J/\psi K^{*0}$ candidates is the correct treatment of the background. In the last chapter it has been assumed that the entire background can be described by components that are flat in the B^0 mass. For this, events from the sidebands are used. It will turn out that this is a good approximation and the default maximum likelihood fit does not take into account further contributions. They are only considered to estimate systematic effects. Nevertheless, it is very important to investigate if there are so-called peaking background components, i.e. non-signal events that form a peak around the known B^0 mass [5]. As these structures are not visible in the mass sidebands, one has to partially rely on simulated events.
However, using **data** an estimate of the most prominent categories of selected $B^0 \to J/\psi K^{*0}$ candidates can be performed. Apart from the signal, there are three main background components which are determined by a simultaneous fit to the reconstructed B^0 and J/ψ mass distributions. For the signal parts a sum of two Gaussian functions and a Crystal Ball function with a double Gaussian core are used, respectively, as described in Sec. 3.4. The background distributions are modelled with an exponential function. In Fig. 5.1 the two-dimensional distribution of the invariant $J/\psi K^+\pi^-$ and $\mu^+\mu^-$ mass is shown for illustration purposes. In summary, the $B^0 \to J/\psi K^{*0}$ candidates can be classed in one signal and three background categories:

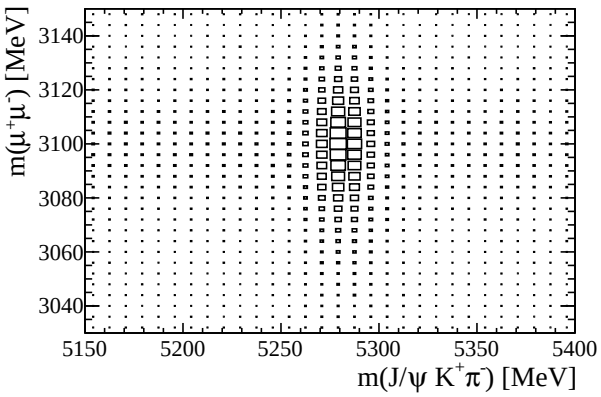

Figure 5.1: *Two-dimensional mass distribution where the invariant $J/\psi K^+\pi^-$ mass is plotted on the x-axis and the invariant $\mu^+\mu^-$ mass on the y-axis using all selected candidates from data.*

1. **Signal**: As shown in Table 3.2 the signal fraction in the entire selected mass range determined by a data fit to the B^0 mass is approximately 79%. This indicates a very low background level. The signal distribution peaks in the B^0 mass as well as in the J/ψ mass.

2. **Background from true J/ψ decays**: The most common background category consists of B decays formed from a true J/ψ meson and two further randomly chosen tracks. It is expected that these candidates peak in the J/ψ mass but show a flat distribution in the B^0 mass. This is called J/ψ background. From the simultaneous fit described above, this fraction is estimated to be approximately 17%.

3. **Background originating not from true J/ψ decays**: On the other hand, background candidates that do not peak in the J/ψ mass but show a peak in the B^0 mass, so-called non J/ψ background, do not have a large contribution. In fact, the simultaneous fit shows that it is compatible with zero.

4. **Combinatorial background**: The remaining candidates do not peak in either of the two mass distributions. This is formed from four randomly selected tracks and represents a fraction of approximately 4%.

In conclusion, only J/ψ and combinatorial background that does not peak in the B^0 mass have a significant contribution. However, this is only a first estimate. It is essential to investigate the background from **simulated events** which allows a more detailed analysis. In the next section several sources of physical background that can lead to peaking components are studied.

5.2 Physical background

In this section, several possible contributions from physical background components are investigated. These are candidates from other decay channels that pass the $B^0 \to J/\psi K^{*0}$ selection. As these are mostly candidates from $B \to J/\psi X$ decays, these processes can peak in the B^0 signal region. The decays considered here have similar branching fractions as the signal decay (remember: $\mathcal{B}(B^0 \to J/\psi K^{*0}) = (1.34 \pm 0.06) \cdot 10^{-3}$ [5]).
There can be contaminations from the decay channels $B^+ \to J/\psi K^{*+}(K^+\pi^0)$ and $B^+ \to J/\psi K^{*+}(K_s\pi^+)$. The branching fraction is $\mathcal{B}(B^+ \to J/\psi K^{*+}) = (1.44 \pm 0.08) \cdot 10^{-3}$ [5]. To estimate their contribution the corresponding fully simulated samples are used, each containing 1 million events. These events are processed with the $B^0 \to J/\psi K^{*0}$ selection. 44 and 80 events pass the selection, respectively. As the mass distributions are flat (see Fig. 5.2), these contributions are treated by the fit and therefore, do not have to be modelled explicitly. Similarly, 760 000 simulated $B_s^0 \to J/\psi\eta'$ events and 5 million simulated $B_s^0 \to J/\psi\phi$ events are used to determine further background sources. The branching fractions are $\mathcal{B}(B_s^0 \to J/\psi\eta') = (3.7^{+1.0}_{-0.9}) \cdot 10^{-4}$ [5] and $\mathcal{B}(B_s^0 \to J/\psi\phi) = (1.05 \pm 0.11) \times 10^{-3}$ [73], respectively, and after applying the $B^0 \to J/\psi K^{*0}$ selection, 688 and 850 candidates remain. The invariant mass distributions can be seen in Fig. 5.3. The first distribution is flat but the second shows a clear peak. Therefore, the $B_s^0 \to J/\psi\phi$ background needs further consideration.
To estimate the fraction of $B_s^0 \to J/\psi\phi$ events one would expect in the $B^0 \to J/\psi K^{*0}$ data sample, first the integrated luminosity corresponding to the 5 million simulated events is calculated by using

$$\mathcal{L}_{\text{int}} = \frac{N}{2 \cdot \sigma_{b\bar{b}} \cdot f_B \cdot \mathcal{B}_{\text{vis}}[B_s^0 \to J/\psi(\mu^+\mu^-)\phi(K^+K^-)] \cdot \epsilon_{\text{gen}}}, \tag{5.1}$$

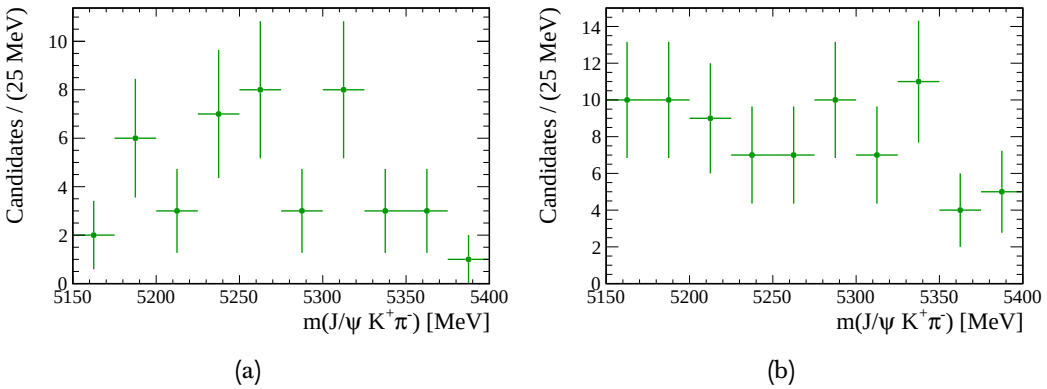

Figure 5.2: *Invariant B^0 mass distribtion using (a) $B^+ \to J/\psi K^{*+}(K^+\pi^0)$ and (b) $B^+ \to J/\psi K^{*+}(K_s\pi^+)$ simulated events.*

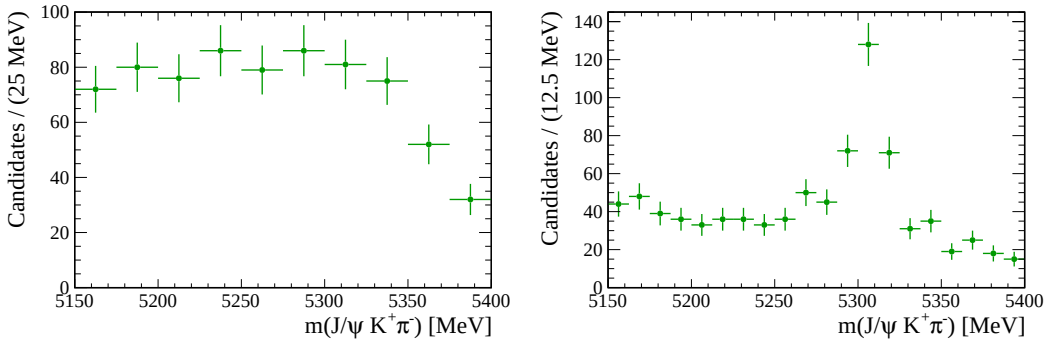

(a) (b)

Figure 5.3: *Invariant B^0 mass distribtion using (a) $B_s^0 \to J/\psi\eta'$ and (b) $B_s^0 \to J/\psi\phi$ simulated events.*

where N is the number of generated events, $\sigma_{b\bar{b}} = (288 \pm 4 \pm 48)\mu$b [42] is the production cross-section of $b\bar{b}$ pairs, $f_B = 0.105 \pm 0.006$ [5] is the hadronisation fraction of B_s^0 mesons, $\mathcal{B}_{\text{vis}}[B_s^0 \to J/\psi(\mu^+\mu^-)\phi(K^+K^-)] = 3.16 \cdot 10^{-5}$ [5] is the visible branching ratio of the simulated decay and $\epsilon_{\text{gen}} = 0.3283 \pm 0.0008$ [74] the efficiency of the selection requirements that are applied during the generation of the events (e.g. detector geometry). The factor of 2 takes into account that b quarks are produced in pairs. The result is $\mathcal{L}_{\text{int}} \approx 8$ fb^{-1}. Scaled to the integrated luminosity of the collected data sample, the selected 850 simulated candidates correspond to 107 $B_s^0 \to J/\psi\phi$ background candidates or a fraction of approximately 0.2% with respect to the number of signal candidates. This is negligible hence, the background pollution from $B_s^0 \to J/\psi\phi$ events can be neglected.
Similarly, a contribution from $\Lambda_b^0 \to J/\psi Kp$ decays has been found to be negligible. This contributions has been particularly investigated as such events can be selected if the mass hypothesis of the pion is replaced with that of a proton. The branching fraction itself is small, $\mathcal{B}(\Lambda_b^0 \to J/\psi Kp) = (4.8 \pm 0.9) \cdot 10^{-6}$ [5].
In Fig 3.1(c) one can see a very small peak at around 5370 MeV which originates from a contribution of $B_s^0 \to J/\psi\overline{K}^{*0}$ events. These events can be modelled separately in the fit by using an additional Gaussian function to describe the mass shape. Performing a fit including this additional background component gives the same results for the physics parameters (at the current precision). Therefore, the contribution from $B_s^0 \to J/\psi\overline{K}^{*0}$ events can be neglected [28].
Finally, it can happen that the mass hypotheses of the pion and the kaon are swapped. It has been shown, however, that these double misidentifications are very rare and consequently are neglected in this analysis [28].
Apart from physical background sources, misreconstructed events can lead to peaking components around the known B^0 mass [5].

5.3 Further background studies

These misreconstructed events are studied in more detail with a simulated signal sample (as described in Ch. 3) using the LHCb framework summarised in [75]. Of course, a simulated signal sample per definition does not contain background events, however, it shows how many events are misreconstructed and what the properties of these events are. These misreconstructed components have also to be considered in data. Only such components that peak in the B^0 signal region are of interest because they cannot be treated by the sPlot technique or other background subtraction methods. This can lead to a significant bias in the determination of the physics parameters. All other components that are flat in the B^0 mass can be extrapolated from the sidebands to the signal region and are treated correctly by the background subtraction methods.
Applying the full $B^0 \to J/\psi K^{*0}$ selection to the simulated signal sample shows that there are only two significant peaking contributions left, the "low mass" and the "misreconstructed background" component. It can be debated whether the latter should be labelled as background as it rather describes reconstruction artefacts. However, since this component needs to be taken into account in data, it is referred to as background in the following. Other peaking components are largely reduced, mainly due to the hard criterion on the pion probability listed in Table 3.1. A summary can be found in Table 5.1. There are also background fractions that are uncategorised (further components) but they either do not peak or the angular distributions are similar to those observed for signal candidates. The mass and angular distributions of the low mass and misreconstructed background components and the signal can be seen in Fig. 5.4 and Fig. 5.5.
The low mass component consists of reconstructed B^0 candidates with invariant mass that is systematically below the known B^0 mass [5]. A more extensive study using simulated events shows that in almost all events the J/ψ meson emits a photon but otherwise the process behaves like a signal event. As can be seen from Fig. 5.5 the angular distributions are similar to those observed for signal candidates. Hence, this component can be classified as signal. The candidates classed as mis-

Category	Events / Fractions
Selected candidates	404 624
Signal fraction	0.906
Low mass fraction	0.044
Misreconstructed background fraction	0.035
Fraction of further components	0.015

Table 5.1: *Composition of the simulated signal sample.*

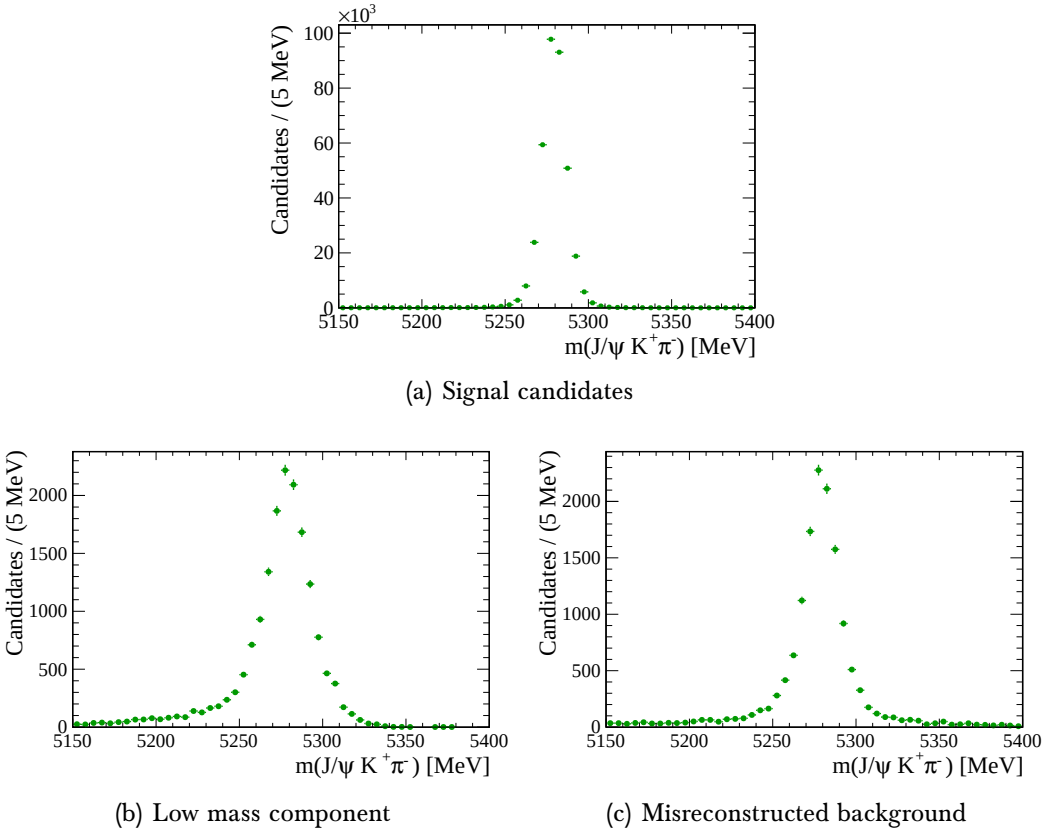

(a) Signal candidates

(b) Low mass component

(c) Misreconstructed background

Figure 5.4: *Invariant B^0 mass distribtion of signal candidates compared to the low mass and misreconstructed background component using simulated signal events.*

reconstructed background consist of at least one track that has not been correctly reconstructed. In most of the cases this is the pion track. Figure 5.5 shows that the angular distributions are different from the signal distributions. Especially candidates that have a large positive value of $\cos\psi$ deviate significantly from the signal distribution. However, from further studies it can be concluded that only 40% of these candidates have a different angular shape as the signal events. The remaining candidates show a signal-like behaviour.
In conclusion, the only component that needs to be taken into account and cannot be described by contributions that are flat in the B^0 mass is the misreconstructed background category. A further background category can easily be included in the fitter by adding the following component to Eq. 4.16

$$\mathcal{B}_{\mathrm{mrec}}(\vec{x}|\vec{\lambda}) = f_{\mathrm{mrec}} \cdot \mathcal{B}_{m,\mathrm{mrec}}(m|\vec{\lambda}_{\mathrm{mrec}}) \cdot \mathcal{B}_t(t|\vec{\lambda}_{\mathrm{bkg}}) \cdot \mathcal{B}_{\Omega,\mathrm{mrec}}(\Omega), \tag{5.2}$$

where f_{mrec} is the overall fraction of misreconstructed background candidates and $\mathcal{B}_t(t|\vec{\lambda}_{\mathrm{bkg}})$ the same decay time parametrisation as used for the flat background (i.e.

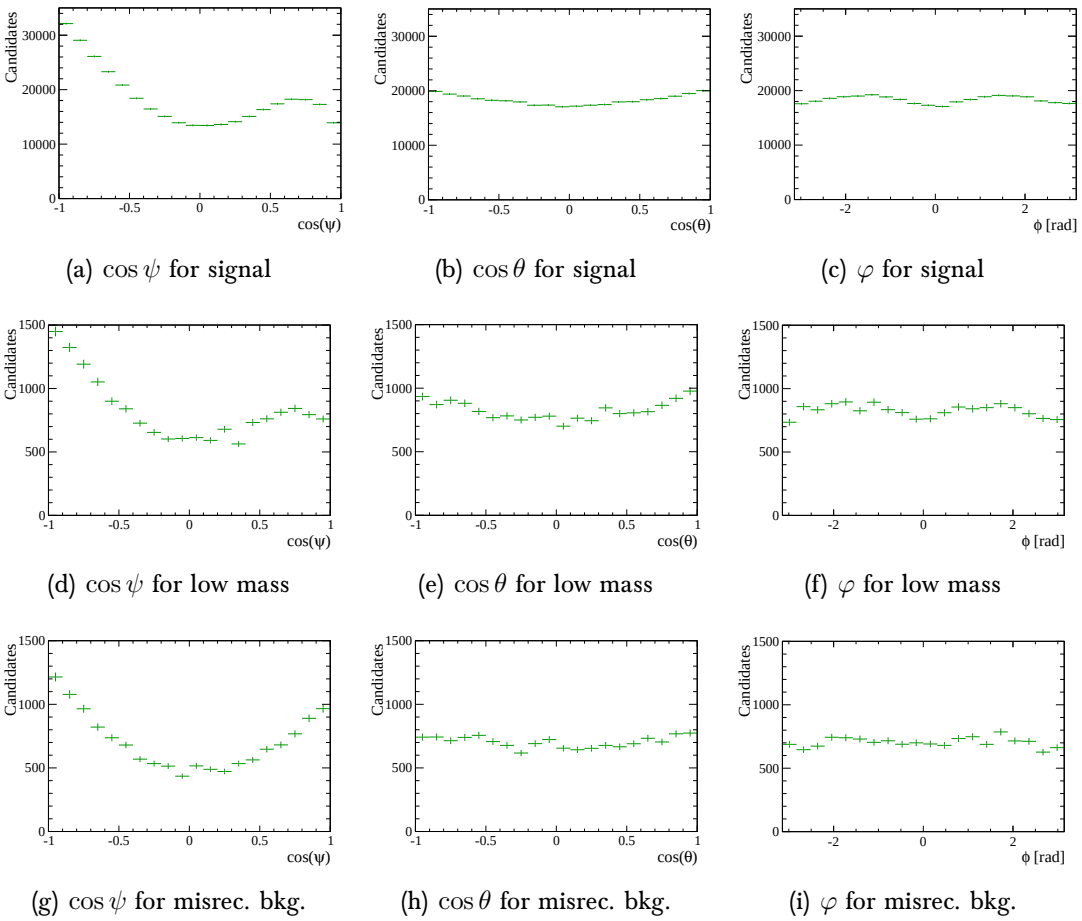

(a) $\cos\psi$ for signal (b) $\cos\theta$ for signal (c) φ for signal

(d) $\cos\psi$ for low mass (e) $\cos\theta$ for low mass (f) φ for low mass

(g) $\cos\psi$ for misrec. bkg. (h) $\cos\theta$ for misrec. bkg. (i) φ for misrec. bkg.

Figure 5.5: *Angular distribtions of signal candidates compared to the low mass and misreconstructed background component using simulated signal events.*

the sum of two exponentials). The mass parameters and angular distributions describing these candidates are taken from simulation. The angular distributions are described by a three-dimensional histogram with seven bins in each angular dimension. The mass PDF can be modelled by the sum of two Gaussian functions plus an exponential function (no physics motivation). The mass distribution is shown in Fig. 5.6. The corresponding fit parameters can be found in Table 5.2. The mass peak is slightly shifted to smaller values and has a larger width compared to the signal distribution. The mass parameters are used in the maximum likelihood fit and are fixed to the values as shown in Table 5.2. The fraction of misreconstructed background candidates is fixed as well in the full likelihood fit to 3.5% as listed in Table 5.1. The fit including the misreconstructed background component of 3.5% gives results close to those using the default conditions documented in the last chapter. The difference to the default results is taken as systematic error (see Ch. 8).

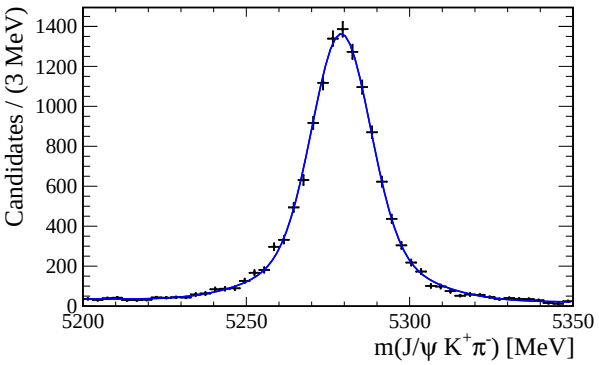

Figure 5.6: *Invariant mass distribtion of the misreconstructed background component fitted with the sum of two Gaussian functions plus an exponential function using simulated signal events.*

Parameter	Fit result
$m_{B^0,\mathrm{mrec}}$	5278.99 ± 0.01 MeV
$f^{\sigma}_{\mathrm{m},1,\mathrm{mrec}}$	0.741 ± 0.018
$\sigma^{sig}_{\mathrm{m},1,\mathrm{mrec}}$	9.55 ± 0.21 MeV
$\sigma^{sig}_{\mathrm{m},2,\mathrm{mrec}}$	28.65 ± 1.70 MeV
$\alpha_{\mathrm{m,mrec}}$	-0.0033 ± 0.0005

Table 5.2: *Fit values corresponding to the distribution shown in Fig. 5.6.*

Varying the fraction up to 5% or using only candidates with angular distributions different from the signal distribution does not change the physics results.

In conclusion, the background can be described by a flat component to a good approximation. Only the misreconstructed background component does peak around the known B^0 mass [5]. To estimate the systematic effect of neglecting this contribution in the default fit, an additional background component is simulated explicitly in the fit. The results are slightly different and the variation is taken as systematic error. The relevant numbers are summarised in Sec. 8.3.

Chapter 6

Angular acceptance determination

> No problem can withstand the assault of sustained thinking.
>
> *Voltaire (1694-1778)*

As the determination of the angular detector acceptance relies entirely on simulated events, it is important that all kinematic distributions, like the momenta of final state particles, agree with those in data. This is especially the case as the acceptance shape is largely dependent on the detector geometry and momentum requirements. In this chapter an extensive comparison between simulated signal candidates and background subtracted data is presented. Furthermore, an iterative method is described to distinguish between differences related to the physics model used in the generation of the simulated events and detector efficiency effects.

6.1 Initial differences

As can be seen from Fig. 6.1, the pseudorapidity (η) and the transverse momentum (p_{T}) distributions for B^0 meson candidates are different for data and simulation. To estimate the effect on the acceptance determination the two distributions from simulated events (denoted as sim) are reweighted simultaneously such that they match the data distributions. Schematically, this can be written as

$$\mathrm{histogram}^{\mathrm{new}}_{\mathrm{sim}} = \mathrm{histogram}^{\mathrm{old}}_{\mathrm{sim}} \cdot \frac{\mathrm{histogram}_{\mathrm{data}}}{\mathrm{histogram}^{\mathrm{old}}_{\mathrm{sim}}} = \mathrm{histogram}^{\mathrm{old}}_{\mathrm{sim}} \cdot R, \qquad (6.1)$$

where R denotes the weight with which the initial histogram is modified. In this case here, both the pseudorapidity and the transverse momentum of the B^0 meson are reweighted separately. The same procedure has also been performed in two dimensions but no differences have been found compared to two separate reweightings. A new acceptance histogram is determined using the weighted distributions from simulation and a new maximum likelihood fit is performed. It has been explained in Subsec. 4.3.1 that the acceptance histogram is determined by the ratio of selected

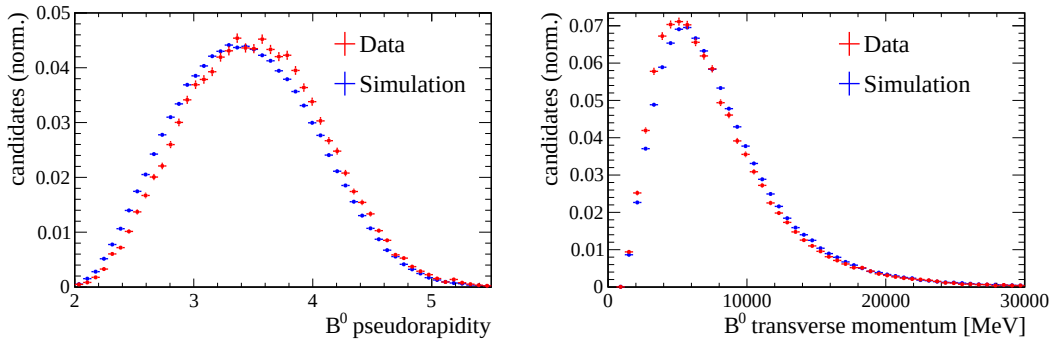

Figure 6.1: *Comparison between simulation and data, showing the pseudorapidity and the transverse momentum of the B^0 meson. The plots are normalised to unity.*

events and the theoretical expectation. By the reweighting procedure the theory remains unchanged but the distribution of selected events is modified. Consequently, only the numerator of the acceptance histogram is altered, the denominator is not changed. The effect of reweighting the acceptance can be best visualised by comparing the calculated acceptance factors for the original and the reweighted simulated events. From Table 6.1 one can conclude that the reweighting has only a small effect on the acceptance. Using the new acceptance histogram the fit parameters either do not change or the difference to the original values is much smaller than the statistical

Factor	No reweighting	Reweighting in $\eta(B^0)$ and $p_T(B^0)$
ξ_1	0.9027 ± 0.0017	0.9046 ± 0.0018
ξ_2	1.1347 ± 0.0024	1.1447 ± 0.0025
ξ_3	1.1408 ± 0.0025	1.1505 ± 0.0026
ξ_4	0.0006 ± 0.0017	0.0004 ± 0.0017
ξ_5	-0.0112 ± 0.0011	-0.0107 ± 0.0011
ξ_6	-0.0007 ± 0.0010	-0.0007 ± 0.0011
ξ_7	1.0084 ± 0.0019	1.0140 ± 0.0020
ξ_8	-0.0135 ± 0.0016	-0.0130 ± 0.0016
ξ_9	0.0011 ± 0.0015	0.0015 ± 0.0015
ξ_{10}	-0.2709 ± 0.0026	-0.2739 ± 0.0030

Table 6.1: *Acceptance factors before any reweighting and after reweighting in $\eta(B^0)$ and $p_T(B^0)$. The factors do not change significantly. The effect on the physics parameters is negligible.*

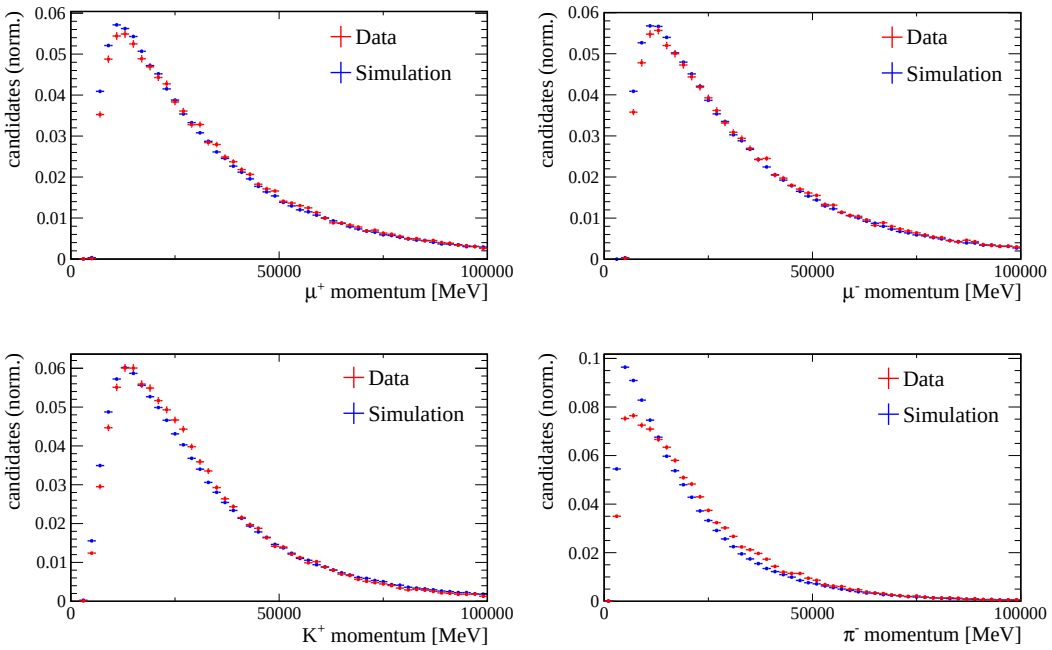

Figure 6.2: *Comparison between simulation and data, showing the momentum distributions of the four final state particles after reweighting of the B^0 kinematics. The plots are normalised to unity.*

error. Thus, no systematic error is assigned due to the reweighting of the B^0 meson kinematics. It has been verified that other kinematic distributions of the B^0 are not affected. The reweighted acceptance is used in the default fit as shown in Table 4.7. It is expected that the kinematics of the B^0 meson do not affect the measurement of the polarisation amplitudes to a large extent as they are determined by the transversity angles between the final state particles. Furthermore, the disagreement between data and simulation for kinematic distributions of the B^0 meson is a known problem at LHCb.

To the contrary, the kinematic distributions of the four particles in the final state largely affect the angular distributions and thus, the measurement of the polarisation amplitudes and phases. These distributions are investigated in the following. Significant deviations between data and simulation have only been found for the momentum distributions which are shown in Fig. 6.2. There is a good agreement for the muons. The agreement is much poorer for the pion and the kaon. Especially the pion momentum distribution shows a very large discrepancy at low values. It has to be emphasised that the polarisation amplitudes largely depend on the kinematics of the final state particles as the amplitudes describe the relative orientation of the spins of the J/ψ and the K^{*0} mesons.

Factor	Reweighting in $\eta(B^0)$ and $p_{\mathrm{T}}(B^0)$	Reweighting in $p(K^+,\pi^-)$
ξ_1	0.9046 ± 0.0018	0.9051 ± 0.0018
ξ_2	1.1447 ± 0.0025	1.1616 ± 0.0025
ξ_3	1.1505 ± 0.0026	1.1670 ± 0.0026
ξ_4	0.0004 ± 0.0017	0.0001 ± 0.0017
ξ_5	-0.0107 ± 0.0011	-0.0090 ± 0.0011
ξ_6	-0.0007 ± 0.0011	-0.0008 ± 0.0011
ξ_7	1.0140 ± 0.0020	1.0240 ± 0.0020
ξ_8	-0.0130 ± 0.0016	-0.0154 ± 0.0016
ξ_9	0.0015 ± 0.0015	0.0018 ± 0.0015
ξ_{10}	-0.2739 ± 0.0030	-0.4513 ± 0.0030

Table 6.2: *Acceptance factors after reweighting in $\eta(B^0)$ and $p_T(B^0)$ and after additional reweighting in $p(K^+,\pi^-)$. The difference is largest for ξ_{10}.*

In principle, a similar reweighting procedure as for the pseudorapidity and the transverse momentum of the B^0 could be performed using the pion and the kaon as both final state particles are highly correlated (for the full procedure see next section). However, as can be seen from Table 6.2, such a procedure would change the acceptance factors and the fit results significantly. This is expected due to the large correlation between the kinematics of the final state particles (the pion is most relevant due to the large discrepancy) and the amplitudes. Especially the acceptance factor ξ_{10} is largely affected. Moreover, as the origin of the discrepancy is not fully understood, such a reweighting of the acceptance is not a valid approach.

6.2 Pion momentum difference: S-wave contribution

The differences in the pion momentum can be attributed to two different effects. The discrepancy can either be induced by the physical differences between data and simulation (the polarisation amplitudes are not the same), which lead to a significantly different momentum distribution in data and simulation, or by an insufficient detector description in the simulation. In this section a method is introduced that removes the discrepancy due to physics effects.
The simulated event sample used for this analysis does not include any S-wave component. Non-resonant $K^+\pi^-$ contributions have different kinematic distributions than resonant K^{*0} components. In particular it has been tested that the S-wave component populates low pion momentum ranges. This served as motivation to assess the effect of the S-wave component on the kinematic distributions of the final

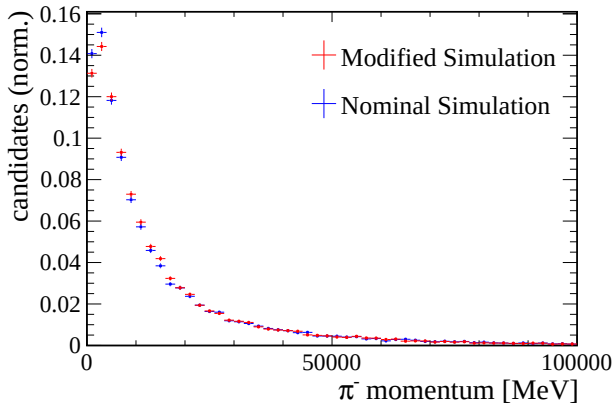

Figure 6.3: *Pion momentum spectrum using simulated raw events for nominal and modified generated amplitudes. These simulated samples are generated without any detector description and reconstruction. The plots are normalised to unity. Note that only detector geometry and momentum cuts have been applied.*

state particles. As a fully simulated sample including an S-wave component does not exist, a data-driven method has been developed to effectively add an S-wave contribution to the simulated sample. This procedure is explained in more detail later in this section.
In addition, the simulated sample is generated with physics parameters (amplitudes, phases) that are not consistent with those being measured in data. To see the effect of different generation values on the pion momentum several samples are generated without any detector description and reconstruction, i.e. only raw events are simulated. Even changing the amplitudes and phases in the generation significantly does not change the kinematic distributions enough to explain the observed discrepancy. As an example, Fig. 6.3 shows the pion momentum distribution for the nominal simulation and for a scenario where the generated polarisation amplitudes have been changed by approximately 50%. The effect on the pion momentum spectrum is small. Note that only detector geometry and momentum cuts have been applied. Thus, Fig. 6.3 is mainly shown for illustration purposes.
To decrease the pion momentum discrepancy a method is used that effectively introduces an S-wave component to the simulation and takes the differences in the physics parameters between data and simulation into account. The method consists of the following steps:

1. The angular part of the PDF as defined in Eq. 4.12 is calculated for every event in two different ways. First, neglecting the S-wave components and using the values of the physics parameters with which the simulation has been generated as input. This corresponds to a set of parameter values V_{gen}. Second, the estimated amplitudes from a fit to data, V_1, are used as an input for the PDF,

i.e. the S-wave component is included. For each event the ratio R_{PDF} between the two PDF values is calculated, hence each event is assigned a weight. This can be formally depicted as

$$R_{\mathrm{PDF},1} = \frac{\mathrm{PDF}(\Omega)|_{V_1}\ (\text{S-wave})}{\mathrm{PDF}(\Omega)|_{V_{\mathrm{gen}}}\ (\text{no S-wave})}. \tag{6.2}$$

2. The kinematic distributions are then reweighted by the ratio determined in Step 1 according to Eq. 6.1. This effectively yields a distribution of simulated events containing an S-wave component and using the best estimates for the physics parameters V_1 determined in a fit to data. Note that the acceptance histogram itself is not changed by this procedure as the acceptance does not directly depend on the polarisation amplitudes. Formally, the numerator and the denominator of the acceptance histogram are weighted by $R_{\mathrm{PDF},1}$ because both the number of selected and expected B^0 candidates depend on the transversity angles. Consequently, the reweighting cancels.

3. After this "physics reweighting" there is a remaining difference in the pion momentum spectrum. This so-called residual difference in the pion and also the kaon momentum (both are highly correlated and introducing an S-wave component has an effect on both quantities) are taken to further reweight the simulation so that the distributions from simulation and data agree. This second reweighting is done in the same way as for the reweighting in the pseudorapidity and the transverse momentum of the B^0, i.e. the two momentum distributions are reweighted separately. However, in this case two iterations are needed until both simulated distributions agree with data. The acceptance factors do change as the physics is unchanged and the denominator of the acceptance histogram is not modified.
   In total, two reweightings are performed, the "physics reweighting" by the PDF ratio described in Step 1 and the residual reweighting of the momentum distributions explained in this step. Hence, the total weight applied to the simulation is
$$R_{\mathrm{tot},1} = R_{\mathrm{PDF},1} \cdot R_{\mathrm{momentum},1}. \tag{6.3}$$

4. The acceptance histogram reweighted as described in Step 3 is then used to perform a new fit to data. The results give a different estimate for the physics parameters V_2 as those of the previous fit to data. These new results are used as input for Step 1 and a new PDF ratio $R_{\mathrm{PDF},2}$ is determined for each event. In addition, the residual reweighting is performed, yielding a new total weight $R_{\mathrm{tot},2}$.

5. The full procedure is re-iterated obtaining new estimates $V_3, V_4, \ldots$ until it converges, i.e. neither the acceptance weights nor the fit results change significantly compared to the previous iteration. For this analysis the first iteration is the most significant and four iterations are sufficient.

Factor	Before iterations	Iteration 1	Iteration 2	Iteration 3	Iteration 4
ξ_1	0.9046 ± 0.0018	0.8973	0.8976	0.8982	0.8985
ξ_2	1.1447 ± 0.0025	1.1665	1.1705	1.1720	1.1727
ξ_3	1.1505 ± 0.0026	1.1725	1.1765	1.1781	1.1788
ξ_4	0.0004 ± 0.0017	0.0002	0.0002	0.0002	0.0002
ξ_5	-0.0107 ± 0.0011	-0.0110	-0.0111	-0.0112	-0.0112
ξ_6	-0.0007 ± 0.0011	-0.0008	-0.0008	-0.0008	-0.0008
ξ_7	1.0140 ± 0.0020	1.0247	1.0273	1.0284	1.0290
ξ_8	-0.0130 ± 0.0016	-0.0117	-0.0115	-0.0114	-0.0113
ξ_9	0.0015 ± 0.0015	0.0017	0.0017	0.0017	0.0017
ξ_{10}	-0.2739 ± 0.0030	-0.2530	-0.2404	-0.2332	-0.2292

Table 6.3: *Acceptance factors before the iterative acceptance determination and after each iteration and residual reweighting. The method converges after four steps. The statistical errors are the same for all iterations.*

Parameter	Before iteration	Iteration 1	Iteration 2	Iteration 3	Iteration 4
$R_\parallel$	0.236 ± 0.004	0.228	0.228	0.228	0.227
$R_\perp$	0.209 ± 0.004	0.202	0.202	0.201	0.201
$\delta_\parallel$	-2.96 ± 0.02	-2.95	-2.94	-2.94	-2.94
$\delta_\perp$	2.93 ± 0.02	2.94	2.94	2.94	2.94
F_S	0.062 ± 0.003	0.061	0.063	0.064	0.064
δ_S	2.24 ± 0.02	2.27	2.29	2.29	2.30

Table 6.4: *Fit results before the iterative acceptance determination and after each iteration and residual reweighting. The errors are statistical only and the same for all iterations. The S-wave parameters are averaged over the four $K^+\pi^-$ mass bins.*

The fits are performed in the four bins of the $K^+\pi^-$ mass. In the case of the PDF reweighting, the C_SP factors are used depending on the $K^+\pi^-$ mass bin of the event. Note that only one acceptance histogram is used for each $K^+\pi^-$ bin. The calculation of four different acceptance histograms corresponding to the four mass bins does not change the fit results significantly and is not performed. This is discussed in more detail in Sec. 7.1. For the PDF reweighting, an S-wave fraction and phase averaged over the four mass bins is used. A reweighting with four different values does not change the results significantly.

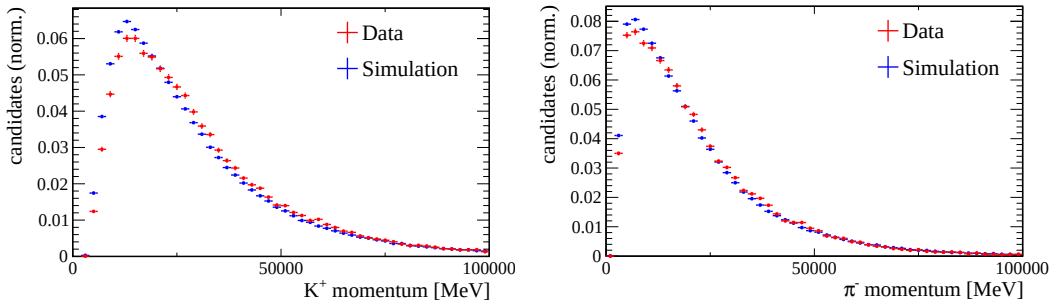

Figure 6.4: *Comparison between simulation and data, showing the momentum distributions of the kaon and the pion after the iterative procedure described in the text. The plots are normalised to unity.*

The acceptance factors before the procedure and after each iteration are shown in Table 6.3, the corresponding fit results in Table 6.4. The values for the S-wave fraction and the corresponding phase are averaged over the four $m(K^+\pi^-)$ bins. Note that the sFit results in Table 4.8 have been obtained using the acceptance factors of Iteration 4. The acceptance factors of the last iteration have already been shown in Table 4.1.

One can see that the procedure converges quickly and that the fit results do not change significantly even after the first iteration. The S-wave parameters remain almost constant, whereas the P-wave amplitudes change by a large amount.

The most important check, of course, is to examine the pion and kaon momentum distributions after the last iteration and *before* the final residual momentum reweighting. From Fig. 6.4 one can see that the agreement in the pion momentum has much improved by applying the method described above. The difference in the kaon momentum has slightly increased but overall has not much changed. In summary, most of the discrepancies can be explained by physical differences between data and simulation.

The method described above is intended to reduce the discrepancies due to physical differences. The remaining difference originates from an insufficient detector description in the simulation. This procedure can be tested mimicking a difference in two event samples by splitting the simulated sample in two and modifying one of them. For this sub-sample the pion momentum is distorted such that it looks like in data. Note that this procedure does also affect the kaon momentum due to the high correlation. Both the sub-sample and the remaining events of the simulation are then used to perform the same iterative method as described above. If the procedure works correctly, the S-wave fraction after the last iteration is expected to be compatible with zero since the simulation does not contain any S-wave contribution.

To artificially distort the pion momentum spectrum in one sub-sample such that it resembles that in data, each event of the simulation is reweighted with $\frac{p(\pi)}{10+p(\pi)}$, where

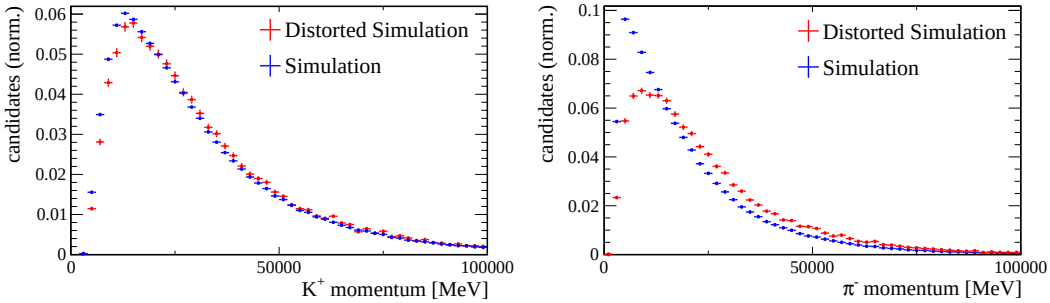

Figure 6.5: *Comparison between simulation and distorted simulation as described in the text. The plots are normalised to unity.*

$p(\pi)$ is the pion momentum in GeV. The distorted spectra can be seen in Fig. 6.5. One can see that the pion momentum distribution is similar to that in Fig. 6.2, the kaon momentum is only slightly affected. An initial fit to the distorted simulation sample yields an S-wave fraction of $F_{\mathrm{S}} = 0.017 \pm 0.001$. The fit is performed in one $K^+\pi^-$ mass bin only. After the first iteration of the above method this is reduced to only $F_{\mathrm{S}} = 0.001 \pm 0.0003$ and after the second iteration it is fully compatible with zero. The P-wave values are compatible with those used for the generation of the simulation within two standard deviations. The differences in the momentum spectra remain.
The conclusion so far is two-fold: Firstly, the test just described shows that the iterative method can distinguish between physics and detector geometry effects. The distortion mimics a detector effect that is also present after the procedure has converged. These detector effects cannot be reduced by this method. Secondly, the true (vanishing) S-wave fraction of the simulated sample is retrieved. Combined with the converging results of Table 6.4 this confirms the stability of the method.
The remaining difference after the final iteration and residual reweighting compared to the fit results before the procedure (i.e. the difference between the first and the last column in Table 6.4) is taken as systematic error due to discrepancies between data and simulation. As shown in the next section, these remaining differences can partially be explained by a different detector description in the simulation. As these differences cannot be easily eliminated by additional selection criteria or reweighting, they are included as the systematic error described above. The systematic errors are discussed in more detail in Ch. 8.

6.3 Pion momentum difference: Detector effects

It can be seen from Fig. 6.4 that even after iteratively reweighting the simulation to remove physical differences there are still discrepancies in the pion momentum and due to the high correlation also in the kaon momentum spectrum. To investigate

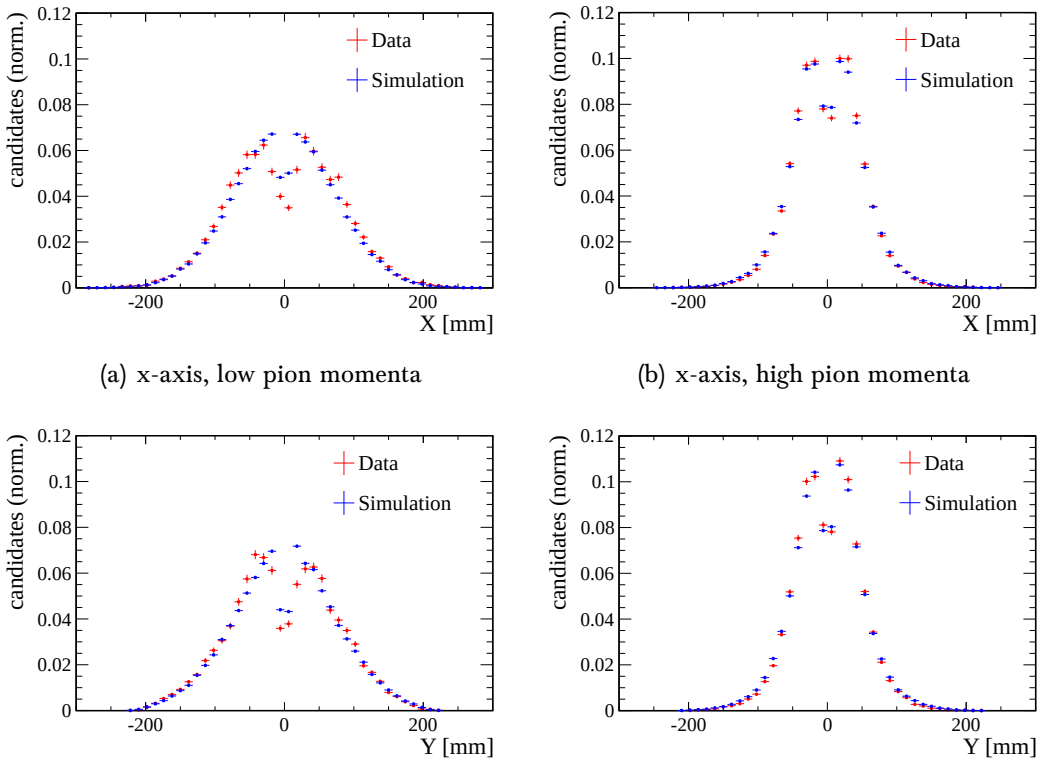

(a) x-axis, low pion momenta

(b) x-axis, high pion momenta

(c) y-axis, low pion momenta

(d) y-axis, high pion momenta

Figure 6.6: *x- and y-positions of the pion tracks at the end of the VELO detector for pion momenta smaller (left side) and larger (right side) than 12 GeV. The plots are normalised to unity.*

possible differences from the detector description in data and simulation the position of the pion tracks (i.e. the x- and the y-coordinate) at the end of the VELO detector is plotted. This is at 770 mm on the z-axis. As the problem mainly occurs at low pion momenta, the samples are split up in pions with momentum smaller and larger than 12 GeV. The distributions can be seen in Fig. 6.6. Two observations can be made: Firstly, the discrepancy between data and simulation is larger and the distribution is much broader for smaller compared to larger pion momenta. It can be seen that in the simulation low momentum pion tracks are more centrally located than those in data. This could explain the discrepancy between data and simulation: As low momentum tracks are more likely to be bent out of the detector acceptance and as these tracks are further away from the beam axis in data, this could account for the excess of low momentum pions in the simulation as observed in Fig. 6.2. Secondly, the disagreement is less pronounced in the y-direction. The discrepancy in the pion momentum might thus be linked to a slightly different geometry description in data and simulation. For kaons and muons, the differences

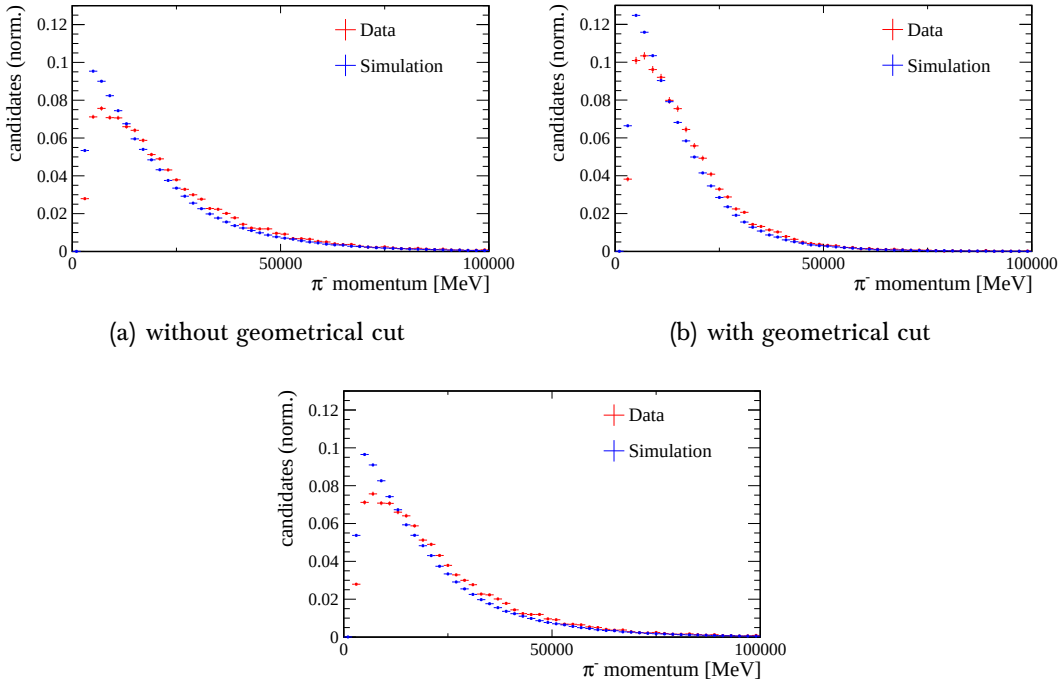

(a) without geometrical cut

(b) with geometrical cut

(c) with additional reweighting

Figure 6.7: *Pion momentum distributions for data and simulation with and without an additional geometrical cut and with additional reweighting. The plots are normalised to unity.*

are very small and can be neglected.
In principle, selection requirements on the position of pion tracks in the VELO detector could improve the agreement in the pion momentum. However, as the disagreement is present over the entire x- and y-range (though more pronounced in the inner region), these criteria will either be not efficient enough or exclude a large fraction of the event samples. In Fig. 6.7(a) and Fig. 6.7(b) the pion momentum distributions without any additional requirement and using only pion tracks that have x-coordinates at the end of the VELO of larger than 40 mm (for data and simulation) are shown. There is only a small improvement if at all and a large fraction of data events are removed from the sample (more than half of it). The entire distribution is shifted to smaller momenta. Another possibility would be to further reweight the simulated pion momentum distribution. This could be done with the distributions in Fig. 6.6. However, reweighting the simulated pion momentum distribution simultaneously with the ratio of the two different distributions in Fig. 6.6(a) and Fig. 6.6(c) does not change the spectra significantly as shown in Fig. 6.7(c). One can conclude that the applied selection cuts and the further reweighting procedure as explained in this section does not improve the agreement between data and simulation. All

studies performed have not revealed a direct link between the detector effects and the pion momentum discrepancy. The only way to account for these possible detector effects and the remaining difference between data and simulation is to assign a systematic error.

6.4 Summary

In this chapter the differences in the kinematic distributions of data and simulation have been investigated. A discrepancy in the pseudorapidity and the transverse momentum of the B^0 meson are taken into account by reweighting the simulation according to Eq. 6.1. This changes the fit results only slightly. The largest difference is observed in the pion momentum, especially for low values. Also the kaon momentum is affected but to a lesser extent. To reduce the physical part of the discrepancy an iterative method is used to effectively mimic a data-like S-wave component in the simulation. This procedure converges quickly and has been tested on simulated events. After the last iteration step, a difference can still be observed but is significantly reduced compared to before. This remaining difference might be linked to different effects of the geometry description in data and simulation. However, neither various additional selection criteria nor further reweighting procedures do change the distributions significantly. Thus, no reason for the observed remaining difference has been found so far.
Therefore, the remaining differences between data and simulation are taken into account by assigning a systematic error. A clear link to detector effects could not be established.

Chapter 7

Additional resonances

Science never solves a problem without creating ten more.

George Bernard Shaw (1856-1950)

Several systematic uncertainties have to be considered for this analysis. They are discussed in detail in the next chapter. In this chapter a source for one specific systematic error is presented, namely the effect of additional $K^+\pi^-$ resonances on the fit results. After a motivation why this effect is studied, it is shown which resonances have to be taken into account. The systematic uncertainty arising from neglecting these resonances is estimated using pseudo-experiments.

7.1 Distribution of the S-wave fractions

As detailed in Ch. 4, the S-wave fractions are determined in four different bins of the $K^+\pi^-$ mass. The results of the nominal fit are summarised in Table 4.8. For

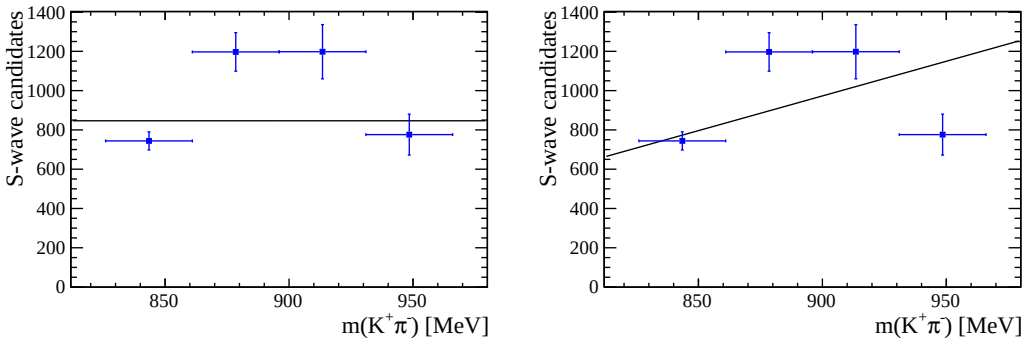

Figure 7.1: *S-wave yield in the four $K^+\pi^-$ mass bins, indicating the statistical error only. A zeroth and first order polynomial is fitted to the data points, respectively.*

the purpose of this chapter, these fractions are converted into an S-wave yield by multiplying the fitted S-wave fraction by the number of signal candidates in that bin. Assuming only a non-resonant contribution, the S-wave yield is expected to follow a flat or linear rising distribution. Figure 7.1, however, shows that this is not the case. Instead a clear increase in the inner bins is visible. Note that only the statistical error is indicated. The two fit curves are discussed later in this section.
The differential decay rate shown in Eq. 1.22 does not explicitly depend on the $K^+\pi^-$ invariant mass although the S-wave amplitude varies with it. To take into account this mass dependency, the nominal fit is performed in four bins of $m(K^+\pi^-)$ and the coupling factors between the S-wave and P-wave contributions are used in the fit. As will be seen in the next chapter, the impact of these factors on the physics parameters is small as they are close to 1 (see Table 1.4). However, an explicit model of the full $K^+\pi^-$ mass spectrum is not assumed for this analysis. Furthermore, only contributions from the $K^*(892)$ P-wave (here, the 0 is dropped for all K^* resonances) and the non-resonant S-wave component are taken into account by modelling the angular distributions, neglecting additional $K^+\pi^-$ resonances, e.g. D-wave states, corresponding to a total spin of $J = 2$ that might be present in the selected mass range (826 to 966 MeV). Although these resonances have a much higher mass than the $K^*(892)$ and their amplitude squared is small in the selected $K^+\pi^-$ mass range, interference effects can have a large impact. This is especially the case for the D-wave resonance $K_2^*(1430)$[76] as it is the only significant contribution with $J > 1$.
Possible explanations of the observed peaking structure are detailed in the following.

To quantify the deviation of the distribution in Fig. 7.1 from the naïve expectation a zeroth and first order polynomial has been fitted to the data points. The fit quality, χ^2/nDoF, is $25/3$ and $21/2$, respectively. These are significant deviations from the expectations and cannot be easily explained by a statistical effect although a downwards fluctuation by two standard deviations of the two inner data points would result in a flat distribution. The most obvious explanation for the peaking structure is another background component in data that is not flat in the $K^+\pi^-$ mass. However, as the background has been investigated in great detail in Ch. 5 and no source has been identified, this is ruled out.
Figure 7.1 only includes the statistical error. In the next chapter, the different systematic uncertainties will be determined, also for the S-wave parameters in each bin. As possible correlations between the four bins and between the amplitude and the corresponding phase are not taken into account in the systematic error determination, they are rather conservatively estimated. Consequently, only the statistical errors are indicated here. While including also the systematic uncertainties would improve the compatibility with a straight line, the peaking structure would, of course, not vanish.

As the angular acceptance is assumed to be independent of the $K^+\pi^-$ invariant mass, the analysis has been performed using a single histogram to describe the

Parameter	Default results	Four acceptance histogram
$R_{\parallel}$	0.227 ± 0.004	0.229 ± 0.004
$R_{\perp}$	0.201 ± 0.004	0.204 ± 0.004
$\delta_{\parallel}$	-2.94 ± 0.02	-2.98 ± 0.02
$\delta_{\perp}$	2.94 ± 0.02	2.92 ± 0.02
$F_{\mathrm{S}}^{(1)}$	0.115 ± 0.007	0.106 ± 0.007
$\delta_{\mathrm{S}}^{(1)}$	3.09 ± 0.10	3.08 ± 0.10
$F_{\mathrm{S}}^{(2)}$	0.049 ± 0.004	0.036 ± 0.004
$\delta_{\mathrm{S}}^{(2)}$	2.66 ± 0.06	2.58 ± 0.06
$F_{\mathrm{S}}^{(3)}$	0.052 ± 0.006	0.045 ± 0.006
$\delta_{\mathrm{S}}^{(3)}$	1.94 ± 0.03	1.77 ± 0.03
$F_{\mathrm{S}}^{(4)}$	0.105 ± 0.014	0.106 ± 0.014
$\delta_{\mathrm{S}}^{(4)}$	1.53 ± 0.03	1.36 ± 0.03

Table 7.1: *Fit results for one and four acceptance histograms. Only the statistical error is indicated.*

angular acceptance. However, an investigation is needed to verify this assumption. The results with one and four acceptance histograms are compared in Table 7.1. The corresponding yield plot can be seen in Fig. 7.2, indicating statistical errors only.

At a first glance, the difference between the two sets of fit results and the two yield distributions is large and the corresponding yield plot shows a different structure. However, several issues have to be taken into account. Firstly, except for the S-wave

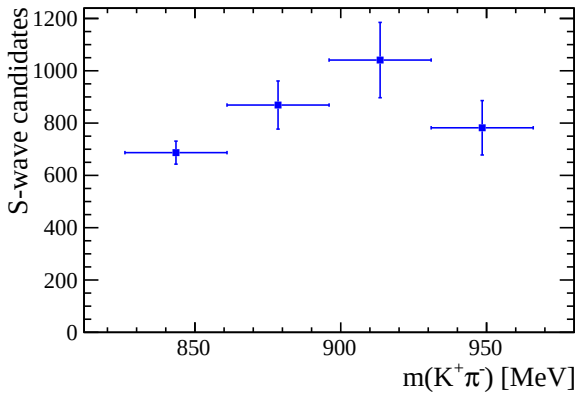

Figure 7.2: *The S-wave yield is shown for the case of four different acceptance histograms, depending on the $K^+\pi^-$ mass bin.*

phase in the third and fourth bin the results are compatible within two standard deviations. Secondly, it has to be noted that the four acceptance histograms have been obtained using a statistically limited simulated event sample. The first bin for example has only approximately one tenth of the total number of candidates. This largely increases the statistical uncertainty of the acceptance and consequently the systematic error due to the limited statistics of the simulated sample. Finally, compared to the nominal yield plot with only one acceptance histogram, only the S-wave yield in the second bin is lower by approximately one standard deviation. As the difference between the two approaches is likely to be of a statistical nature, only one acceptance histogram is used for the default analysis because it reduces the statistical error of the acceptance compared to using four histograms. The cor-

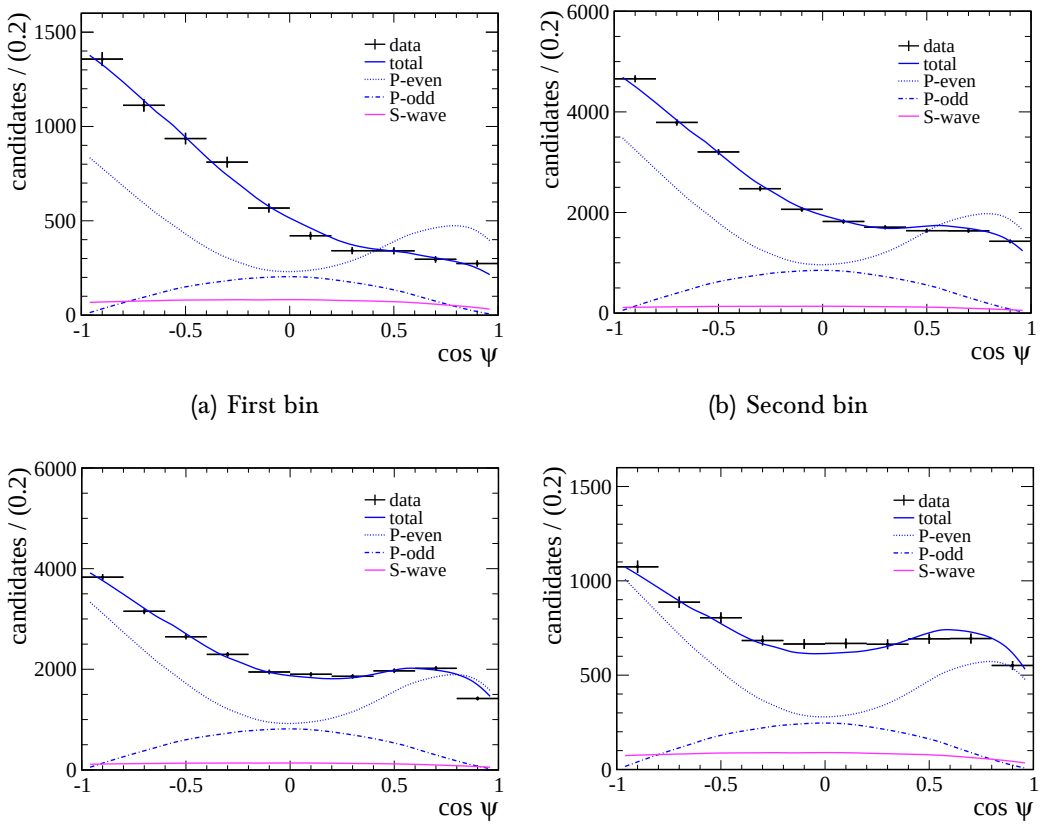

(a) First bin

(b) Second bin

(c) Third bin

(d) Fourth bin

Figure 7.3: *Projection plots of the transversity angle* $\cos\psi$ *in the four mass bins (points with statistical error bars). The plots show the P-wave parity-even (dotted blue) and parity-odd (dashed blue) components, the pure S-wave (purple) contribution without interference terms and the total signal component (solid blue).*

responding acceptance factors for one histogram are listed in Table 4.1.

As a further crosscheck the fit projection plots showing the P- and S-wave components for the four mass bins have been investigated. The most interesting plots because directly related to the S-wave contribution are the projections onto $\cos\psi$ (this angle describes the $K^+\pi^-$ system) that can be seen in Fig. 7.3. The total fitted projections agree well with the data points. In addition, the P-wave shape is constant over the four bins. This is expected as the P-wave amplitudes are defined with respect to the total P-wave fraction. However, the P-even contribution is above the data points in the first and second bin for large positive values of $\cos\psi$. This is the case because interference terms between P- and S-wave lead to a smaller total amplitude. These interference terms can be negative depending on $\cos\psi$. The interference effect decreases with rising $K^+\pi^-$ mass. In a qualitative approach this can be understood in the following way: Integrating over θ and φ to calculate the projection onto $\cos\psi$ yields for the tenth term in Table 1.3

$$h_{10} \cdot f_{10} \propto -|A_0||A_S| \cos(\delta_S) \cdot \cos\psi. \tag{7.1}$$

This is by far the largest contribution to the interference between S-wave and P-wave because $|A_0|$ is the largest amplitude and the term above has to be weighted with the corresponding acceptance factor $\xi_{10} = -0.2292$. The weights ξ_8 and ξ_9 are almost negligible. Keeping in mind that the average $\cos(\delta_S)$ is negative, the term above is negative for $\cos\psi$ larger than zero and positive for values smaller than zero. In addition, the quantity $\cos(\delta_S)$ is close to -1 in the first $K^+\pi^-$ mass bin and approximately 0 in the last bin. This dependence explains that the effect of the interference decreases from bin to bin. This behaviour in addition to the fact that the acceptance in $\cos\psi$ decreases steeply towards large positive values has prompted the concern that this region might be badly treated in the fit. To rule out that this region is responsible for the observed S-wave yield shape, the fit has been repeated for values of $\cos\psi < 0.8$ but this does not significantly change the shape of the S-wave yield. Hence, this is not the reason for the peaking structure.

In summary, several tests have been performed trying to explain the peaking structure in the distribution of the S-wave yield. None of these cross-checks have prompted an explanation. Another possibility left are further $K^+\pi^-$ resonances that are not taken into account by the fitting procedure. This is discussed in more detail in the following section.

7.2 Effect of other resonances

In the context of the analysis of $\overline{B}^0 \to \psi(2S)K^-\pi^+$ decays, possible $K^+\pi^-$ resonances in the relevant mass range for $B^0 \to J/\psi K^+\pi^-$ decays are discussed in [76]. In addition to the $K^*(892)$ contribution, several resonances are known to decay to a

kaon and a pion. The lightest resonance is the $\kappa(800)$ which centers at around 680 MeV and has a very broad width of approximately 550 MeV, thus leaking into the selected $K^+\pi^-$ mass range of this analysis. Considering that the particle is in an S-wave state (total spin $J = 0$), it might mimic a non-resonant $K\pi$ contribution and affect the measured S-wave fractions. Another S-wave component, the $K_0^*(1430)$ meson, has a mass of approximately 1425 MeV and a width of roughly 300 MeV. A particle with similar properties but a total spin of 1 (P-wave), the $K^*(1410)$, has also to be considered in the relevant mass range. Of particular interest is the D-wave state $K_2^*(1430)$. It has a relatively narrow width of roughly 100 MeV but can interfere with the P-wave. These interferences might have a high impact on the physics parameters determined in the fit. Furthermore, there is a P-wave state with a very large width of approximately 300 MeV, the $K^*(1680)$ meson. Moreover, three resonances with a width of approximately 200 MeV are present although their effect on the observables is expected to be small due to their high masses: an S-wave resonance, the $K_0^*(1950)$, an F-wave state ($J = 3$), the $K_3^*(1780)$, and the $K_4^*(2045)$ meson, a G-wave resonance ($J = 4$). The kinematic limit for $B^0 \to J/\psi K^+\pi^-$ decays is at 2183 MeV, thus heavier resonances do not have to be considered. A summary including the measured fractions of the resonant contributions can be found in Table 7.2. The different contributions and the full mass distribution from data are viusalised in Fig. 7.4. It can be seen that in the mass range selected for this analysis (826 to 966

Resonance	Spin state	Mass [MeV]	Width [MeV]	BR [%]	Fraction [76]
$\kappa(800)$	S-wave	682 ± 29	547 ± 24	~ 100	0.032 ± 0.004
$K^*(892)$	P-wave	895.9 ± 0.2	48.7 ± 0.7	~ 100	$\mathbf{0.676 \pm 0.004}$
$K^*(1410)$	P-wave	1414 ± 15	232 ± 21	6.6 ± 1.3	0.003 ± 0.001
$K_0^*(1430)$	S-wave	1425 ± 50	270 ± 80	93 ± 10	0.097 ± 0.005
$K_2^*(1430)$	D-wave	1432 ± 1	109 ± 5	49.9 ± 1.2	$\mathbf{0.082 \pm 0.002}$
$K^*(1680)$	P-wave	1717 ± 27	322 ± 110	38.7 ± 2.5	0.008 ± 0.001
$K_3^*(1780)$	F-wave	1776 ± 7	159 ± 21	18.8 ± 1.0	0.006 ± 0.001
$K_0^*(1950)$	S-wave	1945 ± 22	201 ± 78	52 ± 14	0.008 ± 0.001
$K_4^*(2045)$	G-wave	2045 ± 9	198 ± 30	9.9 ± 1.2	0.004 ± 0.001
non-resonant	S-wave				0.021 ± 0.003
Total S-wave	S-wave				$\mathbf{0.195 \pm 0.011}$

Table 7.2: *Summary of the resonances present in the selected $K^+\pi^-$ mass range [5, 76]. Note that the existence of the $\kappa(800)$ is still disputed. BR denotes the branching fraction for the decay of the resonance to a kaon and a pion. The last column shows the fitted fractions from [76] in the $K^+\pi^-$ mass range up to 2183 MeV. The important components are in bold.*

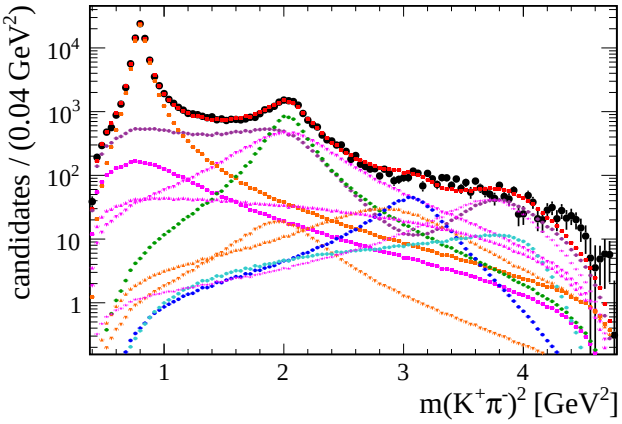

Figure 7.4: *The plot shows the projection of the data distribution of $B^0 \to J/\psi K^+\pi^-$ candidates (black points) onto the $m(K^+\pi^-)^2$ axis as well as the fitted resonant and non-resonant contributions: The S-wave components are shown in magenta (the sum in purple), the P-wave components in orange (note the dominant peak from the $K^*(892)$ resonance), the D-wave contribution in green, the F-wave distribution in blue and the G-wave contribution in cyan. The sum of all fitted contributions is visualised in red. Note that the x-axis is quadratic and the y-axis logarithmic. More details are given in the text. Figure courtesy of T. Skwarnicki [76].*

MeV) the $K^*(892)$ resonance is the dominant contribution (orange peaking structure), followed by various S-wave components (magenta, total distribution in purple).

The fractions quoted in Table 7.2 and the mass plot have been obtained from a fit to data recorded by the LHCb detector in 2011, as documented in [76]. This is done by using a so-called amplitude fit where the total decay amplitude is obtained by summing over all terms that represent the individual $K^+\pi^-$ resonances. For the decay amplitudes the helicity framework (see Subsec. 1.4.2) is used. To each resonance a set of complex decay amplitudes can be associated. For spinless resonances, only one helicity amplitude has to be considered, for all other contributions there are three complex amplitudes. The decay matrix element does then depend on the amplitudes, the shape of the resonance and implicitly the momenta of the final states particles. Interference effects are taken into account by summing over the different resonances linearly and then calculating the magnitude of the total decay amplitude. The $K^+\pi^-$ mass dependence is mainly described by a Breit-Wigner distribution. In the fit the masses and widths of the resonances are generally fixed to the world average values. In a simplified approach the decay matrix element can be schematically written in the form $\mathcal{M} = \sum_\lambda \left| \sum_k A_{k,\lambda}\, R_k\, d_\lambda^{J_k} \right|^2$, where k indicates the resonance, λ is the helicity of the J/ψ (and the K^*), A the complex helicity amplitude, R the

$m(K^+\pi^-)$ [MeV]	candidates, S- and P-wave	candidates, additional resonances
$826 - 861$	26 406	23 957
$861 - 896$	105 287	96 285
$896 - 931$	100 288	90 495
$931 - 966$	32 429	29 429

Table 7.3: *Selected candidates in the four mass bins for both sets of pseudo-experiments.*

shape of the resonance and $d_\lambda^{J_k}$ depends mainly on the spin of the resonance J_k. Note that this formula only serves as an illustration and does not show the full form of the decay matrix element used in the fit. Both the fractions and mass shapes of the individual contributions shown here do not include interference effects, whereas the total contribution does. Hence, the individual contributions do not need to add up to the full distribution.
This model, also called isobar model, is then used to generate two sets of pseudo-experiments, each containing 400 000 $B^0 \to J/\psi K^+\pi^-$ events in the full mass

Parameter	S- and P-wave	Including other resonances	Difference
$R_\parallel$	0.21947 ± 0.00185	0.22485 ± 0.00195	0.005
$R_\perp$	0.21739 ± 0.00187	0.21345 ± 0.00198	0.004
$\delta_\parallel$	-2.9335 ± 0.0122	-2.9320 ± 0.0124	0.00
$\delta_\perp$	2.9687 ± 0.0086	2.9773 ± 0.0090	0.01
$F_\mathrm{S}^{(1)}$	0.10857 ± 0.00347	0.09254 ± 0.00317	0.016
$\delta_\mathrm{S}^{(1)}$	3.3852 ± 0.0418	3.3236 ± 0.0539	0.06
$F_\mathrm{S}^{(2)}$	0.02940 ± 0.00108	0.02695 ± 0.00115	0.002
$\delta_\mathrm{S}^{(2)}$	2.8606 ± 0.0432	2.8358 ± 0.0487	0.02
$F_\mathrm{S}^{(3)}$	0.03536 ± 0.00263	0.04113 ± 0.00299	0.006
$\delta_\mathrm{S}^{(3)}$	1.8247 ± 0.0150	1.8475 ± 0.0151	0.02
$F_\mathrm{S}^{(4)}$	0.12290 ± 0.00730	0.12291 ± 0.00777	0.000
$\delta_\mathrm{S}^{(4)}$	1.4319 ± 0.0126	1.5115 ± 0.0127	0.08

Table 7.4: *Fit results using two sets of pseudo-experiments, one containing only the P- and S-wave contributions, the other also including other resonances. Errors larger than half of the statistical uncertainty are highlighted in red.*

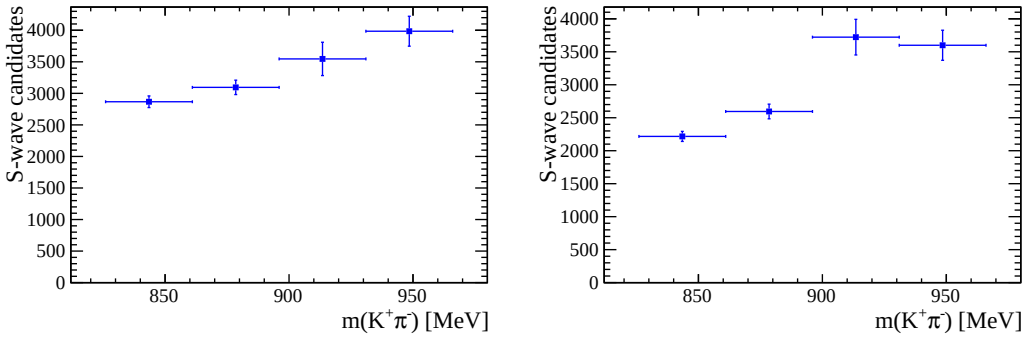

(a) Only the P- and S-wave contributions (b) Including additional resonances

Figure 7.5: *The S-wave yield is shown for two sets of pseudo-experiments, containing (a) only the P- and S-wave contributions and (b) also other resonances. Only the statistical errors are indicated.*

range of Fig. 7.4, i.e. up to 2183 MeV [76] (note that in the figure the mass squared is shown on the x-axis). Both samples contain the four-momenta of the final state particles, from which the transversity angles and the masses of the B^0, the J/ψ and the $K^*(892)$ meson can be calculated. The maximum likelihood fit described in Ch. 4 is then performed, not including efficiency and resolution effects. One of these samples considers only the S- and P-wave contributions (i.e. $J = 0, 1$), the other one all components listed in Table 7.2. The comparison of the two fit results for the two different samples allows to study the effect of higher spin resonances on the physics parameters.

The only prominent contribution with a spin J larger than 1 is the $K_2^*(1430)$ resonance which is a $J = 2$ state. Thus, this is the main difference between the two samples of pseudo-experiments. In the maximum-likelihood fit the angular distributions of the P- and S-wave components are accounted for, whereas states of higher spin are neglected. Figure 7.4 indicates that the D-wave contribution is small in the narrow region considered in this analysis. This, however, is only true for the squared amplitudes alone but not necessarily true for the interference with the $K^*(892)$. As this resonance is so prominent, a large enhancement is possible. The impact of this effect on the polarisation amplitudes can be studied by the two samples.

The number of candidates selected in each $K^+\pi^-$ mass bin is listed in Table 7.3. The results from the fits to the two pseudo-experiments are summarised in Table 7.4. It can be seen immediately that there are large discrepancies between the two sets of results, the largest difference being observed for $F_{\mathrm{S}}^{(1)}$. The corresponding S-wave yield plots are shown in Fig. 7.5. The plot for which only P- and S-wave contributions are considered shows the naïvely expected shape of the S-wave yield, i.e. a rising line. When including all other resonances, however, the plot changes. It is clearly visible that the S-wave yield in the third $K^+\pi^-$ mass bin moves upwards, indicating

a peaking structure. The difference between the two yield distributions can also be attributed to a statistical effect if one considers the third bin an upward fluctuation. On the contrary, the results summarised in Table 7.4 show that including other resonances can also affect the P-wave parameters by a significant amount. Thus, the full difference observed between the two sets of pseudo-experiments is taken as a systematic uncertainty. This additional source of systematic errors is dominant only for some of the S-wave parameters. The total systematic uncertainty of the P-wave parameters is almost unchanged. All systematic effects are discussed in Ch. 8.

7.3 Summary

In this chapter the effect of additional $K^+\pi^-$ resonances other than the $K^*(892)$ in the decay $B^0 \to J/\psi K^+\pi^-$ on the physics parameters has been investigated. The study has been triggered by the distribution of the S-wave yield in the four $K^+\pi^-$ mass bins. In principle, one would expect a flat or linearly rising behaviour. However, a peaking structure is observed. The most obvious explanation would be additional background components that have not been accounted for in the fitting procedure. Therefore, numerous background sources, like the misreconstructed background component and contributions from other decay channels (e.g. $B_s^0 \to J/\psi\eta'$, $B_s^0 \to J/\psi\phi$), have been re-investigated but no evidence has been found that would explain the observed yield distribution. Using separate acceptance histograms for each bin does change the S-wave yields, these effects, however, can be explained by statistical effects. Critical regions for large positive values of $\cos\psi$ have been excluded from the fit but no significant deviations have been found.
Furthermore, additional $K^+\pi^-$ resonances have been investigated. The PDF used in the fit does only include the angular distributions of the P- and S-wave contributions and it does not make any explicit assumption on the mass shape of these components (except in the determination of the coupling factors between S-wave and P-wave). Several other K^* resonances can affect the measurement of the polarisation amplitudes. Of particular interest is the D-wave state $K_2^*(1430)$. D-waves ($J = 2$) are not considered in the fitting procedure and can have an effect on the observables due to interference with P-wave states. Using pseudo-experiments it has been shown that such effects can modify the shape of the S-wave yield distribution and the extraction of the P-wave observables. Consequently, a systematic error has been assigned to account for this behaviour. This, of course, is a very conservative approach because the shape of the S-wave yield could also be explained by a statistical fluctuation.
Future analyses have to take into account these resonances explicitly. One way would be to include D-wave terms into the PDF. Another approach would be to take into account the dependency on the $K^+\pi^-$ mass explicitly, considering all resonant and non-resonant contributions. The problem of this method is that theoretically no full description is currently available.

Chapter 8

Systematic uncertainties

Errors are not in the art but in the artificers.
Sir Isaac Newton (1642-1727)

This chapter is dedicated to the study of sources for systematic uncertainties. In previous chapters, the most important contributions have already been mentioned. These are the background treatment, the misreconstructed background component and the differences between data and simulation. In addition, the uncertainty of the B^0 mass model, the statistical error on the acceptance, the coupling between S- and P-wave and further $K^+\pi^-$ resonances are taken into account. Further resonances have been investigated in the previous chapter. Here, the corresponding systematic errors are again listed in comparison with the other uncertainties. In general, the tables in this chapter contain two sets of fit results. These are the default results and the numbers obtained when changing the fit model to obtain the systematic error. The full difference between the two sets is taken as systematic uncertainty that is listed in the last column of the table. The number is highlighted in red if it is larger than half of the statistical error. The default fit is the sFit as detailed in Ch. 4 and its results are summarised in Table 4.8. It uses the sum of two Gaussian functions as mass parametrisation, does not include misreconstructed background and takes into account the acceptance factors from Table 4.1.

8.1 Mass model

In the default fit, an initial mass fit is performed in each $K^+\pi^-$ mass bin, assuming that the B^0 mass distribution can be described by the sum of two Gaussian functions. Subsequently, signal weights are calculated to separate signal and background, followed by a maximum likelihood fit to the remaining signal candidates to extract the physics parameters. Therefore, the correct choice of the mass model is essential for the determination of the observables. To estimate the effect of a different mass model on the fit results, a single Gaussian function is used instead to describe the invariant mass distribution of the B^0 meson. In Table 8.1 the nominal results are

Parameter	Default result (sFit)	sFit with altern. mass model	Abs. Difference
$R_{\parallel}$	0.22747 ± 0.00387	0.22795 ± 0.00393	0.000
$R_{\perp}$	0.20117 ± 0.00387	0.20024 ± 0.00393	0.001
$\delta_{\parallel}$	-2.9372 ± 0.0240	-2.9343 ± 0.0240	0.00
$\delta_{\perp}$	2.9428 ± 0.0180	2.9402 ± 0.0183	0.00
$F_{\mathrm{S}}^{(1)}$	0.11529 ± 0.00675	0.11997 ± 0.00714	0.005
$\delta_{\mathrm{S}}^{(1)}$	3.0930 ± 0.1010	3.0830 ± 0.1040	0.01
$F_{\mathrm{S}}^{(2)}$	0.04945 ± 0.00398	0.05102 ± 0.00414	0.001
$\delta_{\mathrm{S}}^{(2)}$	2.6566 ± 0.0617	2.6468 ± 0.0613	0.01
$F_{\mathrm{S}}^{(3)}$	0.05171 ± 0.00631	0.05509 ± 0.00667	0.003
$\delta_{\mathrm{S}}^{(3)}$	1.9397 ± 0.0301	1.9465 ± 0.0296	0.01
$F_{\mathrm{S}}^{(4)}$	0.10530 ± 0.01410	0.10930 ± 0.01440	0.004
$\delta_{\mathrm{S}}^{(4)}$	1.5254 ± 0.0287	1.5318 ± 0.0284	0.01

Table 8.1: *Fit results of the nominal fit (sum of two Gaussian functions) compared to those using only a single Gaussian function to model the B^0 mass, showing statistical errors only. Using a Crystal Ball function gives equivalent results.*

compared with those using the alternative mass model. The differences are rather small. They are negligible for the P-wave amplitudes, the largest effect can be observed for $F_{\mathrm{S}}^{(1)}$. The full difference quoted in the table is taken as systematic error. Equivalent results have been obtained using a Crystal Ball function [64] to model the B^0 mass. In conclusion, the physics parameters do not depend on the mass model to a large extent.

8.2 Background treatment

The two fitting techniques, the classical fit using an explicit background model and the sFit, where the background is separated before the extraction of the physics parameters, are used to estimate the systematic uncertainty from the background treatment. The difference between the cFit and sFit results is taken as systematic error. This also serves as a test how accurately the sFit method can separate signal from background. The corresponding results are summarised in Table 8.2. Again, the differences are rather small, showing that both fit methods are fully compatible. Note in particular that the statistical errors are in good agreement. The largest effect is observed for $R_{\parallel}$ and $\delta_{\mathrm{S}}^{(4)}$.

Parameter	Default result (sFit)	cFit result	Abs. Difference
$R_{\parallel}$	0.22747 ± 0.00387	0.22925 ± 0.00401	0.002
$R_{\perp}$	0.20117 ± 0.00387	0.20003 ± 0.00400	0.001
$\delta_{\parallel}$	-2.9372 ± 0.0240	-2.9399 ± 0.0246	0.00
$\delta_{\perp}$	2.9428 ± 0.0180	2.9383 ± 0.0186	0.00
$F_{\mathrm{S}}^{(1)}$	0.11529 ± 0.00675	0.11234 ± 0.00725	0.003
$\delta_{\mathrm{S}}^{(1)}$	3.0930 ± 0.1010	3.1310 ± 0.1070	0.04
$F_{\mathrm{S}}^{(2)}$	0.04945 ± 0.00398	0.04822 ± 0.00398	0.001
$\delta_{\mathrm{S}}^{(2)}$	2.6566 ± 0.0617	2.6578 ± 0.0633	0.00
$F_{\mathrm{S}}^{(3)}$	0.05171 ± 0.00631	0.05143 ± 0.00645	0.000
$\delta_{\mathrm{S}}^{(3)}$	1.9397 ± 0.0301	1.9358 ± 0.0307	0.01
$F_{\mathrm{S}}^{(4)}$	0.10530 ± 0.01410	0.10230 ± 0.01450	0.003
$\delta_{\mathrm{S}}^{(4)}$	1.5254 ± 0.0287	1.5032 ± 0.0307	0.02

Table 8.2: *Fit results of the default fit (sFit) compared to those of the cFit.*

8.3 Misresonstructed background

In Ch. 5 it has been shown that the only background component that has to be taken into account in the fit is the contribution from misreconstructed background (in most of the cases wrongly reconstructed pions). Furthermore, it has been explained how the additional background component can be included in the PDF by using simulated events. The mass distribution of this background component is modelled by the sum of two Gaussian functions plus and exponential function. As the implementation is technically easier in the cFit framework than using the sFit technique, the difference between the cFit results with and without the misreconstructed background is taken as systematic uncertainty. The projection plot of the B^0 mass distribution can be seen in Fig. 8.1. It shows the one-dimensional projection of the fitted signal (blue), flat background (red) and misreconstructed background (green) PDF. The sum of these functions (black) is in agreement with the data points. The misreconstructed component can be clearly identified as the small peaking contribution.

In Table 8.3 the nominal cFit results are compared with those including the misreconstructed background. Taking into account this component has a large impact on the physics parameters, especially on the S-wave values. The S-wave fractions increase significantly, the largest rise can be observed for $F_{\mathrm{S}}^{(1)}$. The fraction of this background is fixed to 3.5%, corresponding to the number observed on simulated events. Alternatively, the fraction has been increased to 5%. The results remain

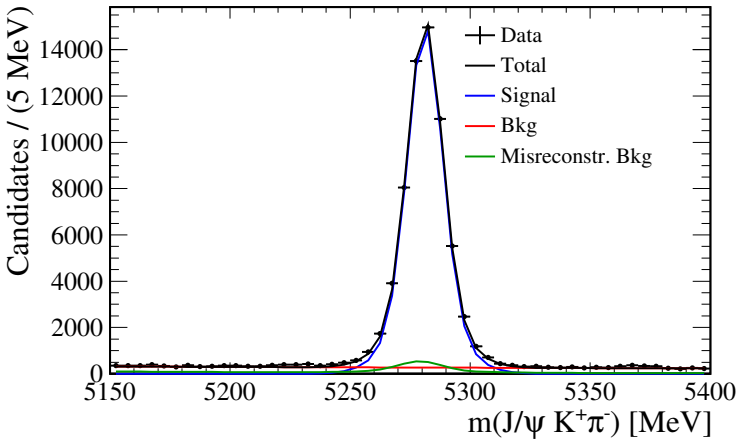

Figure 8.1: *Mass projection plot corresponding to the cFit including the misreconstructed background component. It shows the data points (with statistical error bars), the signal component (blue), the flat background component (red), the misreconstructed background (green) and the sum of all components (black). The plot corresponds to an average distribution over the four $K^+\pi^-$ mass bins.*

unchanged as well as when using only misreconstructed background candidates to model this background shape where the angular distributions are different from the signal distributions. Note that only 40% of the misreconstructed background events have angular distributions significantly different from those for signal candidates.
It can be debated whether the fit including the misreconstructed background should be taken as default. This strategy is not chosen so that the PDF is as simple as possible. The treatment of this background component would have to be included as a systematic uncertainty (although possibly smaller) in any case. Furthermore, this systematic error is not the dominant contribution to the total uncertainty.
This systematic error is obtained using the cFit technique as it is simpler to include an additional background component than in the sFit which is performed on a background subtracted sample and where the angular distributions of the background are not modelled explicitly.

8.4 Angular acceptance

In Ch. 6 the kinematic distributions of data and simulation have been compared and discrepancies have been discussed. To decrease the large discrepancy in the pion momentum spectrum an iterative method has been presented which effectively introduces an S-wave component to the simulated event sample. The remaining differences cannot be fully explained and are taken into account by a systematic uncertainty. The difference between the fit results before the iterative procedure and

Parameter	cFit result	cFit result with misrec. bkg.	Abs. Difference
$R_{\parallel}$	0.22925 ± 0.00401	0.23108 ± 0.00415	0.002
$R_{\perp}$	0.20003 ± 0.00400	0.20020 ± 0.00414	0.000
$\delta_{\parallel}$	-2.9399 ± 0.0246	-2.9388 ± 0.0251	0.00
$\delta_{\perp}$	2.9383 ± 0.0186	2.9329 ± 0.0192	0.00
$F_{\mathrm{S}}^{(1)}$	0.11234 ± 0.00725	0.11850 ± 0.00775	0.006
$\delta_{\mathrm{S}}^{(1)}$	3.1310 ± 0.1070	3.1260 ± 0.1070	0.01
$F_{\mathrm{S}}^{(2)}$	0.04822 ± 0.00398	0.05035 ± 0.00420	0.002
$\delta_{\mathrm{S}}^{(2)}$	2.6578 ± 0.0633	2.6560 ± 0.0635	0.00
$F_{\mathrm{S}}^{(3)}$	0.05143 ± 0.00645	0.05427 ± 0.00680	0.003
$\delta_{\mathrm{S}}^{(3)}$	1.9358 ± 0.0307	1.9292 ± 0.0305	0.01
$F_{\mathrm{S}}^{(4)}$	0.10230 ± 0.01450	0.10630 ± 0.01510	0.004
$\delta_{\mathrm{S}}^{(4)}$	1.5032 ± 0.0307	1.4910 ± 0.0314	0.01

Table 8.3: *Fit results of the cFit compared to those of the cFit including the misreconstructed background.*

after the final step is taken as systematic error. The corresponding fit results can be seen in Table 8.4.
The difference between the two sets of results is large. It is the dominant systematic uncertainty for the P-wave and most of the S-wave parameters. Future analyses, taking into account more data, will have to find a strategy how to further reduce and fully explain the difference in the pion momentum between data and simulation. Several options would be available: The simulation could be tuned to better describe the observed kinematic distributions and underlying physics processes. A first step on this path would be the generation of simulated events including an S-wave contribution. Although this would not solve the observed discrepancy per se, the iterative acceptance determination could be avoided. Certainly the best way would be to find an acceptance description that does not rely on simulated events but on data only. So far, however, no solution has been found.

8.5 Statistical uncertainty of acceptance correction

The angular acceptance is determined from simulated events. Due to the finite size of the sample, the statistical errors of the acceptance histogram have to be taken into account as a systematic uncertainty of the physics parameters as they are not included in the fit procedure. To estimate this effect, 50 pseudo-experiments have been performed and fitted for while varying the acceptance histogram randomly

Parameter	Default result (sFit)	sFit before iter. procedure	Abs. Difference
$R_{\parallel}$	0.22747 ± 0.00387	0.23616 ± 0.00395	0.009
$R_{\perp}$	0.20117 ± 0.00387	0.20852 ± 0.00394	0.007
$\delta_{\parallel}$	-2.9372 ± 0.0240	-2.9648 ± 0.0241	0.03
$\delta_{\perp}$	2.9428 ± 0.0180	2.9298 ± 0.0184	0.01
$F_{\mathrm{S}}^{(1)}$	0.11529 ± 0.00675	0.10844 ± 0.00675	0.007
$\delta_{\mathrm{S}}^{(1)}$	3.0930 ± 0.1010	3.0860 ± 0.1130	0.01
$F_{\mathrm{S}}^{(2)}$	0.04945 ± 0.00398	0.04523 ± 0.00419	0.004
$\delta_{\mathrm{S}}^{(2)}$	2.6566 ± 0.0617	2.6041 ± 0.0658	0.05
$F_{\mathrm{S}}^{(3)}$	0.05171 ± 0.00631	0.05164 ± 0.00662	0.000
$\delta_{\mathrm{S}}^{(3)}$	1.9397 ± 0.0301	1.8625 ± 0.0280	0.08
$F_{\mathrm{S}}^{(4)}$	0.10530 ± 0.01410	0.10790 ± 0.01450	0.003
$\delta_{\mathrm{S}}^{(4)}$	1.5254 ± 0.0287	1.4698 ± 0.0293	0.05

Table 8.4: *Fit results of the nominal sFit compared to those before the iterative acceptance determination.*

within its statistical error. The fit settings have been the same as for the pseudo-experiments detailed in Sec. 4.4. The distributions of the physics parameters agree with a Gaussian shape as expected and the width of these distributions is taken as systematic error. The corresponding numbers are listed in Table 8.5.
The effect is small compared to the statistical error of the physics parameters. For the S-wave parameters the widths are larger than for the P-wave parameters. A full explanation has not been found, one reason, however, could be that the S-wave fractions and phases are determined in separate bins of the $K^+\pi^-$ mass with a reduced number of signal candidates which might increase the fluctuations.

8.6 Coupling between S- and P-wave

In Subsec. 1.4.4 it has been explained that to account for the $K^+\pi^-$ mass dependence of the polarisation amplitudes correction factors, C_{SP}, are calculated in four mass bins that effectively describe the coupling between S-wave and P-wave. This procedure is model dependent. In this case here, a Breit-Wigner function is used to describe the P-wave line-shape, for the S-wave a flat model has been chosen. In principle, the systematic uncertainties could be estimated by changing the assumption for the line-shapes. However, as the C_{SP} factors are close to unity, an alternative, more conservative, approach is used and the full fit is repeated neglecting the coupling between S-wave and P-wave and the difference to the nominal fit is assigned

Parameter	Spread of fit results
$R_{\parallel}$	0.001
$R_{\perp}$	0.001
$\delta_{\parallel}$	0.01
$\delta_{\perp}$	0.01
$F_{\mathrm{S}}^{(1)}$	0.003
$\delta_{\mathrm{S}}^{(1)}$	0.04
$F_{\mathrm{S}}^{(2)}$	0.002
$\delta_{\mathrm{S}}^{(2)}$	0.03
$F_{\mathrm{S}}^{(3)}$	0.002
$\delta_{\mathrm{S}}^{(3)}$	0.03
$F_{\mathrm{S}}^{(4)}$	0.003
$\delta_{\mathrm{S}}^{(4)}$	0.04

Table 8.5: *Systematic errors due to the statistical uncertainty of the angular acceptance histogram.*

as systematic error. The two sets of fit results and the difference between them can be found in Table 8.6.
The effect on the P-wave parameters and the S-wave phases is negligible. To the contrary, it is one of the dominant contributions to the S-wave fractions of the second and third bin. This can be understood as the C_{SP} factors in these two mass ranges are further away from 1 than in the outer bins. However, these uncertainties are smaller or approximately equal to the statistical errors. It is expected that changing the model of the line-shape instead of neglecting the coupling factors entirely would not significantly decrease the systematic effect.

8.7 Summary

In Table 8.7 all contributions to the systematic errors are summarised and compared to the statistical error of the default maximum likelihood sFit. The results will be discussed in detail in Ch. 9. Note that the coupling between S-wave and P-wave does not affect the P-wave results, hence this contribution is only listed for the S-wave parameters. The effect of further $K^+\pi^-$ resonances has been addressed in the previous chapter, the numbers are listed here to be compared to the other uncertainties. The total systematic error is the quadratic sum of all single contributions.
Most of the parameters are systematically limited, only for $\delta_{\mathrm{S}}^{(1)}$ and $F_{\mathrm{S}}^{(4)}$ the statistical error is larger than the systematic uncertainty. The following statements can be

Parameter	Default result (sFit)	sFit neglecting C_{SP} factors	Abs. Difference
$R_{\parallel}$	0.22747 ± 0.00387	0.22729 ± 0.00385	0.000
$R_{\perp}$	0.20117 ± 0.00387	0.20165 ± 0.00384	0.000
$\delta_{\parallel}$	-2.9372 ± 0.0240	-2.9396 ± 0.0239	0.00
$\delta_{\perp}$	2.9428 ± 0.0180	2.9438 ± 0.0180	0.00
$F_{\mathrm{S}}^{(1)}$	0.11529 ± 0.00675	0.11137 ± 0.00651	0.003
$\delta_{\mathrm{S}}^{(1)}$	3.0930 ± 0.1010	3.0930 ± 0.1010	0.00
$F_{\mathrm{S}}^{(2)}$	0.04945 ± 0.00398	0.04465 ± 0.00366	0.005
$\delta_{\mathrm{S}}^{(2)}$	2.6566 ± 0.0617	2.6480 ± 0.0622	0.01
$F_{\mathrm{S}}^{(3)}$	0.05171 ± 0.00631	0.04717 ± 0.00591	0.005
$\delta_{\mathrm{S}}^{(3)}$	1.9397 ± 0.0301	1.9359 ± 0.0301	0.00
$F_{\mathrm{S}}^{(4)}$	0.10530 ± 0.01410	0.10300 ± 0.01390	0.002
$\delta_{\mathrm{S}}^{(4)}$	1.5254 ± 0.0287	1.5255 ± 0.0285	0.00

Table 8.6: *Fit results of the default sFit compared to those neglecting the coupling between S-wave and P-wave.*

made using the results in Table 8.7 (dominant contributions highlighted in red):

- The P-wave amplitudes are clearly systematically limited, by a factor of 2 to 3 compared to the statistical error. The largest systematic contribution has its origin in the differences between data and simulation. All other sources are almost negligible in the quadratic sum. In consequence, future analyses have to focus on reducing the discrepancy in the pion momentum and other kinematic quantities to an even larger extent.

- For the P-wave phases both the statistical and the systematic errors are approximately equal. The largest contribution here originates as well from the angular acceptance determination.

- The S-wave parameters show a very different behaviour in the four $K^+\pi^-$ mass bins. For the amplitudes one can observe a decreasing weight of the systematic error compared to the statistical uncertainty. In the first bin the systematic error is almost three times as large as the statistical uncertainty, whereas in the last bin it amounts to only approximately 60%. For the S-wave phases, however, the trend is opposite. While in the first bin the systematic uncertainty is smaller than the statistical, in the last bin it is almost four times as large. This behaviour, especially the very large systematic uncertainty on $F_{\mathrm{S}}^{(1)}$, is not fully understood. In this context, it should be noted that the contribution from other resonances largely varies from bin to bin. Thus, subsequent anal-

Source	$R_\perp$	$R_\perp$	$\delta_\parallel$	$\delta_\perp$
Mass model	0.000	0.001	0.00	0.00
Background treatment	0.002	0.001	0.00	0.00
Misreconstructed background	0.002	0.000	0.00	0.01
Angular acceptance	0.009	0.007	0.03	0.01
Statistical uncertainty on acceptance	0.001	0.001	0.01	0.01
Other resonances	0.005	0.004	0.00	0.01
Total systematic uncertainty	0.011	0.008	0.03	0.02
Statistical uncertainty	0.004	0.004	0.02	0.02

	$F_S^{(1)}$	$\delta_S^{(1)}$	$F_S^{(2)}$	$\delta_S^{(2)}$
Mass model	0.005	0.01	0.001	0.01
Background treatment	0.003	0.04	0.001	0.00
Misreconstructed background	0.006	0.01	0.002	0.00
Angular acceptance	0.007	0.01	0.004	0.05
Statistical uncertainty on acceptance	0.003	0.04	0.002	0.03
C_{SP} factors	0.004	0.00	0.005	0.01
Other resonances	0.016	0.06	0.002	0.02
Total systematic uncertainty	0.020	0.08	0.007	0.06
Statistical uncertainty	0.007	0.10	0.004	0.06

	$F_S^{(3)}$	$\delta_S^{(3)}$	$F_S^{(4)}$	$\delta_S^{(4)}$
Mass model	0.003	0.01	0.004	0.01
Background treatment	0.000	0.00	0.003	0.02
Misreconstructed background	0.003	0.01	0.004	0.01
Angular acceptance	0.000	0.08	0.003	0.05
Statistical uncertainty on acceptance	0.002	0.03	0.003	0.04
C_{SP} factors	0.005	0.00	0.002	0.00
Other resonances	0.006	0.02	0.000	0.08
Total systematic uncertainty	0.009	0.09	0.008	0.11
Statistical uncertainty	0.006	0.03	0.014	0.03

Table 8.7: *Summary of all contributions to the systematic uncertainty compared to the statistical error for the default sFit. The contribution from the C_{SP} factors is negligible for the P-wave parameters. The dominant sources are highlighted in red.*

yses have to focus on investigating these resonances in more detail. Another point is the effect of the interference between P- and S-wave that decreases from bin to bin, i.e. the statistical handle on the S-wave parameters changes.

- Furthermore, the dominant source is different from bin to bin and also between amplitude and corresponding phase of the same bin. In the first bin, the largest contribution for the amplitude is from the further $K^+\pi^-$ resonances. An extensive discussion of this source has been detailed in the previous section. For the strong phase the same contribution is the most dominant one. However, significant contributions come as well from the statistical uncertainty on the acceptance and the background treatment.

- The systematic errors in the second mass bin are much smaller. Both the difference between data and simulation and the coupling between S- and P-wave are responsible for the systematic error of the amplitude to a large extent, all others sources are negligible. For the corresponding phase the most important contribution originates from the acceptance determination.

- The same conclusion can be drawn for the strong phase in the third bin, even to a larger extent. For the amplitude the C_{SP} factors and further resonances are the dominant contributions.

- In the fourth bin numerous sources are responsible for the systematic uncertainty of the S-wave amplitude, the largest contributions originating from the mass model and the misreconstructed background. For the corresponding phase further resonances are the largest contribution to the systematic error, followed by the acceptance determination.

Although the size and the main sources of the systematic errors vary significantly between P-wave and S-wave and from bin to bin, it can be concluded that the analysis is systematically dominated to a large extent. First and foremost, this can be attributed to the difference of the observed kinematic distributions between data and simulation. Even the relatively small remaining difference in the pion and kaon momentum spectra translates into a very large uncertainty on the acceptance determination and consequently on the fit results. Once more, this shows the tight connection between the kinematic distributions of the final state particles, the acceptance determination and the measurement of the polarisation amplitudes. The effect is reduced by the effective inclusion of an S-wave component to the simulation but the impact on the P-wave amplitudes remains large. As already mentioned the systematic contributions to the S-wave parameters differ largely in the four bins compared to the statistical error. This can be partially attributed to the bin-dependent contributions from other resonances and the interference terms between S- and P-wave.

Chapter 9

Results of the maximum likelihood fit and search for direct CP violation

---

However beautiful the strategy, you should occasionally look at the results.

Sir Winston Churchill (1874-1965)

In this chapter the results of the maximum likelihood fit and a test of the CP symmetry, fitting B^0 and $\overline{B}^0$ decays separately, is presented. First, the results of the P- and S-wave parameters are summarised and important cross-checks are detailed. In addition, it is explained how the 2-fold ambiguity of the strong phases is resolved. Finally, the results of the separate fits to B^0 and $\overline{B}^0$ decays, which tests direct CP violation, is shown and a short summary is given.

9.1 P-wave results

In this section the results of the P-wave parameters obtained from a fit to the combined $B^0 \to J/\psi K^{*0}$ and $\overline{B}^0 \to J/\psi \overline{K}^{*0}$ data set, assuming no CPV, are discussed.

Parameter	Fit result
$R_\parallel$	$0.227 \pm 0.004 \pm 0.011$
$R_\perp$	$0.201 \pm 0.004 \pm 0.008$
$\delta_\parallel$	$-2.94 \pm 0.02 \pm 0.03$
$\delta_\perp$	$2.94 \pm 0.02 \pm 0.02$

Table 9.1: *P-wave results for the sum of $B^0 \to J/\psi K^{*0}$ and $\overline{B}^0 \to J/\psi \overline{K}^{*0}$ candidates. The uncertainties are statistical and systematic, respectively.*

Parameter	BaBar 2007 [29]	Belle 2005 [30]	CDF 2005 [31]
$R_\parallel$	$0.211 \pm 0.010 \pm 0.006$	$0.231 \pm 0.012 \pm 0.008$	$0.211 \pm 0.012 \pm 0.009$
$R_\perp$	$0.233 \pm 0.010 \pm 0.005$	$0.195 \pm 0.012 \pm 0.008$	$0.220 \pm 0.015 \pm 0.011$
$\delta_\parallel$	$-2.93 \pm 0.08 \pm 0.04$	$-2.887 \pm 0.090 \pm 0.008$	$-2.96 \pm 0.08 \pm 0.03$
$\delta_\perp$	$2.91 \pm 0.05 \pm 0.03$	$2.938 \pm 0.064 \pm 0.010$	$2.97 \pm 0.06 \pm 0.01$

Parameter	LHCb 2013 (Neglecting S-wave)
$R_\parallel$	$0.220 \pm 0.004 \pm 0.003$
$R_\perp$	$0.210 \pm 0.004 \pm 0.004$
$\delta_\parallel$	$-2.98 \pm 0.03 \pm 0.01$
$\delta_\perp$	$2.97 \pm 0.02 \pm 0.02$

Table 9.2: *Results from previous experiments where the S-wave has not been taken into account compared to the results of this analysis. The uncertainties are statistical and systematic, respectively.*

The maximum likelihood fit is performed in four $K^+\pi^-$ mass bins using the sFit technique described in Subsec. 4.3.3. The corresponding acceptance factors are listed in Table 4.1. They are obtained after the full reweighting procedure as described in Ch. 6 has been performed. The results are summarised in Table 9.1, showing both the statistical and the systematic error. One can see that the results for the amplitudes have approximately the same value, i.e. $R_\parallel \approx R_\perp$. The phases are significantly away from 0 mod π, showing evidence for final state interactions. This is expected for colour-suppressed modes as explained in Subsec. 1.4.2.
As has been stated in the introduction the original motivation for this analysis was the comparison with $B_s^0 \to J/\psi\phi$ decays. The results for the P-wave amplitudes and phases of this decay channel as measured by LHCb [77] are compatible with those listed in Table 9.1 within two standard deviations. This shows that the polarisation of the final state particles is very similar in both decays.
In Subsec. 1.4.5, results from other experiments have been discussed [29, 30, 31]. As they do not include any S-wave component, the maximum likelihood fit used for this analysis has been performed neglecting all S-wave contributions to be able to compare the results. The systematic errors have been calculated in the same way as for the nominal fit. The iterative acceptance determination, however, has not been applied as the S-wave component has been neglected. The systematic error due to differences between data and simulation is much reduced compared to the full fit, reducing the total uncertainty. Note that to correctly determine the total systematic error the effect of neglecting the S-wave component would have to be estimated. This is not done here as neglecting non-resonant contributions is not a fully correct approach in the first place. Thus, these results are only determined for the sake of

$m(K^+\pi^-)$ bin	N_{sig}	f_{sig}	Parameter	Fit result
$826 - 861$ MeV	$6\,456 \pm 69$	0.651 ± 0.007	$F_{\text{S}}^{(1)}$	$0.115 \pm 0.007 \pm 0.020$
			$\delta_{\text{S}}^{(1)} - \delta_0^{(1)}$	$3.09 \pm 0.10 \pm 0.08$
$861 - 896$ MeV	$24\,418 \pm 80$	0.846 ± 0.003	$F_{\text{S}}^{(2)}$	$0.049 \pm 0.004 \pm 0.007$
			$\delta_{\text{S}}^{(2)} - \delta_0^{(2)}$	$2.66 \pm 0.06 \pm 0.06$
$896 - 931$ MeV	$23\,036 \pm 77$	0.845 ± 0.003	$F_{\text{S}}^{(3)}$	$0.052 \pm 0.006 \pm 0.009$
			$\delta_{\text{S}}^{(3)} - \delta_0^{(3)}$	$1.94 \pm 0.03 \pm 0.09$
$931 - 966$ MeV	$7\,383 \pm 64$	0.656 ± 0.006	$F_{\text{S}}^{(4)}$	$0.105 \pm 0.014 \pm 0.008$
			$\delta_{\text{S}}^{(4)} - \delta_0^{(4)}$	$1.53 \pm 0.03 \pm 0.11$

Table 9.3: *Signal yield N_{sig}, signal fraction f_{sig} and fit results for the S-wave parameters in the four bins of $m(K^+\pi^-)$, showing the statistical and systematic uncertainties. Only the physical solution is shown for the phase difference between S- and P-wave, $\delta_{\text{S}} - \delta_0$. The average S-wave fraction is $F_{\text{S}} = (6.4 \pm 0.3 \pm 1.0)\%$*

comparison. This comparison can be found in Table 9.2. The results presented here agree very well with the results from other experiments and the statistical errors are smaller by a factor two to three. Note that due to the reasons mentioned above the systematic uncertainties cannot be easily compared.

9.2 S-wave results

The S-wave parameters are determined in four $m(K^+\pi^-)$ bins of equal width. Table 9.3 lists the S-wave parameters for each bin and the corresponding number of signal candidates and the signal fraction. The phase δ_0 has been added explicitly to emphasise that this is the phase difference between S-wave and P-wave. How the ambiguity mentioned in Subsec. 1.4.3 can be resolved is explained in Sec. 9.3. Only the physical solution is shown here. As expected, the S-wave fraction is much higher in the outer bins, far away from the known K^{*0} mass [5]. An extensive discussion about the number of S-wave events in each bin has been brought up in the Ch. 7. The statistical error of the signal yield is obtained by propagating the error on the signal fraction in the corresponding bin. It is assumed that the total number of candidates has no error.
An average S-wave fraction can be obtained by integrating over all four bins. This gives a value of $F_{\text{S}} = (6.4 \pm 0.3 \pm 1.0)\%$ in the full mass window of ± 70 MeV around the known K^{*0} mass [5]. In the $K^+\pi^-$ mass range between 0.8 and 1.0 GeV BaBar has measured a fraction of $(7.3 \pm 1.8)\%$ [29], well in agreement with the results presented here.

9.3 Further investigations

The fit results summarised in the two previous sections can be tested in various ways. The first step is to evaluate the projection plots of the decay time and the transversity angles which are shown in Fig. 9.1. The plots show the averaged contributions over the four $K^+\pi^-$ mass bins. The data points agree very well with the projection of the total probability density function (solid blue line). As already observed in the previous chapter, the P-even component in the $\cos\psi$ projection is above the data points for large values of $\cos\psi$ because the (partially negative) interference terms are not included in the P- and S-wave contributions but are taken into account for the sum of all components. The very asymmetric shape of the $\cos\psi$ distribution can be understood by the acceptance curves shown in Fig. 3.3. In the decay time projection plot no difference is visible between the P-even and the P-odd component. This is expected as the decay time width difference for B^0 mesons, $\Delta\Gamma_d$, is assumed to be 0.

The next step is to investigate the correlations between the physics parameters.

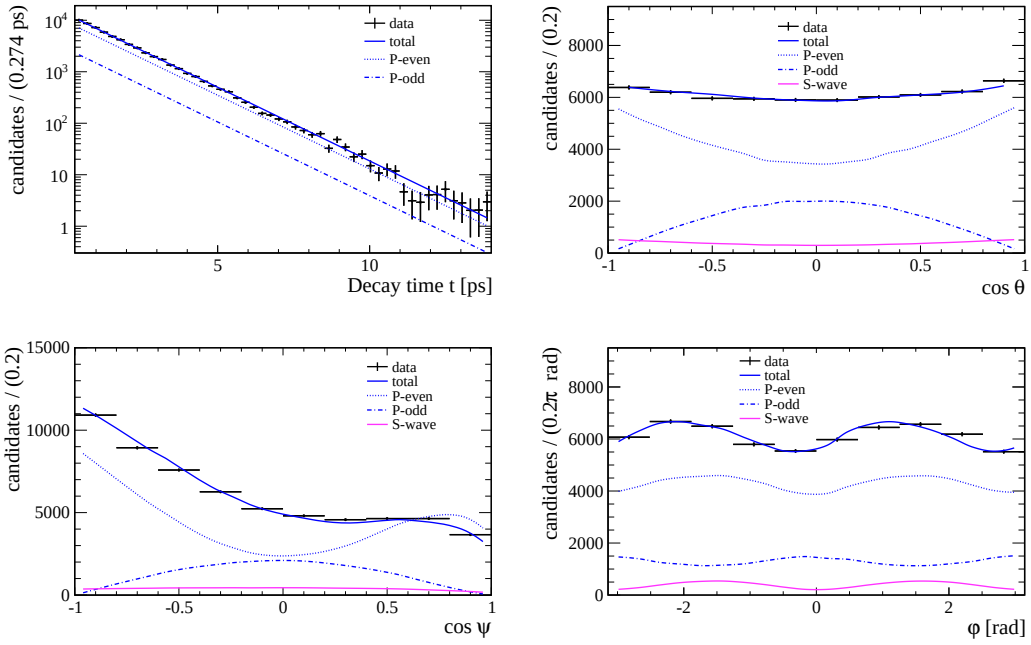

Figure 9.1: *Projection plots of the decay time and the three transversity angles corresponding to the fit results presented in this chapter (points with statistical error bars). The plots show the P-wave parity-even (dotted blue) and parity-odd (dashed blue) components, the pure S-wave (purple) contribution without interference terms and the total signal component (solid blue).*

	$R_\parallel$	$R_\perp$	$\delta_\parallel$	$\delta_\perp$	$F_\mathrm{S}^{(1)}$	$\delta_\mathrm{S}^{(1)}$	$F_\mathrm{S}^{(2)}$	$\delta_\mathrm{S}^{(2)}$	$F_\mathrm{S}^{(3)}$	$\delta_\mathrm{S}^{(3)}$	$F_\mathrm{S}^{(4)}$	$\delta_\mathrm{S}^{(4)}$
$R_\parallel$	1.00	**-0.70**	0.12	0.04	0.02	-0.02	0.10	-0.08	0.14	-0.07	0.10	0.03
$R_\perp$		1.00	-0.14	-0.01	0.01	0.02	-0.09	0.12	-0.19	0.15	-0.15	-0.01
$\delta_\parallel$			1.00	**0.64**	-0.01	0.06	-0.06	0.10	-0.07	0.12	-0.02	0.07
$\delta_\perp$				1.00	-0.03	0.14	-0.16	**0.21**	-0.17	0.18	-0.09	0.05
$F_\mathrm{S}^{(1)}$					1.00	**-0.24**	0.01	-0.01	-	-	-	-
$\delta_\mathrm{S}^{(1)}$						1.00	-0.03	0.03	-0.03	0.03	-0.02	-
$F_\mathrm{S}^{(2)}$							1.00	**-0.76**	0.05	-0.04	0.03	-
$\delta_\mathrm{S}^{(2)}$								1.00	-0.06	0.05	-0.04	0.01
$F_\mathrm{S}^{(3)}$									1.00	**-0.59**	0.04	-
$\delta_\mathrm{S}^{(3)}$										1.00	-0.04	0.01
$F_\mathrm{S}^{(4)}$											1.00	0.19
$\delta_\mathrm{S}^{(4)}$												1.00

Table 9.4: *Correlation matrix for the default sFit. The numbers across the diagonal are the same. The dash indicates no correlation. Large contributions are highlighted in bold font.*

They are listed in the correlation matrix of Table 9.4. In the sFit the decay time is not used to separate between signal and background and the physics results do not change whether it is fixed or floating in the fit. When left free, the correlation between the decay time and the polarisation amplitudes is zero, thus not included in Table 9.4. Overall, the correlations are rather small, except for most of the S-wave amplitudes and the corresponding phases. The only other significant correlations can be observed between the two P-wave amplitudes $R_\parallel$ and $R_\perp$ which is -0.70. This is expected as the normalisation condition $\sum_i R_i = 1$ holds. And, additionally, between the two P-wave phases. The correlation between the S-wave amplitudes is surprisingly low. This indicates that the different $K^+\pi^-$ mass bins are rather independent from each other.

Another important crosscheck is the calculation of profile likelihood scans as discussed in Sec. 4.1. It has also been emphasised that the error estimation is only valid if the errors are Gaussian distributed. As this is only true for a large number of events, it is important to verify this assumption especially for the S-wave parameters in the four mass bins. In the first and last bin there are much less than $10\ 000$ signal candidates. To perform the profile likelihood scan for the parameter λ_i the ratio $-2 \cdot \Delta \ln \mathcal{L}(\lambda_i, \vec{\lambda})$ is determined at grid points of λ_i by minimising the likelihood function with respect to all other parameters, i.e. fixing the parameter under investigation to the grid point. In this case here, 25 grid points are used. The profile likelihood scans for four S-wave parameters can be seen in Fig. 9.2. These

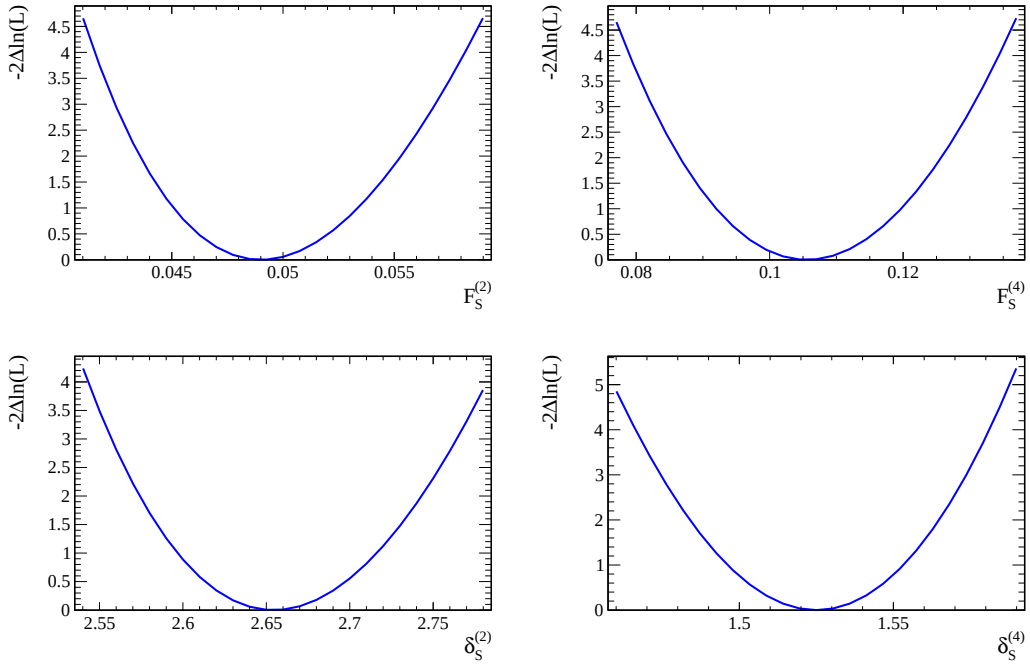

Figure 9.2: *Profile likelihood scans for selected physics parameters.*

parameters have been chosen because problems are rather expected for the S-wave parameters that are determined in four bins with reduced statistics. It can be seen that the distributions are parabolic and confirm the error estimates of the physics parameters given in this chapter. The profiles of all other physics parameters have been found to be parabolic as well [28].

Finally, the measured errors from the fit to data are compared with the expected sensitivities from pseudo-experiments. Similarly to the procedure in Sec. 4.4, 600 pseudo-experiments are generated corresponding to the number of observed candidates. In this case, however, a background fraction corresponding to that observed in data has been included and a cFit is performed. This in particular verifies the error determination of the sFit that is used in the fit to data. The comparison can be found in Tab. 9.5. The agreement between the estimates is very good, especially for the P-wave parameters. There are slight deviations for some of the S-wave parameters but due to the low statistics and high background level this is expected. The error distributions from the pseudo-experiments are Gaussian distributed as expected from the profile scans.

In conclusion, the fit results and error estimations presented in this chapter are robust, also for the first and last $m(K^+\pi^-)$ bin with a low number of signal candidates. In particular, the error estimates for sFit and cFit are fully equivalent.

Parameter	Measured error	Estimated error
$R_{\parallel}$	0.0039	0.0040
$R_{\perp}$	0.0039	0.0040
$\delta_{\parallel}$	0.024	0.026
$\delta_{\perp}$	0.018	0.019
$F_{\mathrm{S}}^{(1)}$	0.0068	0.0063
$\delta_{\mathrm{S}}^{(1)}$	0.101	0.112
$F_{\mathrm{S}}^{(2)}$	0.0040	0.0038
$\delta_{\mathrm{S}}^{(2)}$	0.062	0.071
$F_{\mathrm{S}}^{(3)}$	0.0063	0.0065
$\delta_{\mathrm{S}}^{(3)}$	0.030	0.033
$F_{\mathrm{S}}^{(4)}$	0.0141	0.0152
$\delta_{\mathrm{S}}^{(4)}$	0.029	0.028

Table 9.5: *Error estimates as measured from a fit to data and obtained from 600 pseudo-experiments. The agreement is very good.*

9.4 Resolving the ambiguity

As explained in Subsec. 1.4.3, there are two different solutions for the strong phases of the polarisation amplitudes. The transformation between the two solutions is given by $(\delta_{\parallel}, \delta_{\perp}, \delta_{\mathrm{S}}) \longleftrightarrow (-\delta_{\parallel}, \pi - \delta_{\perp}, -\delta_{\mathrm{S}})$. The two solutions can be disentangled by measuring the phase difference between the P-wave and the S-wave, $\delta_{\mathrm{S}} - \delta_0$, in bins

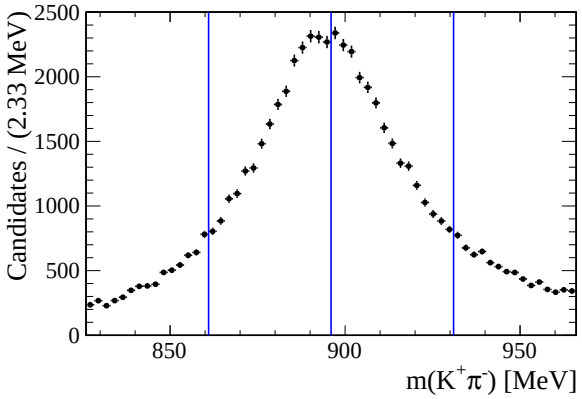

Figure 9.3: *Background subtracted invariant $K^+\pi^-$ mass distribution showing the four bins used to resolve the ambiguity in the strong phases.*

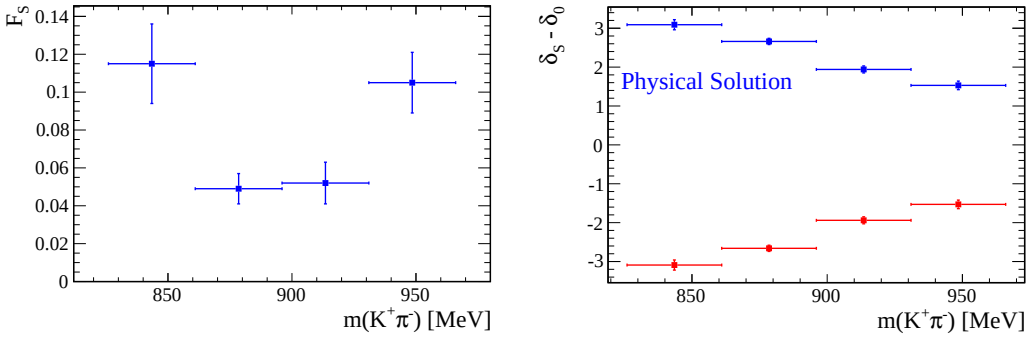

Figure 9.4: *Fit results for (a) the S-wave fraction F_S and (b) the phase difference $\delta_S - \delta_0$, showing two solutions with the falling trend being the physical one. The error bars indicate the quadratic sum of the statistical and systematic error.*

of the $K^+\pi^-$ mass. The $K^+\pi^-$ mass bins are visualised in Fig. 9.3. Corresponding to the two different solutions there are two sets of phase differences $\delta_S - \delta_0$, one has a falling and the other a rising trend. The physical solution is the one with the falling trend. Technically in the fitter, the two solutions are retrieved by changing

Parameter	Physical solution	Second solution
$R_\parallel$	0.227 ± 0.004	0.227 ± 0.004
$R_\perp$	0.201 ± 0.004	0.201 ± 0.004
$\delta_\parallel$	-2.94 ± 0.02	$\mathbf{2.94 \pm 0.02}$
$\delta_\perp$	2.94 ± 0.02	$\mathbf{0.20 \pm 0.02}$
$F_S^{(1)}$	0.115 ± 0.007	0.115 ± 0.007
$\delta_S^{(1)}$	3.09 ± 0.10	$\mathbf{-3.09 \pm 0.10}$
$F_S^{(2)}$	0.049 ± 0.004	0.049 ± 0.004
$\delta_S^{(2)}$	2.66 ± 0.06	$\mathbf{-2.66 \pm 0.06}$
$F_S^{(3)}$	0.052 ± 0.006	0.052 ± 0.006
$\delta_S^{(3)}$	1.94 ± 0.03	$\mathbf{-1.94 \pm 0.03}$
$F_S^{(4)}$	0.105 ± 0.014	0.105 ± 0.014
$\delta_S^{(4)}$	1.53 ± 0.03	$\mathbf{-1.53 \pm 0.03}$

Table 9.6: *Fit results for the two different solutions. Only the statistical error is stated. The differences are highlighted in bold font.*

the starting values of the strong phases to a value near the respective solution. The two different solutions are visualised in Fig. 9.4. To evaluate potential differences between the two solutions, the two fit results are summarised in Table 9.6. Only the statistical error is given. Both sets of results are fully compatible, the strong phases change accordingly to the transformation between the two solutions. The ambiguity can be resolved by using any of the P-wave phases, δ_0 has been chosen as it does not require technical changes in the fitting procedure.
The ambiguity has previously been resolved by BaBar, see [32]. They also observe two distinct solutions for the phase difference $\delta_S - \delta_0$ and identify the falling trend as the physical solution. They use a $K^+\pi^-$ mass range from 0.8 to 1.5 GeV which makes a quantitative comparison with the results presented here difficult.
All results presented in the previous sections correspond to the physical solution.

9.5 Search for direct CPV

In Sec. 1.5 several possibilities have been explained how physics beyond the Standard Model can be observed. One way is to measure the polarisation amplitudes and corresponding phases separately for $B^0 \to J/\psi K^{*0}$ and $\overline{B}^0 \to J/\psi \overline{K}^{*0}$ decays. Any deviations between the two sub-samples would be a clear sign for direct CPV and thus BSM processes as the SM does not predict any CPV for the studied decay channel [6, 7, 8]. The fitting procedure is the same as for the full data sample, only some small changes have been made.
Firstly, two different acceptance histograms, one for each sub-sample, are used to take possible differences from charge asymmetries in the detector into account. The two sets of acceptance factors are shown in Table 9.7. The same iterative method as for the full sample is used. The weights are compatible with each other. The largest discrepancy can be observed for ξ_{10}.
Secondly, the S-wave parameters are fixed to the results from the fit to the full data sample, i.e. they are not left free as this is the case for the default fit. This has several reasons. First of all, the predictions for new phenomena beyond the SM as discussed in Sec. 1.5 do not include the non-resonant contributions but only rely on terms including the P-wave amplitudes. No predictions are made for the S-wave terms. As other experiments have not included S-wave contributions when measuring CP asymmetries, fixing the S-wave parameters allows an easier comparison with these experiments. As a cross-check the fits to the two sub-samples have also been performed with the S-wave parameters kept free. Only marginal changes on the P-wave amplitudes have been observed. The iterative acceptance determination as described in Ch. 6 has been applied in the same way as for the fit to the full data sample, now separately for the two sub-samples. Note that to perform the iterative method the S-wave parameters are required to be floating in the fit. Hence, fixing the S-wave parameters is only done for the final fit after all reweighting procedures have been applied. Using the same single acceptance histogram for the separate B^0

Factor	$B^0 \to J/\psi K^{*0}$ sample	$\overline{B}^0 \to J/\psi \overline{K}^{*0}$ sample
ξ_1	0.8986 ± 0.0024	0.8987 ± 0.0024
ξ_2	1.1769 ± 0.0034	1.1701 ± 0.0034
ξ_3	1.1813 ± 0.0036	1.1778 ± 0.0036
ξ_4	0.0017 ± 0.0025	0.0007 ± 0.0025
ξ_5	-0.0121 ± 0.0015	-0.0106 ± 0.0016
ξ_6	-0.0003 ± 0.0015	-0.0019 ± 0.0015
ξ_7	1.0336 ± 0.0027	1.0257 ± 0.0027
ξ_8	-0.0100 ± 0.0022	-0.0127 ± 0.0022
ξ_9	0.0013 ± 0.0021	0.0020 ± 0.0021
ξ_{10}	-0.2191 ± 0.0041	-0.2350 ± 0.0041

Table 9.7: *Acceptance factors for $B^0 \to J/\psi K^{*0}$ and $\overline{B}^0 \to J/\psi \overline{K}^{*0}$ candidates. Only the statistical error is given.*

and $\overline{B}^0$ fits would not change the P-wave results significantly. The strategy with two different histograms has been chosen to detect any acceptance differences between the two sub-samples.
The results of the two fits and the corresponding CP asymmetry are summarised in Table 9.8. For the results of the two separate fits only the statistical error is given. The B^0-$\overline{B}^0$ asymmetry is defined as

$$A_{\substack{(-)\\f}} = \frac{\overline{X} - X}{\overline{X} + X}, \tag{9.1}$$

where X denotes the parameter in consideration and f or $\overline{f}$ the final state. Note

Parameter	Value for B^0	Value for $\overline{B}^0$	B^0-$\overline{B}^0$ asymmetry
$R_\parallel$	0.230 ± 0.005	0.225 ± 0.005	$-0.011 \pm 0.016 \pm 0.005$
$R_\perp$	0.194 ± 0.005	0.207 ± 0.005	$0.032 \pm 0.018 \pm 0.003$
$\delta_\parallel$	-2.94 ± 0.03	-2.92 ± 0.03	$0.003 \pm 0.007 \pm 0.002$
$\delta_\perp$	2.94 ± 0.02	2.96 ± 0.02	$0.003 \pm 0.005 \pm 0.001$

Table 9.8: *Results from fits to the $B^0 \to J/\psi K^{*0}$ and $\overline{B}^0 \to J/\psi \overline{K}^{*0}$ samples and the direct CP asymmetries $\frac{\overline{X}-X}{\overline{X}+X}$, where X is the corresponding parameter. The uncertainties are statistical for the amplitudes and phases and both statistical and systematic for the direct CP asymmetry.*

that the systematic errors of the asymmetry is much reduced as most contributions cancel in the difference. The asymmetries show no evidence for direct CP violation, they are all compatible with zero within two standard deviations. This is in agreement with similar results from Belle, listed in Table 1.6, but more precise. The mass fit yields $30\,896 \pm 95$ and $30\,422 \pm 92$ signal candidates for $B^0 \to J/\psi K^{*0}$ and $\overline{B}^0 \to J/\psi \overline{K}^{*0}$ decays, respectively. As naïvely expected, the statistical errors scale with the number of events, i.e. are larger by approximately a factor of $\sqrt{2}$ compared to the results from the full fit. Likelihood scans are not shown as they are parabolic as expected.
The systematic uncertainties are calculated only for the CP asymmetry. The numbers are summarised in Table 9.9. The measurement of the CP asymmetries is largely statistically limited, thus it would be worthwhile to repeat the analysis with a larger data sample. The systematic errors have been determined in the same way as for the combined fit, a few issues, however, should be noted:

- A larger systematic error for the amplitude $R_\parallel$ compared to the combined fit is observed when the mass model for the B^0 meson is changed from a double to a single Gaussian function. This hints at a small difference in the mass description between B^0 and $\overline{B}^0$ mesons. For the other parameters the systematic error is negligible.

- The effect of the background model (i.e. using cFit instead of sFit) on the fit results is compatible with that for the combined fit.

- The same statement holds for the effect of the misreconstructed background. Both contributions are small.

- The differences between data and simulation cancel to a large extent in the

Source	$R_\parallel$	$R_\perp$	$\delta_\parallel$	$\delta_\perp$
Mass model	0.003	0.000	0.00	0.00
Background treatment	0.001	0.001	0.02	0.01
Misreconstructed background	0.001	0.002	0.01	0.01
Angular acceptance	0.003	0.002	0.00	0.00
Statistical uncertainty on acceptance	0.000	0.000	0.00	0.00
Other resonances	0.000	0.000	0.00	0.00
Total systematic uncertainty	0.005	0.003	0.02	0.01
Statistical uncertainty	0.016	0.018	0.07	0.05

Table 9.9: *Contributions to the systematic error of the CP asymmetry results.*

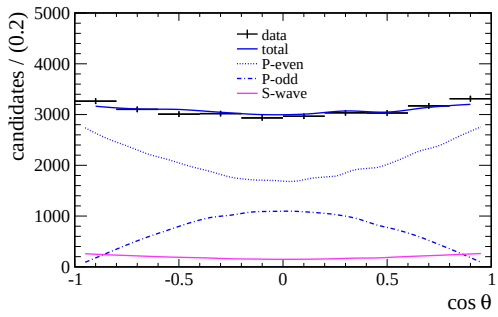

(a) $\cos\theta$ projection plot for B^0 sample

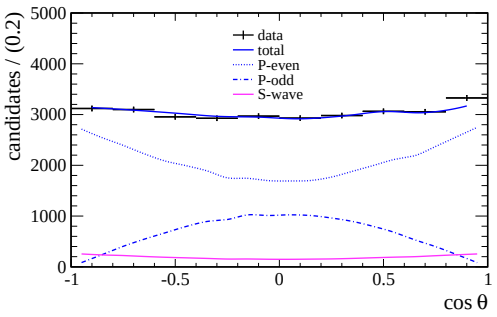

(b) $\cos\theta$ projection plot for $\overline{B}^0$ sample

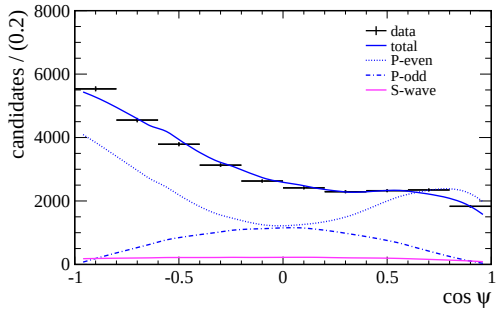

(c) $\cos\psi$ projection plot for B^0 sample

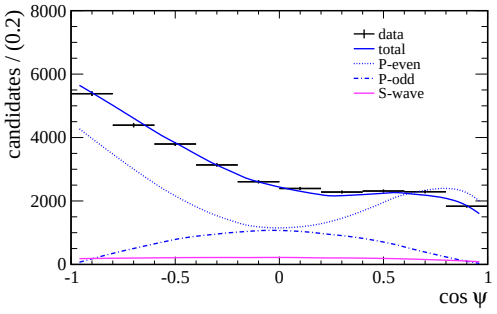

(d) $\cos\theta$ projection plot for $\overline{B}^0$ sample

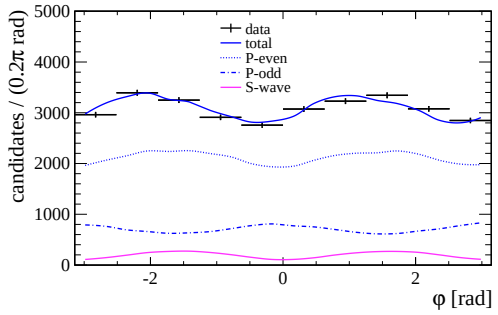

(e) φ projection plot for B^0 sample

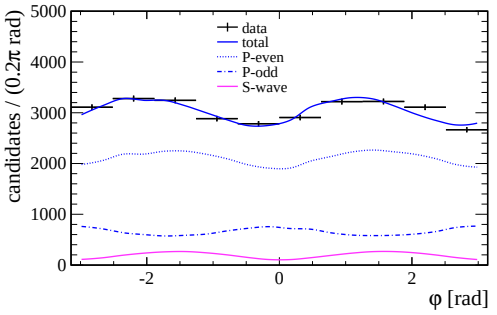

(f) φ projection plot for $\overline{B}^0$ sample

Figure 9.5: *Angular projection plots corresponding to the results from fits to the B^0 and $\overline{B}^0$ samples. The plots show the the P-wave parity-even (dotted blue) and parity-odd (dashed blue) components, the pure S-wave (purple) contribution without interference terms and the total signal component (solid blue). The difference between the sub-samples is small and the fitted curves agree well with the data points.*

difference between B^0 and $\overline{B}^0$ decays. In other words the remaining residual differences after the iterative acceptance determination are similar for both sub-samples. This is the main reason for the low total systematic uncertainty

on the CP asymmetries as it is the dominant contribution to the P-wave parameters, see Ch. 8.

- The systematic uncertainty due to the statistical error on the acceptance cancels in the difference. Thus, the reduced statistics in the two separate acceptance histograms does not affect the systematic error.

- To estimate the systematic effect of other resonances on the physics parameters, the pseudo-experiments described in Ch. 7 are used. For the systematic error determination it has been assumed that there is no CPV in resonances so that the effect on both sub-samples is the same and cancels in the difference. This assumption has been made because no sign for direct CP violation has been observed. As soon as evidence is found for deviations of the CP asymmetries from zero, possible different effects of other resonances on the two sub-samples have to be taken into account.

In summary, the systematic errors of the CP asymmetries are much smaller compared to the uncertainties of the combined fit because they partially cancel when calculating the difference between B^0 and $\overline{B}^0$ decays.
The angular projection plots for both sub-samples can be seen in Fig. 9.5. The fitted curves are in good agreement with the data points. No significant differences between the two sub-samples can be observed.

9.6 Summary

In this chapter the results of the maximum likelihood fit and the search for CP violation have been presented and the 2-fold ambiguity in the strong phases has been resolved. The results are summarised in Table 9.10.
The results can be separated in three sub-sets. The P-wave parameters are the most important results of the analysis. The two amplitudes have approximately the same value, the corresponding phases are the same within errors but have opposite sign. The phases deviate from 0 mod π, indicating final-state interactions. All P-wave results are compatible with previous measurements.
The S-wave parameters in four $K^+\pi^-$ mass bins present a completely new result. S-wave fractions have been measured before but only integrated over the entire mass range. A clear trend can be observed that the S-wave fraction is much larger in the outer than in the inner two bins. In other words, at large P-wave amplitudes the S-wave fraction decreases. This is expected as the resonant component is concentrated in the vicinity of the known K^{*0} mass [5]. The measurement in four bins enables to resolve the ambiguity in the strong phases. The physical solution corresponds to a falling trend in the phase difference $\delta_{\rm S}^{(i)} - \delta_0$, confirming earlier results.
Calculating the B^0-$\overline{B}^0$ asymmetries for the P-wave parameters shows no evidence for

Parameter	Full fit results	B^0-$\overline{B}^0$ asymmetry
$R_\parallel$	$0.227 \pm 0.004 \pm 0.011$	$-0.011 \pm 0.016 \pm 0.005$
$R_\perp$	$0.201 \pm 0.004 \pm 0.008$	$-0.032 \pm 0.018 \pm 0.003$
$\delta_\parallel$	$-2.94 \pm 0.02 \pm 0.03$	$-0.003 \pm 0.007 \pm 0.002$
$\delta_\perp$	$2.94 \pm 0.02 \pm 0.02$	$0.003 \pm 0.005 \pm 0.001$
$F_{\rm S}^{(1)}$	$0.115 \pm 0.007 \pm 0.020$	
$\delta_{\rm S}^{(1)}$	$3.09 \pm 0.10 \pm 0.08$	
$F_{\rm S}^{(2)}$	$0.049 \pm 0.004 \pm 0.007$	
$\delta_{\rm S}^{(2)}$	$2.66 \pm 0.06 \pm 0.06$	Integrated S-wave fraction:
$F_{\rm S}^{(3)}$	$0.052 \pm 0.006 \pm 0.009$	$0.064 \pm 0.003 \pm 0.10$
$\delta_{\rm S}^{(3)}$	$1.94 \pm 0.03 \pm 0.09$	
$F_{\rm S}^{(4)}$	$0.105 \pm 0.014 \pm 0.008$	
$\delta_{\rm S}^{(4)}$	$1.53 \pm 0.03 \pm 0.11$	

Table 9.10: *Summary of the results from a fit to the full data set showing the physical solution and results from the search for direct CPV. The errors are statistical and systematic, respectively.*

direct CPV. While the results from the combined fit to B^0 and $\overline{B}^0$ decays are systematically limited, the CP asymmetry measurements can be improved by a larger data sample. Thus, it will be interesting to see the results using the combined data set taken in 2011 and 2012, corresponding to an integrated luminosity of approximately 3 fb^{-1}.

Conclusions and perspectives

In this thesis a measurement of the polarisation amplitudes in $B^0 \to J/\psi K^{*0}$ decays has been presented. Serving initially as a cross-check analysis for the study of $B_s^0 \to J/\psi\phi$ decays, it has evolved into a measurement on its own as decay specific issues have to be dealt with. In addition, the charge of the kaon allows to separate the data in two sub-samples, dependent on the flavour of the B^0 meson at the time of decay. This advantage can be used to test for direct CP violation. Any sign of a difference between $B^0 \to J/\psi K^{*0}$ and $\overline{B}^0 \to J/\psi \overline{K}^{*0}$ decays would be a hint for new phenomena beyond the Standard Model of particle physics because it does not predict CP violation for this decay channel [6, 7, 8]. To extract the relevant physical observables a maximum likelihood fit in four dimensions, the decay time and the three angles describing the kinematics of the decay, is used.
For this analysis, the full data sample collected in 2011 with the LHCb detector has been used. The data, taken in pp-collisions at a centre-of-mass energy of 7 TeV, correspond to an integrated luminosity of approximately 1 fb^{-1}. After having applied the selection criteria, roughly $61\,000$ signal candidates remain. In a mass window of 30 MeV around the known B^0 mass [5] the signal fraction is approximately 93%.
Three main challenges of this analysis should be summarised. Firstly, it is important to know the exact composition of the background. Most of it can be described by a flat distribution for combinatorial background. This component can be easily accounted for by the maximum likelihood fit. It can either be subtracted by means of a B^0 mass fit before extracting the physical observables or it can be explicitly described by using events outside the signal region. An extensive study of numerous background contaminations (physical contributions and reconstruction artefacts) using simulated events has been performed and only one significant non-flat component remains that shows a peaking structure in the region around the known B^0 mass [5]. This reconstruction artefact consists mainly of misreconstructed pion tracks and is treated as systematic uncertainty.
Secondly, as the determination of the angular detector acceptance relies on simulated events, it is crucial to ensure that the important kinematic contributions agree between data and simulation. In most of the variables both samples agree well, a significant difference, however, has been observed for the pion and, due to a high

correlation, for the kaon momentum. Partially, this effect can be explained by the fact that non-resonant contributions (the so-called S-wave) are not taken into account in the simulation. An iterative procedure has been developed that effectively adds an S-wave contribution to the simulation. This reduces the discrepancy in the pion momentum. The remaining difference is partially attributed to detector effects and is treated as systematic uncertainty.
Thirdly, the maximum likelihood fit takes into account only P-wave resonances (i.e. with a total spin of $J = 1$; in the selected $K^+\pi^-$ mass range of this analysis this is the $K^*(892)^0$) and the S-wave contribution into account. However, several other resonances with higher spin have to be considered also in the relatively narrow $K^+\pi^-$ mass range of this analysis. Especially important is a D-wave state ($J = 2$), the $K_2^*(1430)$ resonance, which can interfere with the P-wave. Pseudo-experiments show that such resonances can change the distribution of the S-wave yield measured in bins of the $K^+\pi^-$ mass and also the P-wave amplitudes. As these states are not modelled in the maximum likelihood fit explicitly, a systematic uncertainty is assigned based on the results of the pseudo-experiments.
All three issues are responsible for most of the systematic uncertainties in the determination of the polarisation amplitudes. The individual physical observables are dominated by different systematic sources.
The maximum likelihood fit is performed in four bins of the $K^+\pi^-$ mass because the S-wave amplitude depends on the $K^+\pi^-$ mass which is not explicitly taken into account by the fit. The P-wave parameters, however, are not mass dependent and hence, are determined globally for the full mass range. The results of the fit can be separated in different parameter sets. The P-wave amplitudes and their corresponding phases have been determined to be

$$\begin{aligned} R_\parallel &= 0.227 \pm 0.004 \pm 0.011, \\ R_\perp &= 0.201 \pm 0.004 \pm 0.008, \\ \delta_\parallel &= -2.94 \pm 0.02 \pm 0.03, \\ \delta_\perp &= \quad 2.94 \pm 0.02 \pm 0.02, \end{aligned}$$

where the errors are statistical and systematic, respectively. The S-wave amplitudes vary significantly from $K^+\pi^-$ mass bin to $K^+\pi^-$ mass bin ($826-861$ MeV, $861-896$ MeV, $896-931$ MeV and $931-966$ MeV):

$$\begin{aligned} F_{\mathrm{S}}^{(1)} &= 0.115 \pm 0.007 \pm 0.020, \\ F_{\mathrm{S}}^{(2)} &= 0.049 \pm 0.004 \pm 0.007, \\ F_{\mathrm{S}}^{(3)} &= 0.052 \pm 0.006 \pm 0.009, \\ F_{\mathrm{S}}^{(4)} &= 0.105 \pm 0.014 \pm 0.008. \end{aligned}$$

There is a 2-fold ambiguity in the strong phases which has been resolved by measuring the difference between the S-wave and the P-wave phase, $\delta_{\mathrm{S}} - \delta_0$, in the four bins,

resulting in a monotonously decreasing or increasing solution. The falling solution corresponding to the expected $\pi/2$ phase change over a resonance is the physical one.
The results for the P-wave parameters presented here are well in agreement with measurements from other experiments and are statistically more precise by a factor two to three. It is also the first time that S-wave parameters are quoted in different $K^+\pi^-$ mass bins.
The maximum likelihood fit has also been performed for the two sub-samples from B^0 and $\overline{B}^0$ decays separately. No evidence for CP violation has been observed thus, confirming Standard Model predictions.
The measurement is clearly systematically dominated, i.e. a simple increase in the number of signal candidates, which can easily be accomplished by including the full data set taken in 2012, does not result in a much smaller uncertainty. When analysing the combined sample, more than 3 fb^{-1}, measures have to be taken to reduce the systematic error significantly. This can only be achieved in the following way: The difference between data and simulation has to be decreased either by improving the simulation or by investigating the exact reason for the remaining discrepancy. In addition, all resonances relevant for the selected $K^+\pi^-$ mass range have to be taken into account. This can be done by modelling D-wave and other contributions in the fit model used in this analysis and by explicitly taking the $K^+\pi^-$ mass dependency into account.
Another important cross-check for the Standard Model will be further searches for direct CP violation. These can be performed not only by fitting the two sub-samples separately, also other CP observables can be extracted. Such tests can place constraints on models describing new phenomena, see e.g. [8]. In this context it will also be important to correctly estimate effects from penguin diagrams.
Using the decay of the K^{*0} meson to another final state, namely the process $B^0 \to J/\psi(\mu^+\mu^-)K^{*0}(K^0_s\pi^0)$, the angle $\cos 2\beta$ of the CKM triangle can be measured by performing a fully time-dependent analysis. For LHCb, however, this will remain a very difficult measurement as neutral pions are very hard to detect.
In summary, this analysis presents the currently most precise measurements of the P-wave amplitudes. The two transverse amplitudes are approximately of equal size. The significant deviation of the P-wave phases from π is an evidence for final state interactions. The S-wave fractions in the four mass bins represent a new measurement. They are highly dependent on the $K^+\pi^-$ mass bin and can be affected by higher $K^+\pi^-$ resonances. The CP asymmetries are consistent with zero, thus showing no sign for new phenomena beyond the Standard Model.
The years ahead at the LHC will remain exciting and the particle physics community will continue to look for a smoking gun of "New Physics".

Bibliography

[1] ATLAS collaboration, G. Aad *et al.*, *Observation of a new particle in the search for the Standard Model Higgs boson with the ATLAS detector at the LHC*, Phys. Lett. B **716** (2012) 1, arXiv:1207.7214; CMS collaboration, S. Chatrchyan *et al.*, *Observation of a new boson at a mass of 125 GeV with the CMS experiment at the LHC*, Phys. Lett. B **716** (2012) 30, arXiv:1207.7235.

[2] A. Sakharov, *Violation of CP invariance, C asymmetry, and baryon asymmetry of the universe*, Pisma Zh. Eksp. Teor. Fiz. **5** (1967) 32.

[3] J. Christenson, J. Cronin, V. Fitch, and R. Turlay, *Evidence for the 2π decay of the K_2^0 meson*, Phys. Rev. Lett. **13** (1964) 138.

[4] G. Lueders, *On the equivalence of invariance under time reversal and under particle-anti-particle conjugation for relativistic field theories*, Math. Fysik. Medd. Kgl. Danske Akad. Ved **28** (1954) 5; W. Pauli, *Exclusion principle, lorentz group and reflection of space-time and charge*, W. Pauli, ed. , Niels Bohr and the Development of Physics, Pergamon Press, New York (1955).

[5] J. Beringer *et al. (Particle Data Group)*, *Review of Particle Physics*, Phys. Rev. **D86** (2012) 010001 and 2013 partial update for the 2014 edition.

[6] X.-G. He and W.-S. Hou, *Direct CP violation in the angular distribution of $B \to J/\psi K^*$ decays*, Phys. Rev. **D58** (1998) 117502, arXiv:hep-ph/9807507.

[7] D. London, N. Sinha, and R. Sinha, *Probing new physics via an angular analysis of $B \to V_1 V_2$ decays*, Europhys. Lett. **67** (2004) 579, arXiv:hep-ph/0304230v2.

[8] W.-S. Hou, M. Nagashima, and A. Soddu, *$B \to J/\psi K^*$ in a supersymmetric right-handed flavor mixing scenario*, Phys. Rev. **D71** (2005) 016007, arXiv:hep-ph/0409197.

[9] A. Bien, *Simulation study for the determination of the CP violating B_s^0 mixing phase ϕ_s with LHCb*, Diploma thesis, Heidelberg University (2010).

[10] S. Glashow, *Partial-symmetries of weak interactions*, Nucl. Phys. **22** (1961) 579.

[11] A. Salam and J. Ward, *Electromagnetic and weak interactions*, Phys. Lett. **13** (1964) 168.

[12] S. Weinberg, *A Model of Leptons*, Phys. Rev. Lett. **19** (1967) 1264.

[13] Super-Kamiokande collaboration, Y. Ashie *et al.*, *Evidence for an oscillatory signature in atmospheric neutrino oscillation*, Phys. Rev. Lett. **93** (2004) 101801, arXiv:hep-ex/0404034; IceCube collaboration, M. Aartsen *et al.*, *Measurement of atmospheric neutrino oscillations with IceCube*, Phys. Rev. Lett. **111** (2013) 081801, arXiv:1305.3909.

[14] Povh, Rith, Scholz, and Zetsche, *Teilchen und Kerne*, Springer, 7th ed., 2006.

[15] G. Altarelli, *The Standard Model of particle physics*, to appear in Encyclopedia of Mathematical Physics (2005) arXiv:hep-ph/0510281.

[16] A. Djouadi, *The anatomy of electro-weak symmetry breaking I*, Physics Reports **457** (2005) 1, arXiv:hep-ph/0503172.

[17] M. Kobayashi and T. Maskawa, *CP violation in the renormalizable theory of weak interaction*, Prog. Theor. Phys. **49** (1973) 652.

[18] D. London, N. Sinha, and R. Sinha, *New physics in $B \to J/\psi K^*$*, FPCP conference talk (2002) arXiv:hep-ph/0207007.

[19] LHCb collaboration, R. Aaij *et al.*, *Measurement of the polarisation amplitudes in $B^0 \to J/\psi K^*(892)^0$ decays*, Phys. Rev. D **88** (2013) 052002, arXiv:1307.2782.

[20] BaBar collaboration, D. Boutigny *et al.*, *The BaBar physics book: Physics at an asymmetric B factory*, SLAC report **SLAC-R-504** (1999).

[21] A. Dighe, I. Dunietz, and R. Fleischer, *Extracting CKM phases and $B_s - \bar{B}_s$ mixing parameters from angular distributions of non-leptonic B decays*, Eur. Phys. J. **C6** (1999) 647, arXiv:hep-ph/9804253.

[22] A. Dighe, I. Dunietz, H. Lipkin, and J. Rosner, *Angular distributions and lifetime differences in $B_s \to J/\psi\phi$ decays*, Phys. Lett. **B369** (1996) 144, arXiv:hep-ph/9511363.

[23] J. Rosner, *Determination of pseudoscalar-charmed-meson decay constants from B-meson decays*, Phys. Rev. **D42** (1990) 3732.

[24] Y. Xie, P. Clarke, G. Cowan, and F. Muheim, *Determination of $2\beta_s$ in $B_s^0 \to J/\psi K^+K^-$ decays in the presence of a K^+K^- S-wave contribution*, JHEP **09** (2009) 074, arXiv:0908.3627.

[25] R. Aaij *et al.*, *Determination of the sign of the decay width difference in the B_s system*, Phys. Rev. Lett. **108** (2012) 241801, arXiv:1202.4717.

[26] E. Wigner, *Lower limit for the energy derivative of the scattering phase shift*, Phys. Rev. **98** (1955) 145.

[27] Y. Xie, *LHCb internal note: Some physics and technical issues in analysis of the decay $B_s^0 \to J/\psi K^+K^-$*, LHCb-INT-2012-017 (2012).

[28] A. Bien *et al.*, *Angular analysis of $B^0 \to J/\psi K^*(892)^0$ with ~ 1 fb^{-1}*, LHCb-ANA-2012-036 (2012).

[29] BaBar collaboration, B. Aubert *et al.*, *Measurement of decay amplitudes of $B \to J/\psi K^*$, $\psi(2S)K^*$ and $\chi_{c1}K^*$ with an angular analysis*, Phys. Rev. **D76** (2007) 031102, arXiv:0704.0522.

[30] Belle collaboration, K. Abe *et al.*, *Studies of CP violation in $B \to J/\psi K^*$ decays*, Phys. Rev. Lett. **95** (2005) 091601.

[31] CDF collaboration, F. Abe *et al.*, *Angular analysis of $B_s \to J/\psi\phi$ and $B^0 \to J/\psi K^*$ decays and Measurement of $\Delta\Gamma_s$ and ϕ_s*, CDF note 8950 (2007).

[32] BaBar collaboration, B. Aubert *et al.*, *Time-integrated and time-dependent angular analyses of $B \to J/\psi K\pi$: A measurement of $cos2\beta$ with no sign ambiguity from strong phases*, Phys. Rev. **D71** (2005) 032005, arXiv:hep-ex/0411016.

[33] BaBar collaboration, B. Aubert *et al.*, *Measurement of the $B \to J/\psi K^*(892)$ decay amplitudes*, Phys. Rev. Lett. **87** (2001) 241801, arXiv:hep-ex/0107049.

[34] L. Evans and P. Bryant, *LHC machine*, JINST **3** (2008) S08001.

[35] ATLAS collaboration, G. Aad *et al.*, *The ATLAS Experiment at the CERN Large Hadron Collider*, JINST **3** (2008) S08003.

[36] CMS collaboration, S. Chatrchyan *et al.*, *The CMS Experiment at the CERN LHC*, JINST **3** (2008) S08004.

[37] ALICE collaboration, K. Aamodt *et al.*, *The ALICE Experiment at the CERN LHC*, JINST **3** (2008) S08002.

[38] LHCb collaboration, A. Augusto Alves Jr *et al.*, *The LHCb Experiment at the CERN LHC*, JINST **3** (2008) S08005.

[39] *LHC overview map*, http://lhcb-public.web.cern.ch/lhcb-public/en/detector/Detector-en.html, last checked: 07-11-2013.

[40] LHCb collaboration, *LHCb Material for presentations*, http://lhcb.web.cern.ch/lhcb/speakersbureau/html/Material_for_Presentations.html, last checked: 07-11-2013.

[41] J. Nardulli, *Reconstruction of two-body B decays in LHCb*, CERN-THESIS-2007-063 (2007).

[42] LHCb collaboration, R. Aaij *et al.*, *Measurement of J/ψ production in pp collisions at $\sqrt{s} = 7$ TeV*, Eur. Phys. J. **C71** (2011) 1645, arXiv:1103.0423.

[43] M. Schiller, *Track reconstruction and prompt K^0_S production at the LHCb experiment*, PhD thesis, Heidelberg University (2011).

[44] *TT detector*, http://lhcb.physik.uzh.ch/ST/public/material/index.php, last checked: 07-11-2013.

[45] LHCb collaboration, A. Barbosa *et al.*, *LHCb inner tracker: Technical Design Report*, CERN document server (2002).

[46] C. Langenbruch, *Measurement of the B^0_s mixing phase in the decay $B^0_s \to J/\psi\phi$ with the LHCb experiment*, CERN-THESIS-2011-161 (2011).

[47] M. Adinolfi *et al.*, *Performance of the LHCb RICH detector at the LHC*, Eur. Phys. J. **C73** (2012) 2431, arXiv:1211.6759.

[48] O. Deschamps, *LHCb colorimeter: Commissioning and performance*, CERN-TALK-2010-053 (2010).

[49] LHCb collaboration, *The LHCb reconstruction program*, http://lhcb-release-area.web.cern.ch/LHCb-release-area/DOC/brunel/, last checked: 07-11-2013.

[50] LHCb collaboration, *The LHCb analysis program*, http://lhcb-release-area.web.cern.ch/LHCb-release-area/DOC/davinci/, last checked: 07-11-2013.

[51] T. Sjostrand, S. Mrenna, and P. Z. Skands, *Pythia 6.4 physics and manual*, JHEP **05** (2006) , arXiv:hep-ph/0603175.

[52] I. Belyaev *et al.*, *Handling of the generation of primary events in Gauss, the LHCb simulation framework*, Nuclear science symposium conference record (NSS/MIC) IEEE (2010) 1155.

[53] D. Lange, *The EvtGen particle decay simulation package*, Nucl. Instrum. Meth. **A462** (2001) 152.

[54] P. Golonka and Z. Was, *Photos Monte Carlo: a precision tool for QED corrections in Z and W decays*, Eur. Phys. J **C45** (2006) 97.

[55] Geant4 collaboration, J. Allison *et al.*, *Geant Developments and applications*, IEEE Transactions on Nuclear Science **53** (2006), no. 1 270; Geant4 collaboration, S. Agostinelli *et al.*, *Geant: A simulation toolkit*, Nucl. Instrum. Meth. **A506** (2003) 250.

[56] M. Clemencic *et al.*, *The LHCb simulation application, Gauss: design, evolution and experience*, J. of Phys, Conf. Ser **331** (2011) 032023.

[57] Belle collaboration, K. Abe *et al.*, *Measurements of branching fractions and decay amplitudes in $B \to J/\psi K^*$ decays*, Phys. Lett. **B538** (2002) 11.

[58] C. Linn, *Measurement of the CP-violating phase ϕ_s using $B_s^0 \to J/\psi\phi$ and $B_s^0 \to J/\psi\pi^+\pi^-$ decays with the LHCb experiment*, PhD thesis, Heidelberg University (2013).

[59] R. Aaij *et al.*, *Selections and lifetime measurements for exclusive $b \to J/\psi X$ decays with $J/\psi \to \mu^+\mu^-$ with 2010 data*, LHCb-ANA-2011-001 (2011).

[60] R. Aaij *et al.*, *Tagged time-dependent angular analysis of $B_s \to J/\psi\phi$ decays with ~ 337 pb^{-1}*, LHCb-ANA-2011-036 (2011).

[61] M. Needham, *Clone track identification using the Kullback-Liebler distance*, LHCb 2008-002 (2008).

[62] W. D. Hulsbergen, *Decay chain fitting with a Kalman filter*, Nucl. Instrum. Meth. **A552** (2005) 566, `arXiv:physics/0503191`.

[63] M. Pivk and F. R. Le Diberder, *sPlot: A Statistical tool to unfold data distributions*, Nucl. Instrum. Meth. **A555** (2005) 356, `arXiv:physics/0402083`.

[64] T. Skwarnicki, *A study of the radiative cascade transitions between the upsilon-prime and upsilon resonances*, DESY-F31-86-02 (1986).

[65] LHCb collaboration, R. Aaij *et al.*, *Untagged angular analysis of $B_s \to J/\psi\phi$ and $B \to J/\psi K^*$ with the 2010 data*, LHCb-CONF-2011-002 (2011).

[66] T. du Pree, *Search for a strange phase in beautiful oscillations*, PhD thesis, Advisors: Prof. Dr. M. H. M. Merk and Dr. H. G. Raven (2010).

[67] LHCb collaboration, *Twiki page of the β_s working group*, `https://twiki.cern.ch/twiki/bin/viewauth/LHCbPhysics/BetasWGFitting`, last checked: 07-11-2013.

[68] R. Aaij *et al.*, *Tagged time-dependent angular analysis of $B_s^0 \to J/\psi\phi$ decays at LHCb*, LHCb-ANA-2012-004 (2011).

[69] V. Blobel and E. Lohrmann, *Statistische und numerische Methoden der Datenanalyse*, Teubner, 1st ed., 1998.

[70] CERN program library, *Minuit: reference manual*, `http://wwwasdoc.web.cern.ch/wwwasdoc/minuit/minmain.html`, last checked: 07-11-2013.

[71] LHCb Collaboration, B. Adeva *et al.*, *Roadmap for selected key measurements of LHCb*, arXiv:0912.4179.

[72] Y. Xie, *sFit: a method for background subtraction in maximum likelihood fit*, arXiv:0905.0724.

[73] LHCb collaboration, R. Aaij *et al.*, *Amplitude analysis and the branching fraction measurement of* $\overline{B}{}^0_s \to J/\psi K^+K^-$, Phys. Rev. **D87** (2013) 072004, arXiv:1302.1213.

[74] LHCb collaboration, *LHCb generator statistics*, http://lhcb-release-area.web.cern.ch/LHCb-release-area/DOC/STATISTICS/MC11STAT/B2Charm-WG/Generation_Beam3500GeV-md100-MC11-nu2.html#13144003, last checked: 07-11-2013.

[75] LHCb collaboration, V. Gligorov, *Reconstruction of the channel* $B^0_d \to D^+\pi^-$ *and background classification at LHCb (revised)*, LHCb-2007-044 (2007).

[76] T. Skwarnicki and W. Qian, *Confirmation of the* $Z(4430)^+$ *resonance in* $\overline{B}{}^0 \to \psi(2S)K^-\pi^+$ *decays and determination of its spin*, LHCb-ANA-2012-091 (2012); T. Skwarnicki, *Private communication*, 2013.

[77] LHCb collaboration, R. Aaij *et al.*, *Measurement of CP violation and the* B^0_s *meson decay width difference with* $B^0_s \to J/\psi K^+K^-$ *and* $B^0_s \to J/\psi\pi^+\pi^-$ *decays*, Phys. Rev. D **87** (2013) 112010, arXiv:1304.2600.

List of Figures

List of Tables

Acknowledgements

Many people contributed to the work presented in this thesis. First of all, many thanks to my supervisor Prof. Uwer who gave me the opportunity to work in the LHCb group at Heidelberg University as a PhD student and supported me during the course of my research. His ideas were crucial for the solution of some difficult parts of this analysis. Thanks also for taking part in the long discussions with our collaborators and for giving valuable comments to this thesis. I am grateful to Prof. Schultz-Coulon for agreeing to be the second referee and to Prof. Plehn and Prof. Grebel for taking part in the viva.
Within the group at the "Physikalisches Institut" I would like to thank Prof. Hansmann-Menzemer for taking interest in the analysis especially during her term as working group convener and all colleagues I worked with. In particular Marco Meißner for having me as an office mate since my first day as diploma student and for our legendary OT shifts. Finally, we have the quiet office we have hoped for. I also had a great time with Sascha Stahl and Andreas Jäger when we were still in our big office. Christian Linn was an important help during the entire analysis. It was also a pleasure to work and spend time with Francesca Dordei, Lucia Grillo, Sebastian Wandernoth, Paul Seyfert and Thomas Nikodem. Thanks also to Christian Färber for numerous OT crash courses and to Katharina Kreplin and Georg Krocker for being helpful at various occasions. The work would not have been possible without the computing support by Alexey Zhelezov.
Vielen Dank an Frau Wallenwein, ohne die ich vermutlich bis heute auf die Erstattungen der Reisekostenabteilung warten würde.
The analysis presented here was developed in collaboration with the LHCb group in Edinburgh. Special thanks go to Ailsa Sparkes who unfortunately finished her PhD before the analysis had been finalised, Peter Clarke whose enthusiasm and ideas were vital for the analysis and Greig Cowan who contributed a lot to the paper writing. Tomasz Skwarnicki from Syracuse kindly made available the pseudo-experiments used in Chapter 7.
Ich danke meinen Freunden, besonders meinen Kommilitonen Philipp und Michael, mit denen ich Studium und Promotion bestritten habe. Wir haben es doch zu was gebracht. Unschlagbar ist die alte Schultruppe: Tina, Larissa, Erdal, Daniel, Denise.

Ebenso möchte ich Eli für die moralische Unterstützung per E-Mails danken. In addition, I am happy to have Catherine and Katharina from my year abroad among my friends.
Ich danke meinem Physiklehrer in der Oberstufe Herrn Knobloch, ohne den ich vielleicht überhaupt nicht Physik studiert hätte.
Zu guter Letzt ein großer Dank an meine Eltern und Großeltern für ihre Unterstützung all die Jahre, ohne die ich das Studium so nicht geschafft hätte.